2011

Magnesium diboride superconductor: thermal stabilization and doping

Andrey V. Shcherbakov
University of Wollongong

Magnesium Diboride Superconductor: thermal stabilization and doping

A thesis submitted in fulfillment of the requirements

for the award of the degree

DOCTOR of PHILOSOPHY

from the

UNIVERSITY OF WOLLONGONG

by

Andrey V. Shcherbakov, M. Sc.

Institute for Superconducting and Electronic Materials

May 9, 2011

DECLARATION

This is to certify that the work presented in this thesis was carried out by the candidate in the laboratories of the Institute for Superconducting and Electronic Materials at the University of Wollongong, NSW, Australia, and has not been submitted for a degree to any other institution for higher education.

Andrey V. Shcherbakov

May 9, 2011

To my parents, wife and son.

Contents

List of Figures

List of Tables

Acknowledgements

I would like to express my deepest gratitude to my principal supervisor, Prof. S. X. Dou, for his financial support and kind supervision throughout my PhD study. He constantly provided me with useful ideas, was always helpful in discussions of results and encouraged me greatly during my work.

I also grateful to my co-supervisor, A/Prof. J. Horvat, for his guidance with testing facilities, fruitful suggestions for research direction, discussions of results, and critical reading of my papers.

Many thanks go to A/Prof. A. V. Pan for his fruitful discussions of stability issues in superconductors and suggestion of an innovative hot aluminizing approach for fabrication of Al-stabilized MgB_2 wires.

I would like to express my gratitude to the group led by Prof. E. Babic (Croatia) for their contribution to transport measurements of my samples; Dr. T. Silver for editing my thesis and papers; and R. Kinnel for his help with set-up of the furnace for aluminizing and other experimental facilities, as well as his friendly conversations.

Finally, I wish to thank my parents, and my wife and son for their love, support, motivation, and encouragement throughout my PhD study and entire life.

Abstract

The primary aims of this research were to (i) improve the thermal stability of MgB_2 wires, and (ii) investigate the effects of different doping materials on the electromagnetic behaviour of MgB_2 in wire form, enabling practical application of this superconductor.

In this work, a *pioneering* results on the fabrication of Al-stabilized Fe-clad MgB_2 wires have been presented. First, the Al-stabilized Fe-clad MgB_2 wires were fabricated using the existing powder in tube method. The possibility of low temperature *in-situ* MgB_2 formation, as well as the compatibility of the Fe barrier layer and the Al stabilizer at increasing fabrication temperatures of Al/Fe-clad MgB_2 wires have been demonstrated. The range of optimal temperatures (600 - 630 °C) and time of sintering (180 - 30 min) for production of Al-stabilized Fe-clad MgB_2 wires were empirically observed. The main limitations of this method are (i) reduced density of the superconducting core during drawing of relatively soft Al metal, and (ii) degraded connectivity between Al and Fe metals, so that they are not suitable for fabrication of long MgB_2 wires. Thus, a *new approach* towards fabrication of Al-stabilized MgB_2 wires (namely the hot aluminizing technique) was developed. In this technique, fully optimized and *in-situ* reacted Fe/MgB_2 wire was immersed in a molten Al bath, resulting in a uniform Al coating of Fe-clad MgB_2 wire. As demonstrated, this approach does not result in any degradation of superconducting properties of final Al-stabilized Fe-clad MgB_2 wires. However,

this enables reduction of the Fe barrier thickness and good connectivity between Fe and Al sheath materials. Furthermore, this approach is easily applicable for simultaneous aluminizing and *in-situ* formation of MgB_2 wires, which can even be extended to fabrication of Al-stabilized Fe/MgB_2 coils. Although realization of Al-stabilized MgB_2 wires is shown to be possible, future work on stabilization should be focused on increasing the Al thickness, reduction of the Fe barrier layer, and demonstration of the stability effects on Al/MgB_2 wires, which has not been investigated due to limitations of available equipment.

Fe-based doping of MgB_2 wires was studied in order to demonstrate the feasibility of introducing magnetic pinning sites into the MgB_2 system, and to confirm theoretical studies predicting improvement of current carrying ability of (ferro)magnet/superconductor hybrid systems. A systematic study of doping materials, which included nano-Fe, home-made Fe_2B, and SiO_2 coated Fe_2B nanoparticles, was conducted, and the effects of the above-mentioned Fe-based dopants on the superconducting properties of MgB_2 wires were investigated. The SiO_2 coated Fe_2B nanoparticles were employed in order to study the feasibility of insulating the ferromagnetic inclusions and superconducting matrix, as well as to enabling more homogeneous distribution of ferromagnetic particles in MgB_2 superconducting wires. The severe suppression of critical temperature (T_c), critical current density (J_c), and upper critical field (B_{c2}) was observed for all magnetic dopants studied with the most detrimental effect coming from nano-Fe doping and to a lesser extent - from SiO_2 coated Fe_2B nanoparticles. The degradation of superconducting properties due to Fe-based dopants was attributed to an increased level of impurity phases in MgB_2 compound, as confirmed by x-ray diffraction studies. Analysis of the electromagnetic properties suggested that the dominant pinning mechanism is the pinning on grain boundaries (as in pure MgB_2 compound), and thus, magnetic pinning was not achieved in the samples studied by introduction of these

Fe-based dopants. It is likely that more homogeneous systems (such as thin films) are required in order to demonstrate the benefits of superconductor/ferromagnet interactions predicted by theoretical investigations.

The effect of polymer C-based dopants on the properties of MgB_2 wires was systematically investigated. Electromagnetic characteristics ($B_{c2}(T)$ and $J_c(B_a)$, where B_a is an applied magnetic field) of Fe-clad MgB_2 wires with an optimal level of doping material were systematically improved with increasing sintering temperature. The ability of polymer dopants to dissolve in liquid media (water or toluene) and cover B particles by thin layer of amorphous carbon before MgB_2 formation has significant benefits for the fabrication of Fe-clad $MgB_{2-x}C_x$ wires with enhanced homogeneity and electromagnetic performance. The analysis of structural and electromagnetic changes in the Fe-clad MgB_2 wires doped with C_2H_6Si polymer and $C_{12}H_{22}O_{11}$ materials revealed that more C (compared to nano-C doping) is incorporated into the MgB_2 crystal lattice on B sites during sintering, resulting in (i) some reduction of critical temperature (by about 2 K), but (ii) formation of a larger number of nanoscale structural defects, favoring pinning of magnetic vortices and leading to significant enhancement of the superconducting properties of the final Fe-clad $MgB_{2-x}C_x$ wires. However, the results of this work indicate an emerging necessity to improve the density of $MgB_{2-x}C_x$ in the wires in order to reach the superconducting properties obtained in the bulk samples. Another crucial issue is to reduce the level of MgO impurities which is a native impurity formation in any *in-situ* fabricated MgB_2 compounds, although this level may also be increased by introduction of O-containing compounds (e.g. $C_{12}H_{22}O_{11}$). As a result, suppressed current carrying ability was observed in $C_{12}H_{22}O_{11}$-doped MgB_2 wires compared to the critical current density, $J_c(B_a)$, of MgB_2 wires with addition of oxygen free C_2H_6Si doping material. This observation confirms that, in spite of imperfectly connected MgB_2 grains, flowing current is notably affected

by the increased level of insulating MgO impurities that preferentially form at the grain boundaries. Results obtained in this work indicate that oxygen free C_2H_6Si dopant is to be the most optimal and thus promising for practical application of $MgB_{2-x}C_x$ wires.

Chapter 1

Introduction to superconductivity

The effect of superconductivity was discovered nearly 100 years ago (in 1911) by Dutch physicist H. Kamerlingh Onnes [1]. He studied electrical resistivity of pure materials at low temperatures. A material possessing high purity was required for study of intrinsic properties. One of these materials was mercury - the metal in which superconductivity was first observed. Temperatures of around 1 K were reached by liquifying helium - the technique established by Kamerling Onnes three years before he discovered superconductivity, and which assured the possibility of this exciting discovery. From this time, a new era in the history of physics - superconductivity - began, and intensive theoretical and experimental study of this phenomenon, which remains one of the most interesting and sophisticated in condensed matter physics up until today, was initiated. The main properties of superconductivity are briefly outlined in this Chapter.

One of the striking properties of superconducting material is that its electrical resistivity becomes immeasurably small at cryogenic temperatures. Due to historical reasons, the electrical resistivity of mercury is presented in Fig. 1.1 [1]. As in many other metals and alloys, in which superconductivity was later observed (Fig. 1.2 [2]), the electrical resistance of mercury suddenly drops by several orders

of magnitude on lowering temperature below a certain characteristic temperature (4.15 K). This temperature, which is specific for each material, was called the critical temperature, T_c.

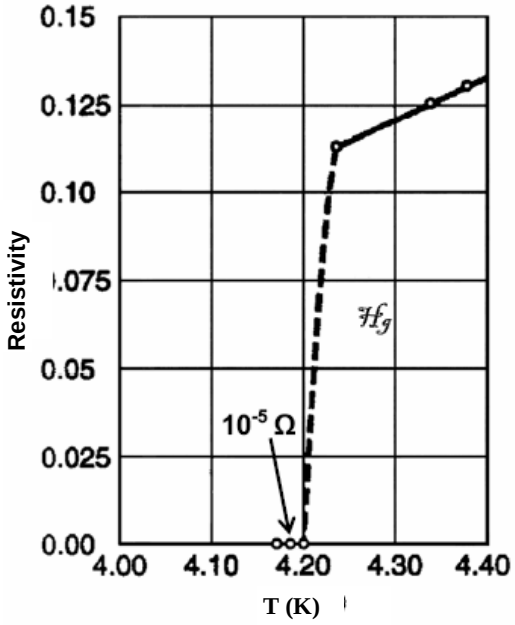

Figure 1.1: *The resistivity of mercury measured by Kamerling Onnes [1].*

In 1933, Walter Meissner and Robert Ochsenfeld discovered the second fundamental property of superconductivity [3]. They found that the material in superconducting state exhibits spontaneous, complete expulsion of magnetic flux from its volume. In their experiments, if a superconducting material was in the normal state (kept above T_c and had electrical resistance), an applied magnetic field would penetrate through the material (Fig. 1.3(a)). However, once the material was cooled below T_c (made a transition into the superconducting state), applied magnetic field was expelled from it (Fig. 1.3(b)). The reason for this is shielding currents which arise in the superconductor surface. These currents create a field inside and outside of the superconductor in such a way that magnetic fields applied and induced inside the superconductor are exactly canceled. This effect is known

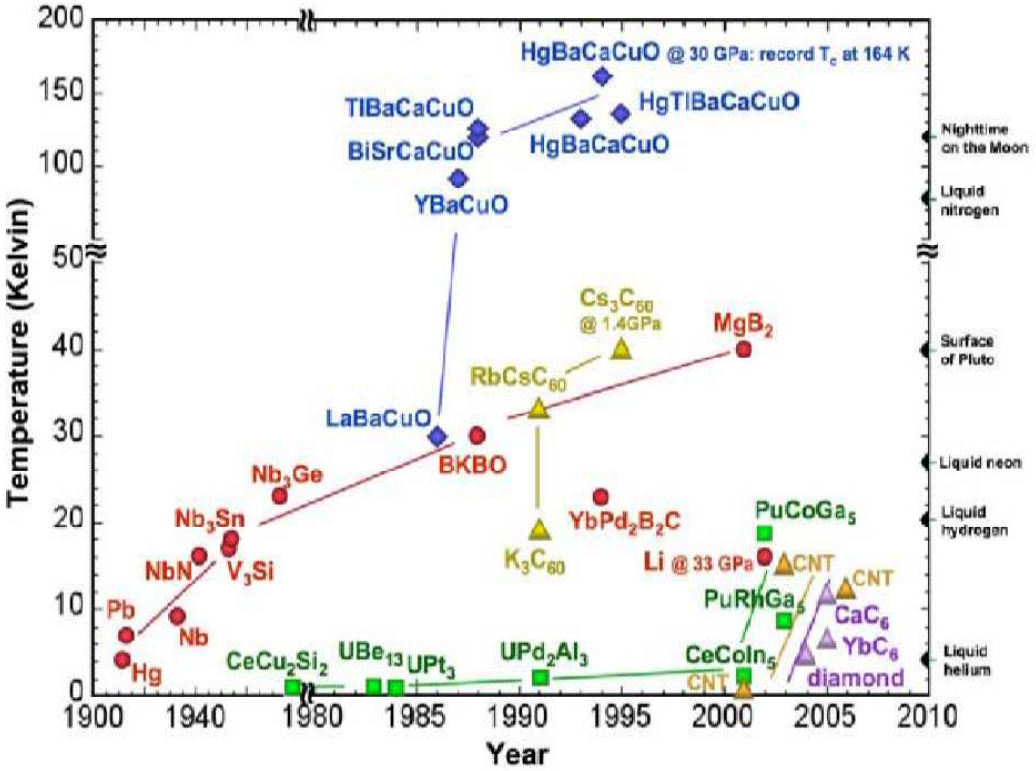

Figure 1.2: *The superconducting transition temperature (T_c) of a variety of classes of superconductors plotted as a function of time. [2]*

today as the "Meissner effect". The Meissner effect is so strong that a magnet can actually be levitated over a superconducting material.

The experimental results demonstrated that superconductivity can be destroyed by a critical magnetic field, B_c, applied to the superconductor. It was found empirically that $B_c(T) = B_c(0)[1 - (T/T_c)^2]$ [4].

The theoretical explanation of Meissner effect was offered by brothers Fritz and Heinz London in 1935. They developed a set of electrodynamic equations (called the *London equations*) [5] from Maxwell's equations. According to the London equations, the magnetic field exponentially decays from the interior of the superconductor with a characteristic decay length λ (also known as the *London penetration depth*).

A macroscopic explanation of the superconducting properties was offered by V.

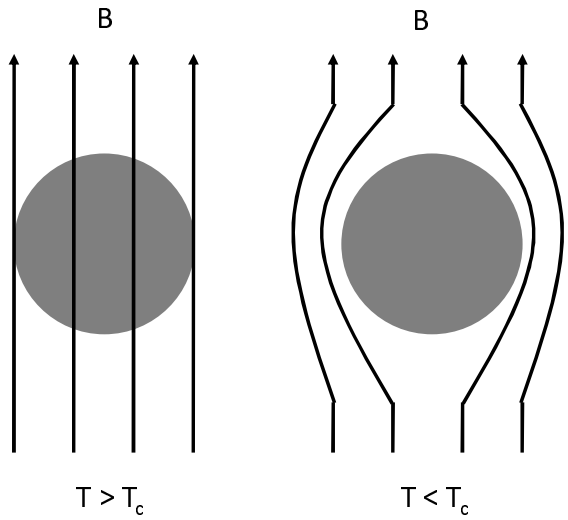

Figure 1.3: *Explanation of the Meissner effect. Magnetic field lines (arrows), are excluded from a superconductor when it is below its critical temperature.*

Ginzburg and L. Landau in 1950. They extended the London theory by introducing the order parameter ψ, which describes the local density of superconducting electrons $n_s = \mid \psi(x) \mid^2$ [6]. One of the key parameter of this theory was the Ginzburg-Landau parameter, $\kappa = \lambda/\xi$, where λ is the penetration depth and ξ is the Ginzburg-Landau coherence length.

The microscopic explanation of superconductivity, however, was proposed several years later (in 1957) by three American physicists J. Bardeen, L. Cooper and R. Schrieffer. According to their theory [7], known as the *BCS theory*, superconductivity results from the interaction between electrons and the surrounding ions in crystal. When moving in the crystal, an electron leaves behind a deformation cloud which affects the positions of the ion cores. This distortion creates an effective positive charge which attracts other approaching electrons to form an electron

pair, called a *Cooper pair*. The Cooper pairs move without scattering in the lattice, which leads to the resistance-free nature of the superconducting state. The Cooper pair has the same size as the coherence length (ξ).

Theoretical analysis of superconducting properties under applied magnetic field by A. A. Abrikosov in 1957 resulted in the discovery that by virtue of the critical magnetic field, superconductors can be categorized into two types [8]. In the case of *type I* superconductors, an external magnetic field higher than a certain critical field (B_c) destroys the superconducting state (Fig. 1.4(a)). *Type II* superconductors, on the other hand, have two critical fields: the lower and the upper critical fields, B_{c1} and B_{c2}, respectively. If the applied field B $< B_{c1}$, the material is in the Meissner state, essentially the same as the type I superconductors. When the external magnetic field is between the two critical values, $B_{c1} < B < B_{c2}$, the material is in a mixed state and above B_{c2}, the superconductivity of type II materials disappears completely as shown in Fig. 1.4(b). In the mixed state, an external magnetic flux penetrates partly into the superconducting material in the form of thin filaments, magnetic vortices. The core of a vortex is in the normal state, whereas the other part of the material is still in the superconducting state. Each vortex carries a discrete amount of magnetic flux, namely one flux quantum, $\Phi_0 = 2.07 \times 10^{-15}$ T m^2. A vortex has a normal core whose radius is the coherence length, ξ, and the magnetic field of the vortex decays on the characteristic distance of the London penetration depth, λ. Superconductors can be classified into type I and type II materials by defining the Ginzburg-Landau parameter $\kappa = \lambda / \xi$. For all type I superconductors, κ should be smaller than $\sqrt{2}$, and for type II materials, κ should be greater than $\sqrt{2}$.

Another important characteristic of superconductivity is the critical current, I_c. There is a certain maximum current that superconducting materials can carry, above which, the superconducting state will be destroyed. If the applied current

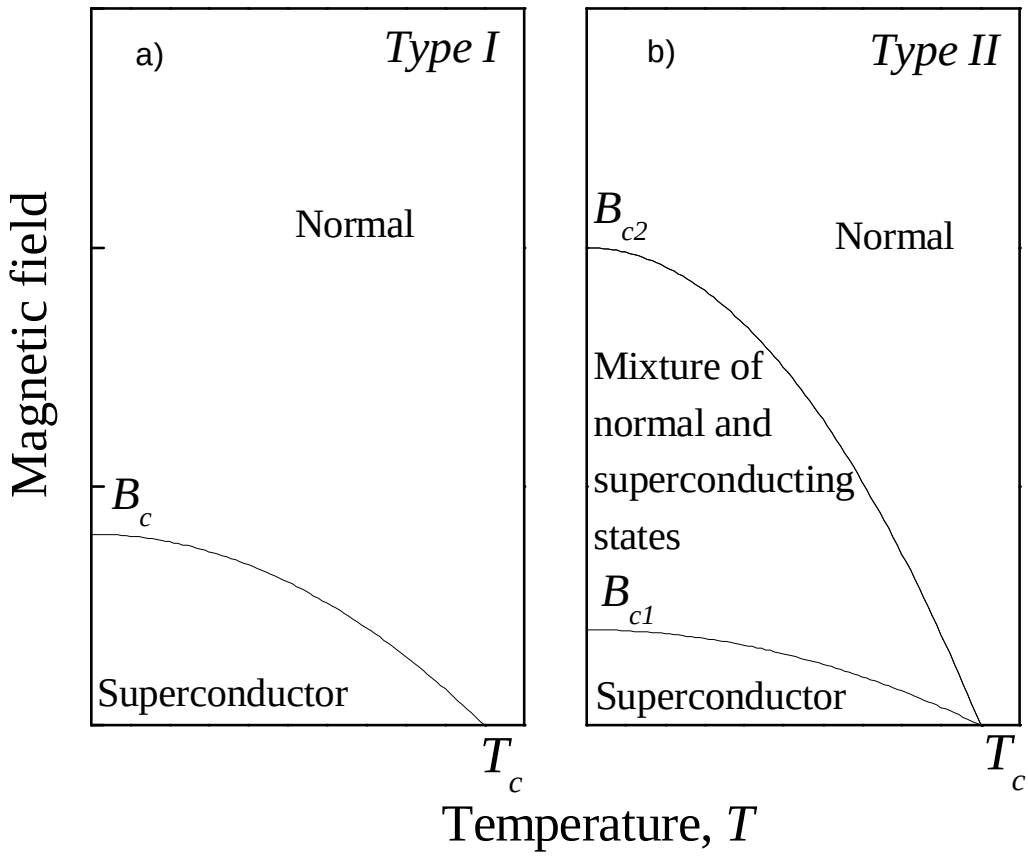

Figure 1.4: *Temperature dependence of critical magnetic field for type I (a) and type II (b) superconductors.*

exceeds I_c, it will cause the superconductor to revert to the normal state, even though it may be below its transition temperature. In type II superconductors, if $I > I_c$, the vortices start to move in the material, causing resistance and thereby losses. Luckily, there are a number of inhomogeneities in the usual materials which can trap (or *pin down*) vortices and thus increase the value of I_c. The average pinning force can be defined as $F_p = J_c \times B_a$, where J_c is the critical current density of the superconductor.

Besides theoretical work, extensive research efforts have been devoted to find ways to employ superconductors in practice. Large-scale applications of superconductors have long been limited by the necessity to cool the materials to the boiling

point of liquid helium, 4.2 K. It wasn't until the discovery of high-temperature superconductivity in 1986 by G. Bednorz and A. Müller [9] that research on superconductors took a major step forward. With the discovery of superconductivity in material classes showing a transition to superconductivity at temperatures above liquid nitrogen temperature, expectations about practical uses for these materials also came into major consideration. It is important to note that the nature of high-T_c superconductivity cannot be explained by BCS theory, and this remains an unsolved problem in modern solid-state physics.

The recent discovery of superconductivity in MgB_2 at 39 K was announced by J. Akimitsu in 2001 [10]. This was an unexpected and exciting finding, which again boosted interest in the field of superconductivity. MgB_2 superconductor possesses a number of interesting features, such as much higher T_c than in previously reported conventional superconductors and unique two-gap superconductivity. Furthermore, its high T_c, I_c, and B_{c2} values, as well as the large coherence length, low anisotropy, and absence of grain-boundary misorientation induced weak-links make MgB_2 material attractive for practical applications. Importantly, easily fabricated MgB_2 wires and tapes can be employed at working temperatures of 20-25 K, achievable by compact cryocoolers, which significantly reduce the running costs of this conductor compared to low temperature (NbTi, Nb_3Sn) superconductors.

New types of superconducting material, most recently, (2008) SmFeAsOF with T_c greater than 50 K [11] and $(Tl_4Ba)Ba_2Ca_2Cu_7O_{13+}$ (2009) with T_c of 254 K [12], are constantly being discovered. The driving force in the search for new materials is based on the desire to find superconductivity at room temperature, which would have an enormous effect on wide application of this phenomenon in a variety of applications.

Superconductors are finding their applications in diverse fields, including motors and generators, considerably reducing their weight and enhancing efficiency

[13]; fault current limiters, for use in a power transmission networks [14; 15; 16]; in medicine (Magnetic Resonance Imaging (MRI) [16] systems); in daily scientific research (the Magnetic Properties Measurement System (MPMS) and the Physical Properties Measurement System (PPMS)) [17]; in sensitive magnetometers based on the Josephson effect and Superconducting Quantum Interference Devices (SQUIDs) capable of detecting extremely weak (5×10^{-18} T) magnetic fields [18]; and nuclear fusion reactors (the International Thermonuclear Experimental Reactor (ITER)) [19] - to name just a few of them.

The work described in this thesis is devoted to enable replacement of low temperature superconductors by (middle-temperature) MgB_2-based conductors in existing superconductor-based magnets and devices, which would significantly reduce their operational cost. The important steps towards this goal is (i) to enhance electromagnetic properties (J_c, B_{c2}) of MgB_2 wires at the temperature of 20 K in order to make them competitive with characteristics achieved by conventional superconductors at cryogenic temperatures, and (ii) to assure thermal stability of conductor preventing its transition to normal state in a long-term operation cycle. In this work, chemical doping of MgB_2 compound with various C- and Fe-based materials is investigated in order to achieve enhancement of current-carrying ability of MgB_2 wires. To assure good thermal stability particularly essential for practical application of superconducting wires, the effect of Al as a stabilizer, having excellent electric and thermal conductivities, has also been explored for the first time.

Chapter 2

MgB_2 superconductor: literature review

2.1 Introduction

As a compound, magnesium diboride (MgB_2) has been available since 1953 [20]. Accidental discovery of superconductivity in this simple binary compound in 2001 [10] generated a great deal of interest in both theoretical and experimental investigations worldwide. Several surprising properties of this material were revealed during intensive fundamental studies of this superconductor that were initiated following its discovery.

The critical temperature (T_c) of MgB_2 - 39 K - is the highest among conventional Berdeen-Cooper-Schrieffer (BCS) binary compounds. For a long time, the temperature of 23 K (observed in Nb_3Ge, Fig. 1.2) was the top value in this class of superconductors. Similar to high-T_c superconductors, MgB_2 has layered structure, which leads to significantly anisotropic superconducting properties [21]. Interestingly, MgB_2 possesses two-gap superconductivity, a phenomenon which was predicted theoretically in 1959 [22], but was only obviously observed for the

first time in this compound [23].

The relatively low cost of materials and wire/tape production, promising electromagnetic characteristics, and an operating temperature at 20 K (easily reached by modern cryocoolers) make MgB_2 conductor a tempting material for applications [24].

In this Chapter, structural properties (2.2), the mechanism of superconductivity (2.3), superconducting properties (2.4), the effects of doping (2.5), and fabrication issues (2.6) as well as several examples of applications (2.7) of MgB_2 conductor found in the literature will be briefly summarized.

2.2 Crystal structure

The crystal structure of MgB_2 is shown in Fig. 2.1. This compaund has a hexagonal crystal structure with a space group that is common among diborides, *p6/mmm* [25]. Magnesium diboride consists of honeycomb boron layers separated by magnesium layers. Each Mg atom is located at the center of hexagons of B atoms.

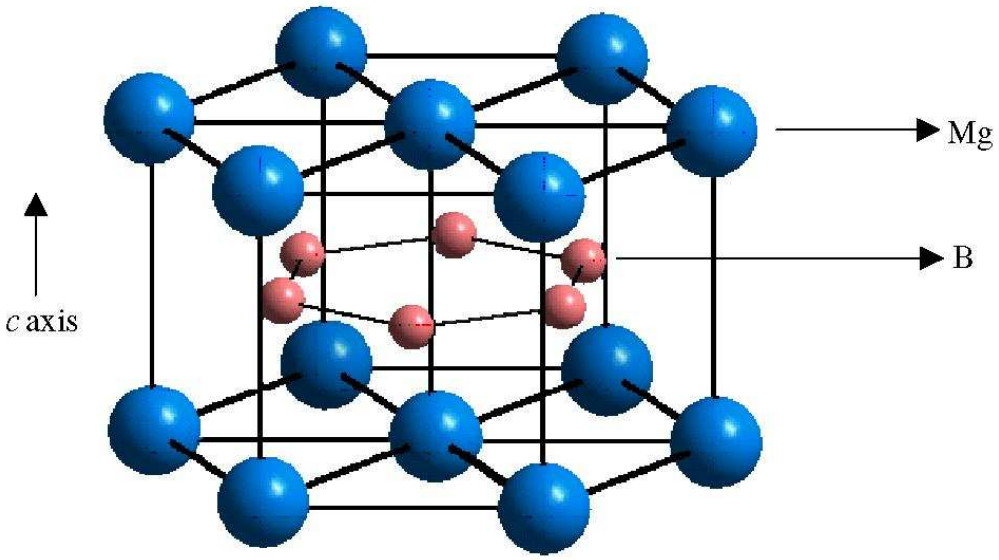

Figure 2.1: *Crystal structure of MgB_2 [30].*

The hexagonal unit cell has the in-plane $a = 3.086$ Å and out of plane $c = 3.524$ Å lattice parameters [27]. In the unit cell, the atomic positions are (0, 0, 0) for Mg and (1/3, 2/3, 1/2) and (2/3, 1/3, 1/2) for B atoms [20; 28]. The in-plane B-B distance is almost half that of the interplane B-B distance, resulting in anisotropic electromagnetic properties for MgB_2 compound [29].

2.3 Mechanism of superconductivity in MgB_2

2.3.1 Two-gap superconductivity

Theoretical investigation of two-band superconductivity in MgB_2 resulted in calculation of the Fermi surface of MgB_2 from the band structure (Fig. 2.2 [26]) and calculation of the energy gap value for each point of the Fermi surface [23].

In Fig. 2.2 the vertical sections of cylinders represent two-dimensional (2D) σ bands; and the three-dimensional (3D) tunnel-like networks are π bands. The green and blue cylinders come from bonding $p_{x,y}$ boron orbitals and are hole-like.

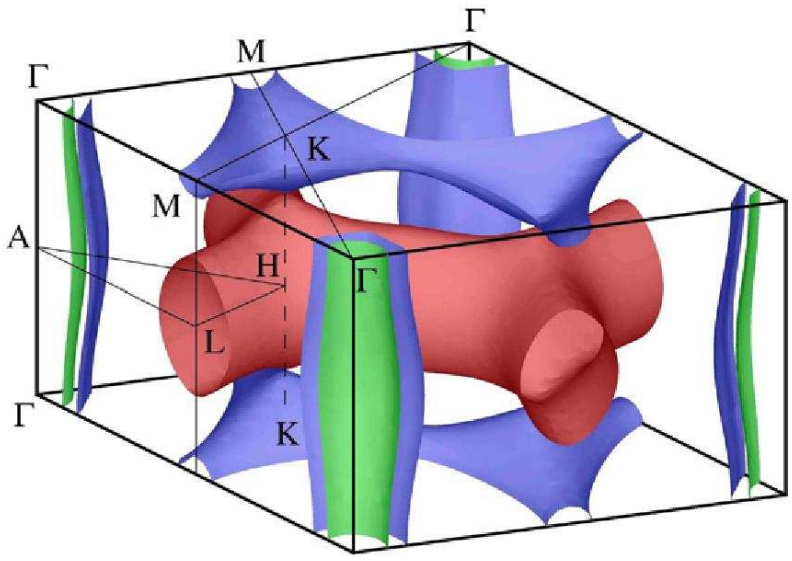

Figure 2.2: *The Fermi surface of MgB_2 [26].*

The blue tubular network (hole type) comes from the bonding p_z boron orbitals and the red tubular network (electron-like) from the antibonding p_z band [30]. Each σ- and π-band has an energy gap ($\triangle$) at the Fermi surface [23], which is reduced as the temperature is approaches the critical temperature (T_c). The energy gap of σ bands has values from 6.4 to 7.2 meV (with an average value of 6.8 meV), and on the π bands, it ranges between 1.2 and 3.7 meV (with an average of 1.8 meV) [23].

Experimental demonstration of the two superconducting gaps and their measurement has been achieved by point-contact spectroscopy [31; 32; 33; 34], tunneling spectroscopy [35; 36; 37], Raman spectroscopy [38], and photoemission spectroscopy [39; 40; 41].

The normal state conductivity in MgB_2 compound has contributions from both the covalent 2D σ band and the metallic 3D π band, however, the 2D σ band on the boron layer is responsible for the superconductivity in this compound.

2.3.2 Isotope effect. Phonon mediated superconductivity

An isotope effect gives direct evidence for a phonon-mediated mechanism of superconductivity. Generally, a critical temperature decreases with increasing isotopic mass of the superconductor, which indicates the involvement of the lattice in the superconductivity [4]. The isotope effect exponent (α) is defined as $\alpha = dlnT_c/dlnM$ (where M is the atomic mass), or for a multi-element superconductor, $\alpha = \Sigma\alpha_i = \Sigma\partial lnT_c/\partial lnM_i$ [42; 43].

Bud'ko et al. [44] measured the effect of B isotopes on superconductivity in MgB_2 and found that T_c increases by 1 K when ^{11}B was replaced by ^{10}B in this compound. They calculated the boron isotope exponent of $\alpha_B = 0.26(3)$. Following studies performed by Hinks et al [45] demonstrated that the exponent $\alpha_B = 0.3(1)$. T_c was increased by 0.1 K due to substitution of ^{24}Mg with ^{26}Mg resulting in an

Mg isotope exponent of $\alpha_{Mg} = 0.02$.

The results observed by study of the isotope effect indicated a phonon mediated BCS superconductivity mechanism with dominant B phonons contribution to the overall pairing. The BCS mechanism in MgB_2 was experimentally confirmed by photoemission spectroscopy [46], scanning tunneling microscopy [47], and neutron scattering measurements [48].

2.4 Superconducting characteristics

The properties of any superconductor can be described by its critical quantities: (i) critical temperature, T_c; (ii) critical current, I_c (or critical current density, J_c) and (iii) upper critical field, B_{c2}. Impacts of multiple gaps, as well as structural and microstructural properties of MgB_2 on these critical parameters, are summarized below.

2.4.1 Critical temperature

First reported by Akimitsu et al. [10], the transition temperature for MgB_2 is 39 K with a transition width of 1 K.

Further studies demonstrated a pressure effect on T_c of MgB_2 superconductor. T_c decreased under pressure (as in other BCS superconductors) due to the reduction of electron-phonon coupling [49]. The T_c decreased monotonically with rates varying from -1.00 to -2.00 K GPa^{-1} for both single crystal and polycrystalline MgB_2 [50]. Although the T_c decreases with pressure, remarkably, MgB_2 remains in a superconducting state (to the highest pressure studied [51; 52]) and has no structural transition up to applied pressure of 40 GPa [52]. The decrease in T_c under pressure was ascribed to an increase in phonon frequency and decrease in coupling between phonons and charge carriers [30; 53; 54; 55]. Extensive data

on MgB_2 superconductors demonstrated that T_c is reduced as a result of neutron irradiation [56; 57; 58], as well as poor crystallinity [60; 61], strain in the lattice [59; 60], doping, inhomogeneity, etc. - or any other reason resulting to the change in crystal lattice parameters of MgB_2 compound. The ways that have been tried to improve T_c of MgB_2 compound (e.g. via doping), have given disappointing results so far. However, extensive studies of other boride materials are being conducted in order to find new materials with higher T_c [25].

2.4.2 Critical current density

Critical current (I_c) is a measure of the largest current which superconductor can carry with zero electrical resistivity. If an applied current exceeds the I_c value, Abrikosov magnetic vortices start to move under the influence of the Lorentz force, resulting in interaction between the applied current and the vortex lines. Each vortex consists of a magnetic flux quantum in its normal core, which is surrounded by shielding supercurrents. The movement of vortices generates an electric field (i.e. energy dissipation) in the superconductor, which destroy superconductivity.

The critical current value depends on the size of the superconductor, and thus, for characterization of optimal conditions for different superconductors, a size independent parameter - critical current density (J_c) - is widely used. J_c is defined as the critical current per cross-sectional area of superconductor (A): $J_c = I_c/A$.

There is a fundamental limit to the current-carrying ability in superconductors. It is the current at which the coupling energy of Cooper pairs is exceeded and superconductivity is destroyed. This limit is called the depairing current density (J_{dp}) and is defined by the electronic structure of the superconducting material. Based on the Ginzburg-Landau equation [4]:

$$J_{dp} = \Phi_0/[3/\sqrt{3}\pi\mu_0\lambda^2(T)\xi(T)]. \tag{2.1}$$

Calculation of J_{dp} for MgB_2 gives a theoretical value of 8.7×10^{12} A/m^2. For comparison, the highest self-field J_c values obtained in pure High Pressure Chemical Vapor Deposited (HPCVD) thin films are 3.4×10^{11} A/m^2 at 4.2 K [62] and 1.6×10^{12} A/m^2 at 2 K [63]. For polycrystalline bulk MgB_2 samples the highest J_c(0 T, 4.2 K) reaches 10^{10} A/m^2 [64], and for MgB_2 tapes, J_c(0 T, 20 K) = 5×10^9 A/m^2 is reported in Ref. [65]. It was also established that in pure MgB_2, J_c is rather quickly suppressed by the applied magnetic field due to weak pinning in this compound.

2.4.2.1. Grain connectivity. Factors affecting current carrying ability in MgB_2

An important feature of MgB_2 superconductor was reported by Larbalestier et al. [66], who demonstrated that this material does not show weak link behaviour, in contrast to high-T_c superconductors, where weak links between superconducting grains is an important issue [67; 68]. Absence (or less pronounced) weak link behaviour was confirmed by the good agreement between magnetic and transport measurements reported in Ref. [69].

However, later on, it was realized that MgB_2 possesses other structural obstacles, which result in reduction of current carrying ability in this superconductor. In the Collings et al. topical review [70], these are referenced as extrinsic MgB_2 properties, and they include porosity and (grain) connectivity. It has been established that the magnesium plus boron *in-situ* (Mg+2B) mixture shrinks during the MgB_2 formation process due to the difference in theoretical density between the Mg+2B mixture (2.0×10^3 kg/m^3) and MgB_2 (2.63×10^3 kg/m^3). The shrinkage causes voids (pores) which can take up to 24% of the overall MgB_2 volume [71]. In addition, the low filling factor (of about 65 %) of Mg and B powders in *in-situ* fabricated MgB_2 wires further affects the level of porosity in the final

MgB_2 compound [70]. Porosity results in reduction of the effective cross-sectional area for the current flow and makes the flow highly percolative. In addition, the transparency of the grain boundaries can be reduced due to impurities distributed between MgB_2 grains, which include MgO, nano-$Mg(B,O)_2$ precipitates, or amorphous BO_x layers [72; 73; 74]. Additional impurities (secondary phases) in doped samples can further attenuate the transparency of grain boundaries.

It was first postulated by Rowell [75; 76] that normal state resistivity (sensitive to inter- and intragranular defects) can be used as a measure of effective cross-sectional area for transport in the normal and superconducting states. He proposed the equation for connectivity (e.g. electrically connected area) estimation as:

$$A_{eff} = \triangle\rho_{ideal}/\triangle\rho, \tag{2.2}$$

where $\triangle\rho = \rho(300\ K) - \rho(50\ K)$ for the particular superconductor and $\triangle\rho_{ideal}$ value is that of a fully connected MgB_2 sample (practically 7-9 $\mu\Omega$ cm, as for fully connected chemical vapor deposition made MgB_2 filaments [77]).

More extensive connectivity analysis is proposed by Collings et al [70], who extended the Rowell model, introducing parameters relative to superconducting properties of the material (e.g. Debye temperature and a material constant (K) as a measure of connectivity).

2.4.2.2. Flux pinning

The behaviour of the critical current density at applied magnetic fields (B_a), $J_c(B_a)$, can be described by a bulk pinning function, F_p. F_p is given by summation of elementary pinning forces, f_p: $F_p = \Sigma f_{pi}$ [78; 79; 80]. Summation leads to an expression of pinning force as

$$F_p = B_{c2} f(h) \tag{2.3}$$

where $h = B_a/B_{c2}$. Since in MgB_2, F_p vanishes at the actual irreversibility field (B_{irr}), in Eq. (2.3) B_{c2} can be replaced by B_{irr} [70]. The bulk pinning force normalized by its maximum value (F_p^{max}) can be described by a function: $f(h) \propto h^p(1-h)^q$, where p and q are fitting parameters. As proposed by Dew-Hughes [78], various types of pinning can be described by these parameters. "Normal" ($q = 2$) pinning (e.g. pinning by non-superconducting features), is classified as due to volume pins (for which $p = 0$); surface pins ($p = 1/2$); and point pins ($p = 1$) [78].

Intensive research on the nature of pinning in thin films and bulk MgB_2 confirmed that pinning in this material mainly occurs on grain boundaries [66; 83; 84; 85; 86; 87], as well as intragrain nano-impurities (e.g. MgO, $Mg(B,O)_2$) [73; 81; 82] and nanoscale crystal lattice defects (stacking faults, dislocations, etc) [88].

2.4.3 Critical fields. Anisotropy

Being a type-II superconductor, MgB_2 has two critical fields: B_{c1} and B_{c2}. The crystal structure of MgB_2 is anisotropic (Fig. 2.1), which results in anisotropy of superconducting properties in directions parallel to the ab-plane and the c-direction of the crystal lattice. The lower (upper) critical field parallel to the ab-plane is defined as $B_{c1,ab}$ ($B_{c2,ab}$), and parallel to c-direction as $B_{c1,c}$ ($B_{c2,c}$). Then, the anisotropy parameter, γ, is defined for the lower critical field as $\gamma_{Bc1} = B_{c1,ab}/B_{c1,c}$ and for the upper critical field as $\gamma_{Bc2} = B_{c2,ab}/B_{c2,c}$.

The values for B_{c1} estimated for polycrystalline samples at 0 K vary from 25 mT to 48 mT [25]; for single crystals estimation at 0 K of $B_{c1,c} = 27.2$ mT and $B_{c1,ab} = 38.4$ mT [89]. The γ_{Bc1} reported at low temperatures is between 1-2 [90; 91].

The temperature dependencies of the $B_{c2,ab}$, $B_{c2,c}$, and γ_{Bc2} values obtained by different techniques on single crystal are presented in Fig. 2.3. These B_{c2} values

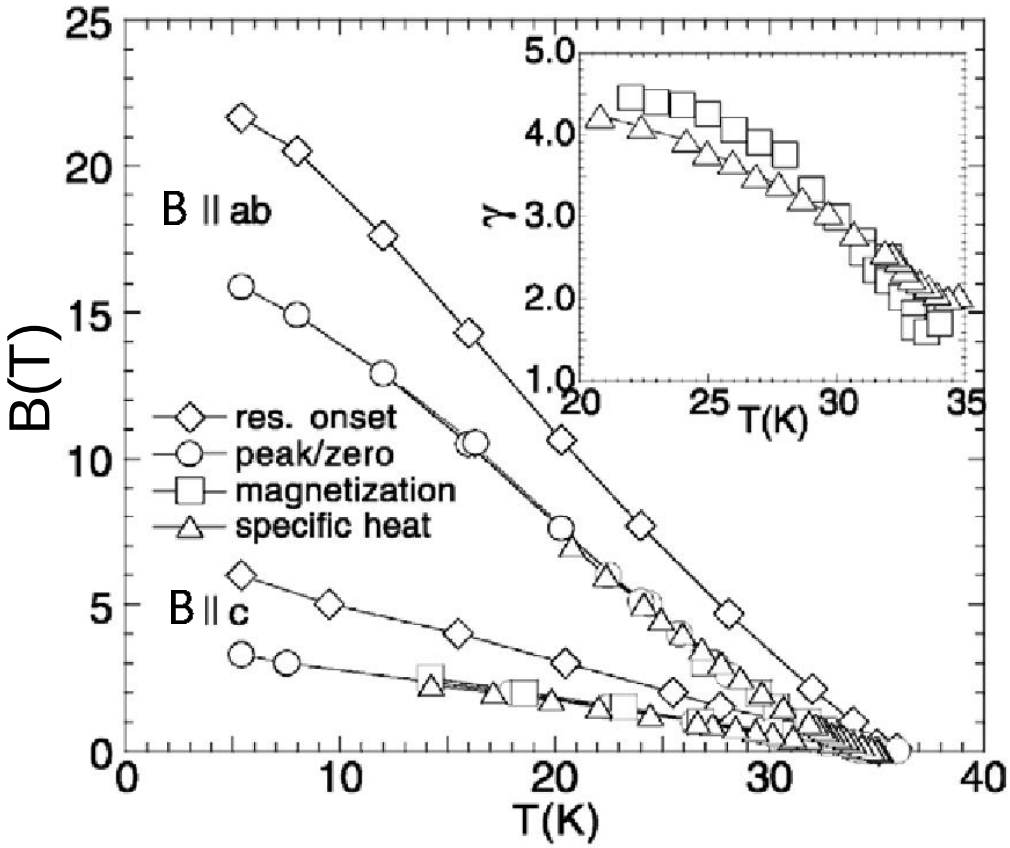

Figure 2.3: *Temperature dependence of upper critical field determined by different techniques for two field directions for a single crystal of MgB_2. The inset shows the temperature-dependent anisotropy coefficient γ [92].*

are relatively low ($B_{c2,ab}$ = 18 T and $B_{c2,c}$ = 3.5 T) compared to $B_{c2,ab}$ = 50 T obtained by Gurevich et al. [93] in thin MgB_2 films contaminated with impurities. As can be seen from the inset in Fig. 2.3, the γ_{Bc2} value is about 4.2 at 20 K(for single crystal) and decreases with increasing temperature down to about 1.5. γ_{Bc2} values of 5-6 are estimated at 0 K for polycrystalline samples [94; 95; 96].

The temperature dependence of B_{c2} for an MgB_2 sample is presented in Fig. 2.4 [97]. Surprisingly, the scaling equation valid for one-gap superconductors in the dirty limit ($B_{c2}(0) = 0.69T_c(dB_{c2}/dT)_{Tc}$ [98]) did not give satisfactory fitting results. The origin of the observed $B_{c2}(T)$ behaviour lies in the nature of the multiple

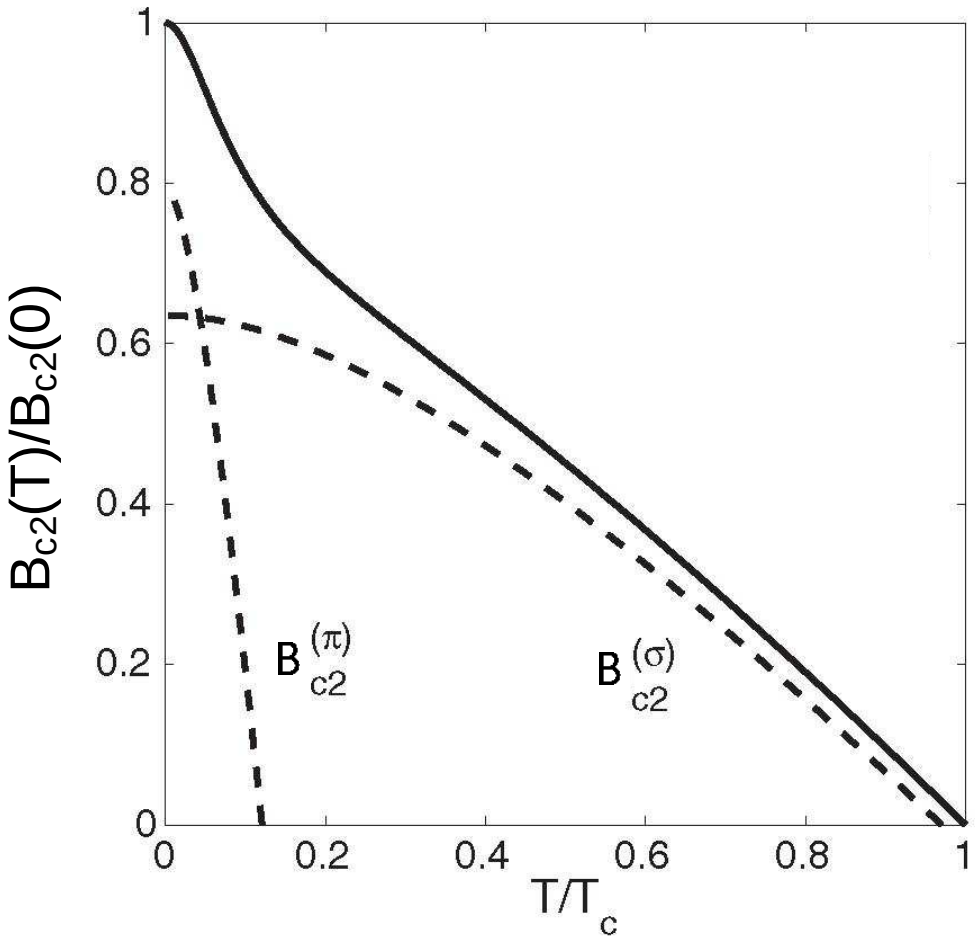

Figure 2.4: *Temperature dependence of B_{c2} for the dirty two-gap MgB_2 superconductor. The dashed curves are for σ and π films in the one-gap dirty limit. The solid curve shows $B_{c2}(T)$ calculated from the two-gap dirty-limit BCS theory [97].*

gaps in MgB_2 superconductor. An explanation of $B_{c2}(T)$ performance was given by Gurevich, who applied a dirty-limit, weakly coupled, multi-band BCS model and took into account intraband and interband scattering by non-magnetic impurities [97]. He showed that $B_{c2}(T)$ depends on which band (σ or π) is dirtier and has the higher value. Thus, if the π band is dirtier, it will have higher B_{c2} at low temperatures, and total $B_{c2}(T)$ will show an upturn behaviour at low temperatures, as schematically shown in Fig. 2.4. The experimental evidence of upward $B_{c2}(T)$ at low fields was demonstrated by Braccini et al [99], who studied thin

MgB_2 films with introduced disorder (via C-doping). Importantly, in his model Gurevich, [97] demonstrated the opportunity for further enhancement of the upper critical field by tuning the impurity scattering.

2.4.3. Coherence length and penetration depth

The coherence length (ξ) and penetration depth (λ) of MgB_2 were estimated using experimentally observed B_{c2} and B_{c1} values using the equations:

$$B_{c1} \simeq \frac{\Phi_0}{4\pi\lambda^2} ln\kappa, \tag{2.4}$$

and

$$B_{c2} = \frac{\Phi_0}{2\pi\xi^2}, \tag{2.5}$$

where $\Phi_0 = h/2e = 2.07\times10^{-15}$ Tm^2 is the magnetic flux quantum and $\kappa = \lambda/\xi$ is the GL parameter (see Chapter 1).

The values of λ reported for MgB_2 in the literature vary from 85 to 203 nm, with an average value of 140 nm [25; 100; 101]. ξ(0 K) of 5 nm was reported for polycarbosilane MgB_2 samples [77; 102], while the values $\xi_{ab} = 10$ nm (parallel to *ab*-plane) and $\xi_c = 5$ nm (parallel to *c*-direction) were reported for MgB_2 single crystal [21].

2.4.4 Summary

Summarizing the critical properties of pure MgB_2 superconductor, it is important to note that (i) the critical current density is rapidly degraded under applied magnetic field, which indicates weak pinning in the pristine material; and (ii) the upper critical field is not sufficiently high (~18 T) for pure samples.

With prospects for practical application of this material, these critical properties need to be enhanced without significant reduction of the critical temperature

of the final MgB_2 product. In order to push the properties of MgB_2 conductor towards practical application, the relatively simple method of chemical doping can be employed.

2.5 Chemical doping

Chemical doping has been extensively studied in order to enhance the superconducting properties and thus increase the potential of MgB_2 superconductor to replace low temperature superconductors (NbTi, Nb_3Sn), which have been in the market for magnet applications for the last 50 years. A brief review of the dopants studied is summarized below. Among all of them, only a few elements, namely, Al, Mn, Li, and C result in substitution in either Mg or B sites in the MgB_2 crystal lattice and therefore change the two-gap properties of MgB_2. Recently, Dou et al [103] proposed a dual reaction mechanism for SiC doping, which helps to classify all dopants in regards to their effectiveness for enhancement of superconducting properties in MgB_2.

2.5.1 Dopants substituted for magnesium in the MgB_2 lattice

Among the many doping materials studied, only three result in substitution into Mg sites in MgB_2 crystal lattice. The effects of these dopants on the physical properties of MgB_2 are summarized below.

Al doping. Al substitutes for Mg and donates electrons reducing the number of holes in MgB_2, thus suppressing T_c. The decrease in T_c is very significant: x = 0.4 in $Mg_{1-x}Al_xB_2$ results in loss of superconductivity [104]. Increasing the Al doping level from 0 to 0.09 causes a slight increase in the π-gap value, which was explained by weak interband scattering in $Mg_{1-x}Al_xB_2$ [105; 106; 107]. However,

this effect was very weak, and enhancement of B_{c2} was not observed [108]. Further increasing the Al content to about x = 0.3 resulted in reduction of both σ and π-bands [106].

Li doping. Interestingly, despite of expectations that substitution of Li for Mg would dope holes into MgB_2 and increase T_c, a slight decrease in the T_c value and MgB_2 crystal lattice distortion were experimentally observed in Li-doped samples [109]. In order to separate the effects of charge doping and lattice distortion caused by Li doping, isoelectronic AlLi co-doping in MgB_2 was studied. Comparative analysis of $Mg_{1-x}(AlLi)_xB_2$ compound with Al-doped MgB_2 suggested that superconductivity is mainly affected by Al substitution [110]. Theoretical investigation of AlLi co-doped MgB_2 demonstrated that Al dopes both σ and π bands, but Li provides holes only to the π band [111]. Since T_c is determined by the σ band, the overall effect of AlLi doping tended towards T_c reduction. Thus, reduction of T_c in Li-doped MgB_2 was ascribed to lattice distortion caused by Li doping.

Mn doping. Mn substitutes for Mg and reduces T_c even more rapidly than Al: only 2 % Mn substitution completely destroys superconductivity in MgB_2 [112]. Similar to Al doping, both gaps are reduced with increasing Mn content. Notably, Mn results in substitution for Mg. It was shown that the suppression of T_c is mainly due to magnetic pair breaking in MgB_2 caused by Mn doping [112].

2.5.2 Nano and organic C-based doping

It was experimentally found that C-based doping leads to significant enhancement in the superconducting properties of MgB_2 conductor.

C-based doping results in C substitution into B sites in the MgB_2 crystal lattice. In addition, C donates electrons and reduces the number of holes in MgB_2. According to the configuration of the superconducting gaps in MgB_2 (Fig. 2.2),

2D σ- and 3D π-bands are located in the B-plane, and thus, C substitution for B has a significant impact on the inter- and intraband scattering [27]. For C-doped MgB_2 single crystal, a decrease in the σ band and flattening of the π band with increasing C-doping content was observed [113; 114; 115]. At higher C-content ($x = 0.12$ in $MgB_{2-x}C_x$), the σ and π bands merge, providing clear evidence for interband scattering [106; 113; 116].

Generally, C-based doping results in constriction of a-lattice parameter, and leaves c-lattice parameter unaffected. This change in lattice parameter ($\triangle a$) suppresses T_c of C-doped samples.

In order to evaluate the level of C substitution (x) for B in MgB_2 crystal lattice, Avdeev et al [117] suggested an empirical equation (based on neutron diffraction data) $x = 7.5\triangle(c/a)$, where $\triangle(c/a)$ is the change in c/a compared to pure sample. It should be noted that type of dopant and sintering temperature significantly affect level of C-substitution for B in the MgB_2 samples [103].

As a result of C substitution into MgB_2 lattice and formation of impurity phases (different for each type of dopant), a dense network of nano-scale crystal lattice defects forms in C-doped samples. In addition, a number of nanoscale impurities form during heat treatment (e.g. Mg_2Si, BO_x, $Si_xB_yO_z$, BC for SiC-doping [88; 118; 119; 120], or BC, Mg_2C_3, MgB_2C-2 for C-doping [121; 122] as observed in TEM and HRTEM studies.

It is well known that in type-II superconductors, vortex lines have a normal core diameter of 2ξ. ξ is 5 nm in MgB_2 (Sec. 2.4.3), and thus, impurities and defects with sizes around 10 nm are ideal pinning centers. Many reports have demonstrated that C-based doping improves pining and thus the current carrying ability of $MgB_{2-x}C_x$ samples [103; 121; 122; 123; 124; 125; 126; 127; 128; 129; 130; 131; 132; 133; 134; 135; 136; 137].

As a result of the modification of interband and intraband scattering discussed

above, C-based doping results in a very effective enhancement of B_{c2} values. The intraband scattering in these samples is increased via shortening of the electron mean free path, ℓ [93]. As a consequence, ξ will be shortened according to the equation $1/\xi = 1/\ell + 1/\xi_0$ [93], but B_{c2} is increased according to Eq. (2.5). The observed increase in B_{c2} at low temperatures is attributed to the dirtier π band, as is demonstrated in Fig. 2.4. For instance, record high $B_{c2,ab}$ over 60 T (0 K) was observed in C-doped MgB_2 films prepared by the HPCVD technique [24; 138].

Electromagnetic characteristics for different types of C-based doping are presented below.

Nano-C doping. For 5 at% C-doped MgB_2 tape, the 5 K transport J_c reached 1.85×10^8 A/m^2 at 10 T and 2.8×10^7 A/m^2 at 14 T. The record high value of 4.2 K $J_c = 10^8$ A/m^2 at 14 T was reported for Fe-sheathed MgB_2 wire after ball milling of precursor powders [139]. B_{c2} value as high as 32.5 T was observed in CVD fabricated $MgB_{2-x}C_x$ fibers with $x = 0.038$ [140].

CNT doping. For (single wall) CNT-doped MgB_2 wire, the highest 4.2 K transport $J_c = 10^8$ A/m^2 at 14 T and 3×10^7 A/m^2 at 12 T was reported in Ref. [127]. B_{c2} value of about 40 T at 0 K was reported for double-wall CNT-doped MgB_2 [141]; $B_{irr} = 9$ T at 20 K was reported in Ref. [142].

Nano B_4C doping. The 4.2 K J_c value of 10^8 A/m^2 at 9 T was reported in Ref. [143]. For B_4C dopant, the sintering temperature can be reduced from 900°C to 800°C, which is preferable for pinning on a larger number of grain boundaries and thus $J_c(B_a)$ enhancement.

Nano SiC-doping. This is the first nano-dopant that resulted in significant enhancement of $J_c(B_a)$, $B_{c2}(T)$, and B_{irr} with small reduction in T_c (about 2 K) [133]. 4.2 K transport $J_c = 2\times10^7$ A/m^2 at 16 T was reported in Refs. [124; 134]. 4.2 K B_{c2} value of 33 T were reported for SiC-doped MgB_2 wires [144], and a value of 40 K for bulk samples sintered at temperature of 600°C [145].

Organic C-based doping. A variety of organic materials have been studied as dopants in recent years (sugar [146; 147], malic acid [148], polycarbosilane [149; 150; 151], tartaric acid [152], etc.), all showing enhancement of MgB_2 electromagnetic properties. Importantly, a small amount of sugar did not result in a degradation of self-field J_c [146]. A $B_{c2}(T)$ value of 36 T at 5 K was approximated for a sugar-doped bulk sample [147]. A high current carrying ability (5 K (magnetic) $J_c = 3{\times}10^8$ A/m^2 at 8 T), which outperforms that for nano-SiC doping, was observed in a bulk polycarbosilane-doped MgB_2 sample [149; 150].

The advantages of organic doping are (i) decomposition of organic material at low temperatures and release of highly reactive amorphous C before MgB_2 formation; and (ii) homogeneous distribution of the organic dopant within the MgB_2 matrix as a result of pre-mixing the organic dopant with B particles in liquid media [146; 148; 149].

2.5.3 Dual reaction model. Classification of dopants.

Standing foremost among other dopants, the effects of nano-SiC doping, resulting in excellent enhancement of electromagnetic performance of MgB_2 conductor, were not understood for several years. In 2007, Dou et al. [103] proposed the so-called dual reaction model, which explained the uniqueness of SiC dopant (compared to other C-based dopants) for MgB_2. Moreover, this model enabled a classification of dopants in regards to MgB_2 superconducting property enhancement.

According to Dou et al. [103], highly reactive C appears in the Mg+2B system doped with SiC due to reaction of Si and Mg, which form Mg_2Si and releases C at low temperature (~ 600°C). This fresh C is easily incorporated into the lattice of the MgB_2, which apparently forms at the same temperatures (≥ 600°C) and results in consequent enhancement of impurity scattering and vortex pinning. The SiC also takes advantage of low temperature synthesis of MgB_2, which yields small

grain size, an increase in the density of grain boundaries, and hence, enhancement of the grain boundary pinning. In addition, highly dispersed fine particles (Mg_2Si, BO_x, $Si_xB_yO_z$, BC), and the excess nanosized C can be embedded into the MgB_2 matrix, matching the coherence length of MgB_2, which makes them good pinning centers.

An important outcome of this model is that all dopants can be classified in to four groups in terms of their beneficial effects on the superconducting properties of MgB_2 [103]: *the first group* are SiC and the carbohydrates, where fresh reactive C is incorporated into the B site at the temperature of MgB_2 formation; *the second group* are materials such as nano-C, CNTs, and B_4C, which provide C substitution at higher temperatures than are required for MgB_2 formation; *the third group* are Si and a number of silicides, which can react with Mg at the MgB_2 formation temperature, but without C substitution; *the fourth group*, including compounds such as BN and MgO, has little positive, or even a negative effect on enhancement of MgB_2 superconducting properties due to the lack of any reaction or substitution up to very high sintering temperatures.

2.5.4 Some other dopants studied

Several dopants have an important (from the practical point of view) impact on MgB_2 microstructural and thus electromagnetic properties; they are summarized below.

Ti [153; 154; 155], Zr [156], and Ta [157; 158], as well as the silicides $ZrSi_2$ and WSi [159], which do not enter the MgB_2 crystal lattice, result in either absorbtion of oxygen at the grain boundaries (Ti, Ta, Zr), or improve grains connectivity, reduce porosity, and enhance pinning and J_c. Dy_2O_3 [160] and Zr doping [161] result in grain size reduction; Y_2O_3 doping [162] leads to formation of highly dispersed (YB_4) nano-inclusions; Fe_2O_3 doping materials [163] act themselves as effective

pinning centers - all of these dopants contribute to enhancement of pinning in MgB_2. However, they have less significant enhancement of MgB_2 superconducting properties compared to C-based doping.

2.6 Fabrication of MgB_2 superconductors (fibers, bulk, wires and tapes)

Based on 50 years of low-T_c (NbTi, Nb_3Sn) and 20 years of high-T_c superconductor fabrication experience, the first MgB_2 samples in the form of fibers, followed by bulk, wire, and tape were quickly fabricated. A number of techniques applied for fabrication of practical MgB_2 conductors are described in this Chapter.

2.6.1 Diffusion method

First, superconducting MgB_2 wires were synthesized by Mg diffusion into B fibres having a diameter of 200 μm [77]. These wires demonstrated self-field J_c values of 10^9 A/m^2 at 4.2 K. They also had very low normal state resistivity ρ_{40K} of 0.38 Ωcm and the high RRR value of 25.3. Some other papers on this method report formation of short wires with T_c of 39.4 K [102]; several hundred continuous wires within an Mg matrix studied in Ref. [164] had a broad transition with critical temperature of 39 K and demonstrated poor homogeneity.

2.6.2 Liquid infiltration

The reactive Mg-liquid infiltration technique enabling formation of dense MgB_2 wires was demonstrated by Giunchi et al [165]. The billet configuration for this method consists of a central Mg rod surrounded by B powder inserted into soft steel tube. An Nb tube was used as a barrier between the steel and B the powder.

After deformation, the wire was subjected to a heat treatment for 3 h at 900°C. During sintering, Mg reacted with B, leaving a hole in the center of the wire. $J_c = 8 \times 10^9$ A/m^2 was observed at applied magnetic field of 1 T at 4.2 K. This technique was also used to fabricate seven filament wires reaching $J_c \geq 10^9$ A/m^2 at 4.2 K and 4 T.

2.6.3 In-situ and ex-situ techniques

MgB_2 bulk, wire, and tape samples can be fabricated using either *in-situ* or *ex-situ* approaches.

In the ***in-situ*** method, pure Mg and B powders are mixed in a stoichiometric composition, compacted to the desired form (bulk or wire, tape) and subjected to the heat treatment procedure for formation of MgB_2 compound. The purity and size of the initial materials have a significant impact on the grain size and connectivity in the final product [74; 166; 167; 168; 169; 170; 171], demanding usage of high purity and small size precursor materials. During *in-situ* MgB_2 processing, some level of MgO impurity is always observed. If formed at the grain boundaries, MgO reduces the current flow in the MgB_2. In order to reduce the level of MgO, a number of authors have suggested replacing Mg by MgH_2 compound [119; 172; 173; 174; 175]. Since pinning on grain boundaries dominates in MgB_2 (Sec. 2.4.2.2), formation of MgB_2 with small grains is desirable. The size of grains can be controlleda and kept small by sintering Mg+2B mixture at lower temperatures (600 - 650°C). The *In-situ* technique enables effective introduction of dopants (incorporation of dopant elements into the lattice) and stoichiometry variations. For instance, it was demonstrated that some excess of Mg improves in-field properties of SiC-doped MgB_2 [125] and the low field J_c value of MgB_2 [176].

In the ***ex-situ*** approach, commercially available reacted MgB_2 powder is used.

The advantage of this method is higher density compared to *in-situ* samples [177; 71; 178]. The properties of the final MgB_2 product depend greatly on the purity and size of the starting MgB_2 powder. It was found that sintering at high (900 - 1000°C) temperatures [179] and ball milling [16; 180] of the starting MgB_2 powder are beneficial for better grain connectivity, formation of larger number of grain boundaries, and uniform distribution of MgO impurities in the final material.

2.6.4 CIP, HIP and CHPD

In order to improve density of *in-situ* or *ex-situ* MgB_2 superconductors, cold isostatic pressing (CIP) and hot isostatic pressing (HIP) can be effectively employed. A number of papers has been published on MgB_2 prepared by these techniques. These demonstrated higher density in both *in-situ* and *ex-situ* [59; 181; 82; 182; 183] formed MgB_2 bulk and short-length wires and consequently, resulted in enhancement of current carrying ability in these samples. For instance, 4 K J_c of 10^7 A/m^2 and 2.5×10^6 A/m^2 were observed in HIP-treated MgB_2 wire and its non-HIP-treated analog [59]. Authors explained the observed results by the high density of nanodefects (small angle twisting, tilting, and bending boundaries) formed in HIP treated *ex-situ* MgB_2 wires, which improved pinning, $J_c(B_a)$ and B_{irr} (up to 17 T at 4K compared to 14 T for non-HIP-treated sample) at high fields. In spite of enhancement of density, grain connectivity, and superconducting characteristics, these methods are not applicable for fabrication of long length wires.

Recently, Flukiger et al. [184] reported the effects of cold high pressure densification on *in-situ* MgB_2 wires. They demonstrated enhancement of density and grain connectivity in the final MgB_2, and an increase in J_c (by 300% at 20 K and 5 T, and by 53% at 4.2 K, 10 T) and B_{irr} (by 0.7 T at 20 K) with respect to the same wires without the application of pressure. The effect of the cold high

pressure densification was particularly pronounced at 20 K. This technique seems to be applicable to long-length wire fabrication.

2.6.5 PIT and CTFF. Sheath materials

Powder in tube (PIT) and continuous tube forming and filling (CTFF) are two widely employed methods for fabrication of mono- and multifilament MgB_2 wires and tapes.

In the PIT technique, (*in-situ* or *ex-situ*) MgB_2 powder is packed into a tube, which then subjected to deformation and an appropriate heat treatment procedures at the final size. For deformation, different routes can be used, including rotary swagging, extrusion, drawing, groove or two-axial rolling, and flat rolling [64; 133; 168; 173; 185; 186; 187; 188; 189; 190; 191], which affect core density, grain connectivity, and thus, current carrying ability of the final wire. For instance, extrusion [191] and rolling deformations [168; 173] lead to the highest core density. In contrast, drawing of wires results in lowered core density (as a result of axial strain), but such wires can be improved by employing a mechanically strong sheath material (e.g. stainless steel) [186]. Flat wire geometry observed after rolling causes undesirable J_c anisotropy in MgB_2 wires. Two-axial rolling deformation results in relatively good density, prevents flattening of wires, and is beneficial for fabrication of MgB_2 wires by PIT [192].

In the CTFF technique, precursor MgB_2 powder is dispensed onto a strip of metal, which is then moved through tube shaping dies, resulting in formation of an overlap-closed tube filled with powder in continuous lengths [193].

The sheath material has a strong influence on electromagnetic performance of MgB_2 wires/tapes. First, this material should be relatively hard to assure high density and good grain connectivity of the final MgB_2 superconducting core. Second, it should possess high thermal and electrical conductivities in order to

prevent thermal instabilities in the superconductor. Several materials have been used as a sheath material, including Fe, Ni, Cu, Ag, Nb, Ta, and their alloys (stainless steel (SS), Monel, etc.) [178; 194; 195; 196; 197; 198; 199; 200; 201; 202; 203; 204; 205; 206; 207; 208; 209].

It was found that Ag and Cu, which would provide good stabilization of MgB_2 wires, are not compatible with MgB_2. At sintering temperatures between 600°C and 900°C, *in-situ* MgB_2 reacts with these materials resulting in various (at different temperatures) Mg-Ag and Mg-Cu binary compounds between the superconducting core and the Ag or Cu sheath materials, respectively. These reactions lead to deficiency of Mg in MgB_2 and degrade the $J_c(B_a)$ performance of final the MgB_2 wires/tapes. Similarly, Ni as a sheath material forms Mg-Ni reaction layer with *in-situ* formed MgB_2 wire [210]. However, it can be effectively used for fabrication of Ni-sheathed *ex-situ* MgB_2 tapes with and without annealing [211] (Fig. 2.5 [64]).

Hard materials, such as Fe, SS, and Ta do not react with MgB_2 up to high temperatures (∼900°C) and are generally used for mechanical reinforcement or as a barrier. For instance, Fe/Cu [215; 216], Fe/SS [213; 217], Cu/Ta [218; 219], Ta/Cu/SS [220], Nb/Cu/SS [220; 221], Ta/SS [213], Nb/SS [213], and Monel/Nb [260] have been used as a sheath materials for MgB_2. Some examples showing the current carrying ability of (*in-situ* and *ex-situ*) MgB_2 wires with different sheath materials are shown in Fig. 2.5 [64].

It was found that Fe is an excellent sheath material for MgB_2 [194; 204; 215]: it is compatible with (*in-situ*) MgB_2 up to high temperatures (T<900°C) [223], assures wires with high density, and (due to the ferromagnetic nature of Fe) possesses a shielding effect, reducing the effects of an external field on the superconducting core [224]. However, in addition to its relatively high hardness, Fe does not provide good thermal stabilization, which make this material practically not applicable for

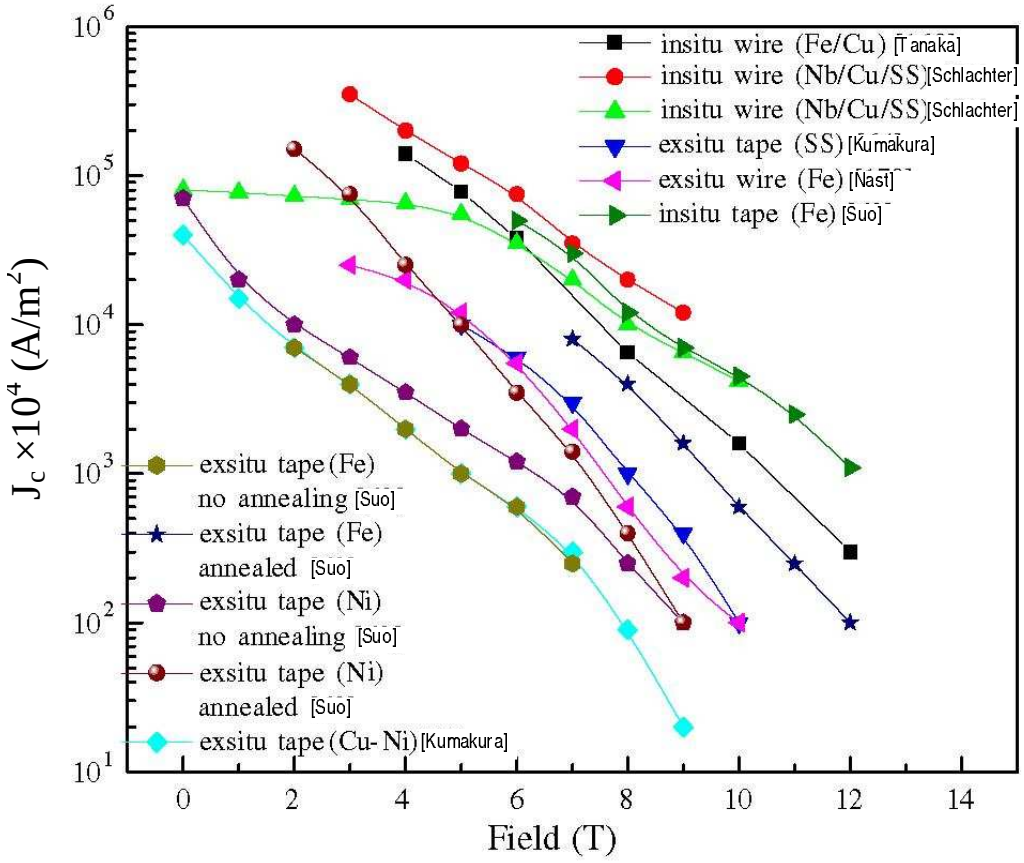

Figure 2.5: *Magnetic field dependence of the transport J_c of undoped MgB_2 conductors with different sheath materials at 4.2 K [64]. References in figure are Tanaka [212]; Schlachter [186]; Nast [213]; Suo [211]; Kumakura [214] .*

multifilament MgB_2 wire fabrication.

2.6.6 Thermal stability

Type-II superconductors operate in a mixed (normal and superconducting) state (Chapter 1, Fig. 1.4), and magnetic field penetrates into it through the normal cores. Any change in magnetic field may result in unstable behaviour of the superconductor. This is because magnetic field induces screening currents, flowing at the critical density J_c. Changes in the screening currents allows flux to move into the superconductor, which is followed by energy dissipation. Because thermal

diffusivity in superconductors is low, energy dissipation causes the local temperature to rise. For a conductor in a superconducting state, heat release of several microjoules may be enough to increase local temperature well above T_c. The resulting "hot spot" is in a normal (ohmic) state and generates more heat. If heat is generated faster than it is removed, the whole wire can transit to the normal state. Due to the large currents carryed by a superconductor, the temperature can increase to a very high value, resulting in local melting or evaporation of the superconductor. Thus, for practical application, it is necessary to enable good heat transfer from the superconductor and quickly restore the operating temperature. To minimize thermomagnetic instability in superconducting wires, normal metal with high electric and thermal conductivities should be employed as a sheath materials.

Cu or Cu-alloys are commonly used as stabilizing materials for (multifilament) low-T_c and MgB_2 superconductors [260]. However, it has long been recognized that high purity Al offers several potential advantages over high purity Cu for thermal stabilization of superconductors. It is due to its lower electrical resistivity at low temperature, low magnetoresistance, and higher Residual Resistivity Ratio (RRR) [250].

The work of this thesis pioneers the introduction of Al stabilization for MgB_2 wires, which is described in Chapters 4-5.

2.7 Market for and application of MgB_2 conductors

Since 2001, rapid R&D progress on MgB_2 towards its practical application has resulted in development of technical MgB_2 superconductor wires in kilometer-long piece-lengths [16; 193; 241]. Today, MgB_2 superconducting wires are commercially

available from three main manufacturers: Columbus Superconductors (Italy) [231], Hyper Tech Research (USA) [232], and Hitachi Cable (Japan) [233].

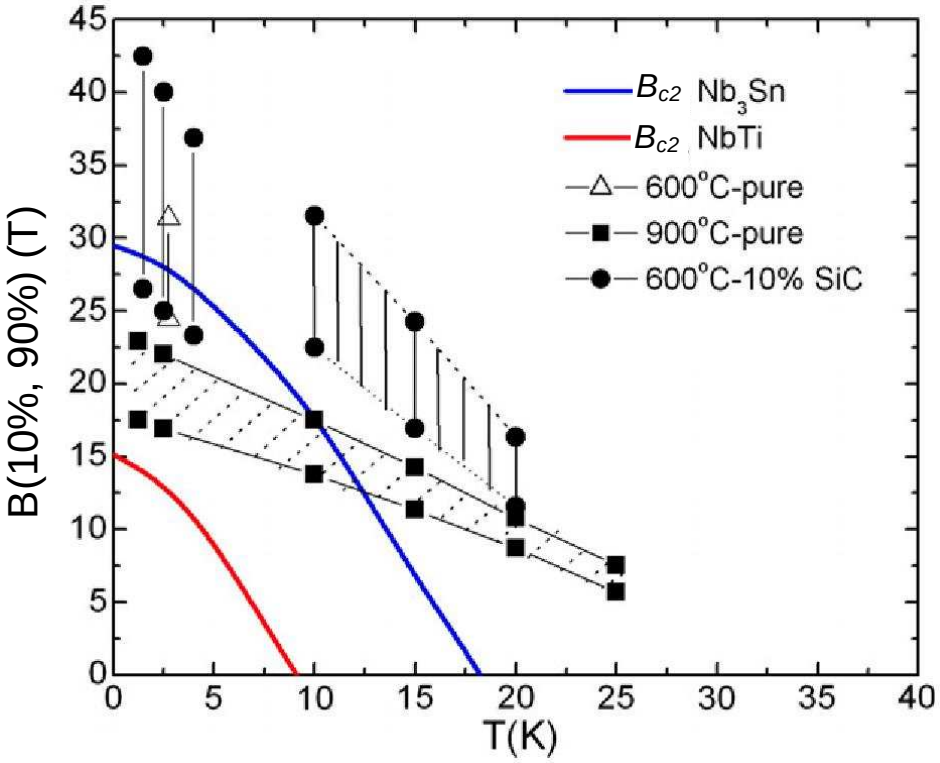

Figure 2.6: *The B_{c2} and B_{irr} values of pure and SiC-added MgB_2 sintered at 600 and 900°C, respectively. The B_{c2} and B_{irr} values were obtained from the 10% and 90% normal state, respectively. The B_{c2} values of NbTi and Nb_3Sn are also shown in the figure [234].*

Figs. 2.6 and 2.7 [234] show the superconducting characteristics of state-of-the-art MgB_2, NbTi and Nb_3Sn (low-T_c), and $Bi_2Sr_2Ca_2Cu_3O_x$ (high-T_c) superconductors. Possessing higher critical temperature (39 K), MgB_2 superconductor has a higher upper critical field compared to NbTi (T_c = 9 K) and Nb_3Sn (T_c = 18 K) (Fig. 2.6 [234]). The upper critical field (B_{c2} on the top of shaded areas), as well as irreversibility filed (B_{irr} at the bottom of shaded areas) of MgB_2 superconductor are enhanced significantly by introducing SiC dopant in MgB_2 compound, as can be seen in Fig. 2.6. As can be seen from Fig. 2.7, at the operating temperature of 4.2 K, the current carrying ability of MgB_2 doped with SiC is comparable with

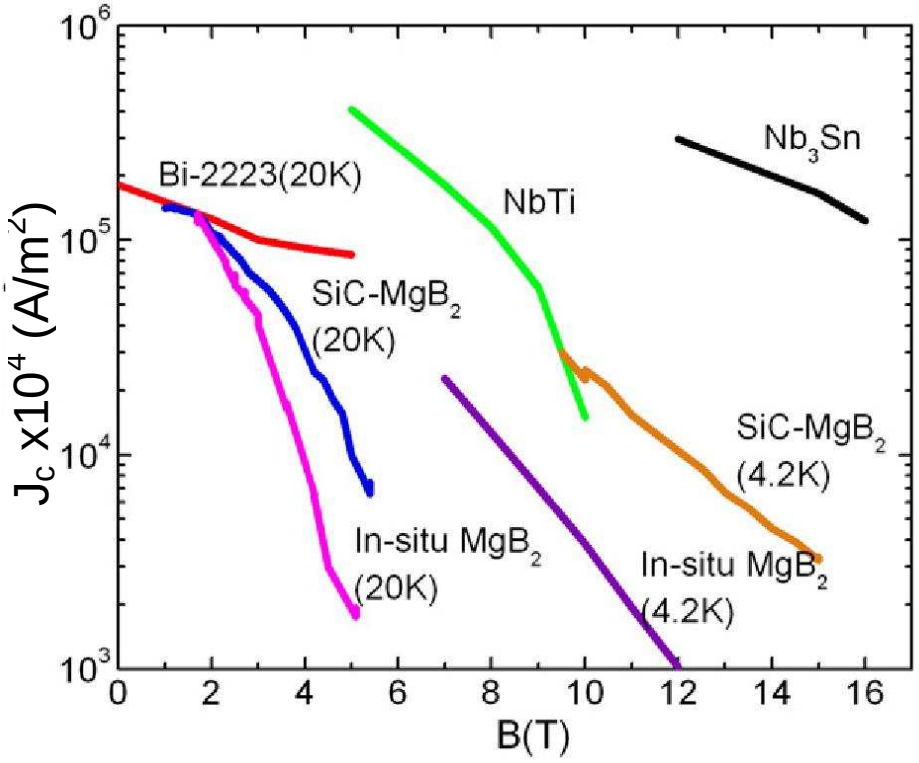

Figure 2.7: *Comparison of J_c of MgB_2 with other types of commercial superconducting wire [234].*

the performance of NbTi wires at $B_a = 9.5$ T, but it is still significantly below the performance of Nb_3Sn conductors, suggesting that there is a room for further MgB_2 improvement. At 20 K, pure and SiC-doped MgB_2 superconductors are competitive with Bi-2223 in the low field region.

For effective practical application, production and maintenance costs of superconducting devices are also crucial factors. These include materials and production costs, and coolant expenses. At the temperature of 4.2 K, the cost-to-performance ratio is estimated to be 1 Euro/kA-m at 2 T and 5 T for MgB_2 and NbTi, respectively. The costs of Nb_3Sn and Ag-clad $Bi_2Sr_2Ca_2Cu_3O_x$ superconductors are estimated at 5-25 Euro/kA-m (4.2 K, 12 T) and 50-200 Euro/kA-m (77 K, self field), respectively [236; 237].

In addition to its low cost-to-performance ratio, MgB_2 is attractive for applica-

Figure 2.8: *MgB_2 based, cryogen-free, open MRI magnet [235].*

tion at higher temperatures such as 20 K. These temperatures are easily reached by modern cryocoolers, which can significantly reduce the cooling and operation costs of superconducting devices.

The economic analysis of magnets performed in Ref. [24] indicates that MgB_2 magnets are least expensive for a field of 1 T, but that the expenses increase sharply above 1.5 T. This again shows the need for and the benefits of further enhancement of critical current for MgB_2 superconductors.

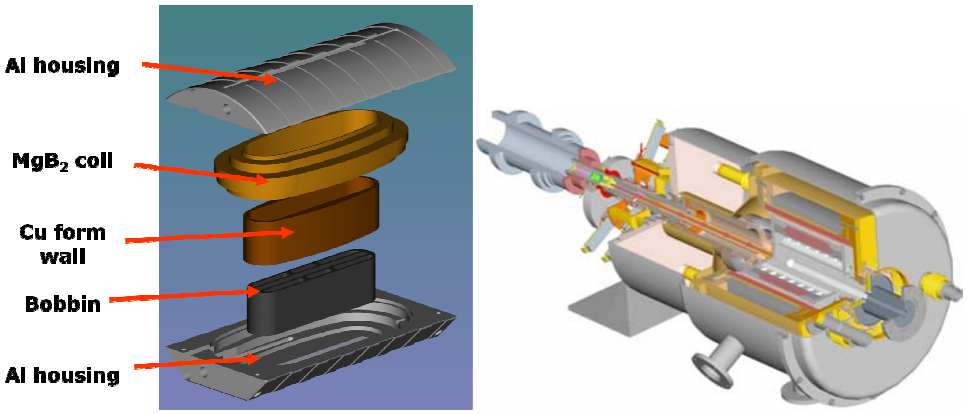

Figure 2.9: *MgB_2 rotor coils for a 2 MW generator [242].*

With the described costs and performance characteristics, MgB_2 conductor is attractive for several applications, among them, **Magnetic Resonance Imaging (MRI) magnets**. The prototype of first cryogen free MRI magnet was made by ASG Magnet using MgB_2 wires provided by Columbus Superconductors and is shown in Fig. 2.8 [235]. The preliminary results [16] confirmed that the 18 km of MgB_2 conductor used to wind the coils are satisfying the requirements of this MRI system. The magnet immediately reached its nominal current of 90 A with a central field of 0.5 T [16]. The first MgB_2 based MRI magnets will be out in the market as soon as the tests and the full industrialization are successfully completed.

With its potentially low cost, ability to operate at moderate temperatures (20 - 25 K), and very sharp ($\sim$ 1 K) transition from the superconducting to the normal state, MgB_2 is very attractive as a cost-effective resistive-type **superconducting Fault Current Limiter** (FCL) element. Results have been reported on the current limiting properties of different kinds of MgB_2 wires at 50 Hz in the temperature range of 20 - 30 K [238; 239; 240]. MgB_2 wires showed good limiting properties, characterized by a fast transition to the normal state and a limiting effect without damage to the wire samples.

MgB_2 is also attractive for application in **motors and generators** replacing existing NbTi conductors with lighter MgB_2 wires working at higher (20-25 K) temperatures [241]. Fig. 2.8 shows the design of a superconducting electric generator (right) [242] and a conceptual model of an MgB_2 rotor coil in the rotor coil pack (left) [193]. For this purpose, Hyper Tech Research made racetrack MgB_2 coils from a 580 m continuous piece of MgB_2 cable using the wind-and-react approach. The best performing coil reached 400 A at 4 K [193]. The superconducting generator demonstration will be a 2 MW generator operating at 20 K in liquid H_2.

Other possible applications of MgB_2 superconductor include adiabatic demag-

netization refrigerators, magnetic separation, magnetic levitation, superconducting magnetic energy storage, and high-energy physics applications. The feasibility of these applications is analyzed in Ref. [241].

Chapter 3

Experimental techniques

3.1 MgB_2 sample preparation

In this work, *in-situ* pure and doped MgB_2 superconductors were fabricated. High purity (99%) powders of magnesium (- 325 mesh) and amorphous boron (-325 mesh) were used as starting materials. These are the highest quality precursor powders which were available for conducting this work. The major impurities in these powders are oxides (oxidized surface of Mg powder and B_2O_3 impurities in boron), which result in the formation of MgO impurities in the *in-situ* synthesized MgB_2 compounds. The level of these impurities should be kept low in order to minimize an amount of MgO impurities and its effect on the current flow in MgB_2 as explained in previous chapter. Doping materials (Fe, Fe_2B, SiO_2 coated Fe_2B, SiC, C_2H_6Si, and $C_{12}H_{22}O_{11}$) were used in the form of nanosized powders with sizes and types specified in each specific chapter. Samples were prepared in the form of *bulks* and/or short length *wires*.

3.1.1 Bulk samples

Powders of Mg and B were weighed out in the proportion of 1:2 and hand mixed by mortar and pestle. Pellets 10 mm in diameter and 3 mm in thickness were made under (maximum) uniaxial pressure at 10 tonne press. They were sealed in Fe tubes and annealed in a tube furnace at different temperatures and for different times (specified in each following chapter). The heating rate was 5 °C/min, and the cooling time was 14 h, which corresponds to natural cooling of the furnace to room temperature. The heat treatment procedure was conducted in flowing high purity Ar gas under ambient pressure in order to avoid oxidation of MgB_2 material.

3.1.2 Wire samples

In this work, Fe-sheathed MgB_2 wires were fabricated by the Powder-In-Tube (PIT) technique [118; 133]. This includes the following steps:

First, mixing of Mg and B powders in the stoichiometry of MgB_2. Then the powder mixture was packed into a clean Fe tube having an outside diameter of 10 mm and a wall thickness of 1.5 mm. One end of the tube was sealed with a piece of Al foil.

Second, the Fe-MgB_2 composite was drawn through the conical hole of successive round dies at a speed of a few cm/s. The deformation of the composite rod was about 17 % at each size of the die. Final Fe-sheathed MgB_2 wires had diameters of 1.42 or 1.00 mm.

Third, wires were cut in several short pieces and sealed in an Fe-tube. The annealing was conducted in a tube furnace in flowing high purity Ar gas at different temperatures and for different times (specified in according chapters) for formation of superconducting MgB_2 phase.

3.1.3 Aluminizing technique

In order to study the effects of Al as a stabilizer for MgB_2 wires, an aluminizing technique was developed and realized. Open-plan melting furnace with an Al_2O_3 crucible was modified for conducting the aluminizing procedure on Fe-sheathed MgB_2 wires (Fig. 3.1). Since MgB_2 is easily oxidized at higher temperatures, it was required to reduce oxygen by passing high purity Ar gas over it under the ambient pressure. For this purpose, a stainless steel cup with an inlet for Ar gas fully covered crucible was prepared. Al was melted inside the crucible at temperatures $\geq 650\ ^oC$, as specified in subsequent chapters. The temperature of hot aluminizing procedure was controlled by thermocouple immersed inside the Al bath. Fe-sheathed MgB_2 samples were immersed in a molten Al bath through the hole on the top of the protective shroud.

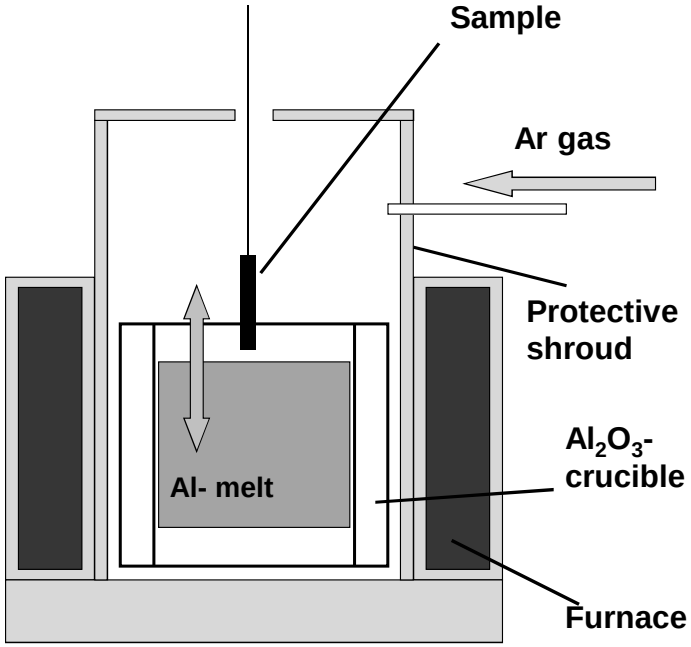

Figure 3.1: *Melting furnace modified for hot aluminizing of Fe/MgB_2 wires.*

3.2 Phase and structure characterization techniques

All synthesized MgB_2 composites and some dopants were analyzed by X-ray diffractometer (XRD) and by Scanning and Transmission Electron Microscopes (SEM and TEM).

3.2.1 X-ray diffraction

X-ray examination was carried out using a Philips PW1730 instrument, which was fully automated and configured in a Bragg-Brentano focusing geometry with 2θ optics. In all X-ray investigations, monochromatized CuK_α radiation from a

normal focus X-ray tube was used, having wavelengths of $\lambda_{K\alpha 1} = 1.5405$ Å and $\lambda_{K\alpha 2} = 1.5443$ Å.

XRD study was performed on powdered samples. The sheath material of the MgB_2 wires was mechanically removed, and the superconducting core or pellet samples were ground into powder, which was attached to the glass slide by a drop of ethanol for XRD study.

The detection sensitivity of our XRD instrument is 5 wt.%, and thus, phases with volume ratios less that 5 wt.% would not be detected. Bragg's law was used to index peaks in the XRD patterns [243]: $2d \sin\theta = n\lambda$, where n is an integer, λ is the radiation wavelength, θ is the diffraction angle, and d is the inter-planar distance. The lattice parameters were calculated from the positions of the (110) and (002) MgB_2 peaks, which correspond to the a and c-lattice parameters, respectively, or by fitting XRD patterns using the Rietveld refinement method.

3.2.2 Scanning electron microscopy

Microstructure of MgB_2 samples was investigated with help of the JEOL 6460 Scanning Electron Microscope (SEM) based at ISEM, University of Wollongong. The imaging was performed using the secondary electron detector. The resolution of the instrument is about 20 nm, with of maximum magnification of 35,000 times. Microstructure analysis of bulk MgB_2 was performed on fractured samples attached to carbon tape, while samples in the form of wire required special preparation. Short wire samples (3 mm in length) were prepared by cold mounting the wires in Strues Epofix epoxy resin. The polishing of mounted samples was performed using SiC polishing papers with sizes from 600 to 2400 mesh, followed by fine polishing with 5-1 micron diamond paste. Epoxy mounted and polished samples were coated by a thin layer of carbon in order to make samples conductive.

3.2.3 Transmission electron microscopy

Transmission Electron Microscopy (TEM) has much higher resolution (down to 0.2 nm), when compared to SEM [244]. TEM can be used for analysis of fine structures on the atomic scale using electron beam energies in the range of 60 to 350 keV. In this work, TEM investigation was carried out with help of a JOEL JEM 2011 unit (based at the University of Wollongong). The maximum beam energy for this instrument is 200 keV, which corresponds to an electron wave length of 0.0025 nm. TEM was used for observation of the grain size of pure and doped MgB_2 samples, analysis of nanostructures of secondary phases, and visualization of crystal lattice defects. In contrast to SEM, where the image is formed by electrons reflected from the surface of the sample, the TEM collects the electrons, which are transmitted through the sample. Thus, specimens for TEM should be very thin. In this work, pure and doped MgB_2 samples were prepared by Focused Ion Beam (FIB) milling in the University of New South Wales, Sydney. Samples of 100 nm thick and 5 micron long were prepared and placed on a holey-carbon coated copper grid for TEM study.

3.3 Electromagnetic characterization of samples

Superconducting properties of pure and doped MgB_2 samples were investigated by magnetic and transport measurements.

3.3.1 Magnetic measurements

Magnetic measurements were carried out using a Physical Property Measurement System (PPMS, Quantum Design). The critical temperature, T_c, was defined as the onset of superconducting screening determined by measuring the real part of the ac susceptibility. The measurements were done in a magnetic field of 25 Oe.

The absolute value of the dc magnetization was measured on a sample with an applied constant field. The sample was moved through the entire detection coil. The pick-up coil detects the waveform signal from the sample. The signal is then fitted with the known calibration waveform, with the magnetic moment of the sample being a fitting parameter.

Magnetic critical current density, J_c, was calculated from the measured magnetic hysteresis loop assuming that $J_c \sim \triangle M$, where $\triangle M$ is the width of the hysteresis loop. The calculation of magnetic J_c from the dc magnetization loop is based on the critical state model [245].

The magnetic J_c were calculated using the following relations [246]:

i) for a bar shaped sample:

$$J_c = 20\frac{\Delta M}{a(1 - a/3b)}, \tag{3.1}$$

where a and b are the dimensions of the sample perpendicular to the magnetic field ($a < b$).

ii) for a cylindrical sample with long dimension parallel to the applied magnetic field:

$$J_c = 30\frac{\Delta M}{d}, \tag{3.2}$$

where d - is the diameter of the cylinder.

iii) for a cylindrical sample with long dimension perpendicular to the applied magnetic field:

$$J_c = 30\pi\frac{\Delta M}{4d}. \tag{3.3}$$

In Eqs. (3.1)-(3.3) the units used are for J_c in [A/m^2], for ΔM in [emu/m^3], and for a, b, d values in [m].

It was found that magnetic J_c of MgB_2 material is sample size dependent [247; 248], thus, all samples for magnetic measurements were shaped to the size

of 1×2×3 mm for bulk samples and to a length of 3 mm for samples in the form of wire. In this work, the dc magnetization of samples was measured in a time-varying magnetic field with a sweep rate of 0.005 T/s and amplitude of up to 8.5 T at temperatures of 5 and 20 K.

3.3.2 Transport measurements

In this work, the four probe technique was used for measurement of transport critical current, I_c. Four contacts (two outer contact for current and two inner for voltage) were directly attached to the sample. The measurements were performed by the group led by Prof. Babic in the University of Zagreb, Croatia. In their set up, I-V curves were measured using a 0.5 ms long pulse of current (rectangular pulses with a maximum current of 320 A) at 20 K and 5 K. A magnetic field was applied parallel to the wire. The criterion for I_c definition was 1 μV/cm. The transport critical current density, J_c, was calculated by dividing I_c by the cross-sectional area of the MgB_2 core.

The four probe method was also employed for resistivity measurements of the superconducting core of the wires or bulk samples, which was performed on the PPMS (Quantum Design). The current and voltage contacts were attached to the surface of the sample by silver paste. The measurements were done in magnetic fields up to 8 T at current density of 1.3x10^4 A/m^2. The upper critical field, B_{c2}, and the irreversibility field, B_{irr}, were defined from the temperature dependence of the resistivity $\rho(T)$ measured at different fields, using the relations:

$$\rho(B_{c2}) = 0.9\rho(T_c); \tag{3.4}$$

and

$$\rho(B_{irr}) = 0.1\rho(T_c). \tag{3.5}$$

Chapter 4

Powder-in-tube and solid-state diffusion approaches for fabrication of Al-stabilized MgB_2 superconductor

4.1 Introduction

Since the discovery of superconductivity in MgB_2 [10], this material has been produced in different forms - bulk, tapes, and wires. For practical application of superconductors, wires and tapes with high critical current are necessary. Considerable work has been done to investigate and optimize the properties of MgB_2 wires and tapes with different sheath materials such as Ag, Cu, Monel, Ni, Nb, stainless steel, and Fe (see for example [194; 204; 207; 266; 267; 268; 269; 270; 271] and references therein). Chemical compatibility with MgB_2, high hardness, low specific weight, and the low price of Fe make it the most suitable sheath material for fabrication of long length MgB_2 wires and tapes. However, Fe creates a low

thermal conductivity ($\lambda_{20K} = 15.4$ W/cm K) barrier for heat sinking to the cryogen bath or cryocooler. This can result in thermomagnetic instability [224] and trigger the transition from the superconducting to the normal state in superconducting coils at high currents due to avalanche-like heat release.

It is well known that one of the most important goals for practical large current applications of wires/coils is good thermal stabilization. To minimize thermomagnetic instability in superconducting MgB_2 wires sheathed in iron, a normal metal with high electrical and thermal conductivity, such as Cu or Al, can be used for stabilization. It has been long recognized that high purity aluminum offers several potential advantages in the stabilization of superconductors.

First, over a wide range of temperatures, the resistivity of Al (pure and alloys) is lower than the resistivity of pure Cu (Fig. 4.1, left). Furthermore, Al has a high residual resistivity ratio (RRR = $\rho_{300\ K}/\rho_{10\ K}$). High purity Al (99.995%) with RRR of 5000 is commercially available [225], while high purity coppers (OHFC, C101, >99.99%) have in-service RRRs within the range of 100 to 200 [226; 227]. Given such values (e.g. $RRR_{Al} = 4000$, $RRR_{Cu} = 150$) the advantage in electrical resistivity at 10 K is obviously 27:1, and in thermal conductivity is 9:1 [252]. Under applied magnetic fields, RRR_{Al} decreases rapidly between 0 and 1 T from 5000 to 4000, and then drops from 4000 at 1 T to 1000 at 5 T [228]. In case of Cu, RRR_{Cu} decreases uniformly from 70 at 0 T to 30 at 5 T [252]. Nevertheless, $RRR_{Al} \gg RRR_{Cu}$ over the entire field range of 0-5 T.

Second, Al has higher thermal conductivity at low temperatures than Cu (Fig. 4.1, right). At the temperature of 20 K, the thermal conductivity of Al (99.995%) is 117 W/cm K, while for Cu (99.99%), it is 108 W/cm K [229].

Third, aluminum has lower magnetoresistance than copper [230]. The rate at which the resistance of aluminum rises with transverse magnetic field diminishes substantially between 1 and 2 T [225], whereas the resistance of copper continues

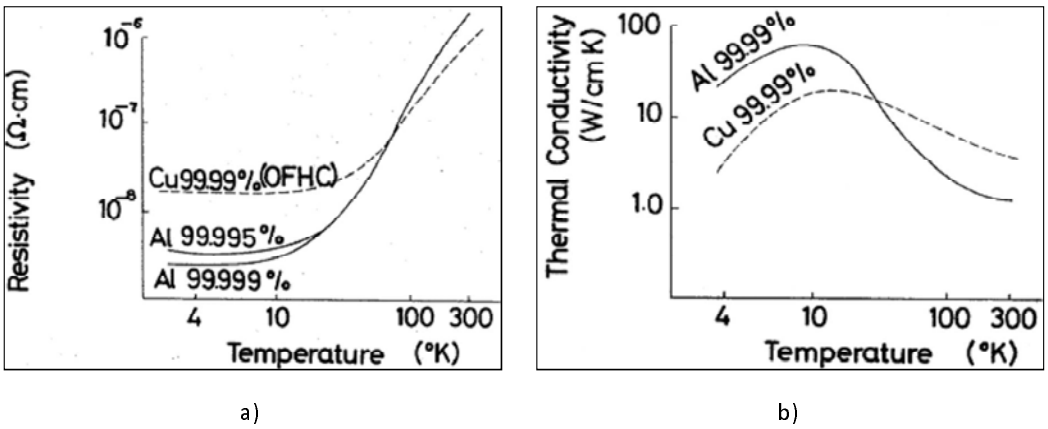

Figure 4.1: *Temperature dependence of resistivity (a) and thermal conductivity (b) for Al and Cu [226].*

rising at a steep rate. This characteristic makes aluminum favorable for application in high magnetic fields.

Fourth, Al has lower density: the density of Al (2.70 g/cm^3) is approximately 1/3 that of copper (8.86 g/cm^3) [229]. Low density of the stabilizing material results in lower weight of superconducting wires or devices.

Fifth, Al has a low collision cross section and is effectively transparent to most particles of interest in high energy physics experiments.

However, application of Al as a stabilizer has been limited due to serious difficulties associated with the manufacture and use of aluminium stabilized (low-T_c) superconductors. These difficulties have included the low melting temperature of Al (Nb_3Sn with reaction temperature $> 650°C$ cannot be made using Al), incompatible mechanical properties and processing technology (compared to Cu stabilized NbTi), and poor joinability [226]. In order to overcome these difficulties, different approaches have been employed including the technologies of radial wrapping, linear wrapping, molten metal dip coating, extrusion, and electroplating. Numerous attempts have been made to provide Al stabilization in NbTi-based low temperature superconductors [253; 254; 255; 256; 257]. However, in association with already formed NbTi/Cu, Al was used for cryogenic stabilization in particle-

detector magnets such as the Compact Muon Solenoid (CMS) [258; 255] and the Toroidal Large Hadron Collider Apparatus (ATLAS) [259].

Al appears to be an attractive stabilizer for MgB_2 wires, because it will allow the production of cheap and lightweight superconducting wires, suitable for application even in the aerospace industry. Assuming a stabilizer-to-superconductor volume ratio of 2:1 the density of Al/MgB_2 conductor is a factor of 3.0 lower than that of Cu/NbTi. However, direct employment of Al for fabrication of Al-sheathed MgB_2 wire by the *in-situ* process will result in serious damage or even loss of superconductivity in case of a reaction between the Al and the unreacted Mg+2B powder during the sintering process [104; 273]. On the other hand, the $J_c(B_a)$ performance of as-drawn Al/MgB_2 *ex-situ* wires is not high enough, due to the low mechanical strength of the Al (see for example [274] and references therein). Application of the final processing step in the fabrication of *ex-situ* MgB_2 wires (their heat treatment at a temperature of 900°C [179; 194] resulting in $J_c(B_a)$ improvement) is restricted by low melting point of Al (660°C).

At the time when this work was started, the *in-situ* solid-state-diffusion formation of MgB_2 at the temperature of 600°C was first demonstrated by Fujii et al [173]. The sintering temperature of MgB_2 compound was below the melting points of Mg and B, and thus the formation of MgB_2 occurs by solid state diffusion of Mg into B [173]. Later on, these results were confirmed by Soltanian et al [251], Yamamoto et al. [249] and our work [252].

In this chapter, the solid-state-diffusion approach has been further developed as a means for processing Al-stabilized MgB_2 wire. The structural and superconducting properties of MgB_2 samples sintered in the range of temperatures from 600 to 630°C have been systematically investigated. The compatibility of Fe and Al at these temperatures has also been studied. Since practical application of MgB_2 wires for high (in-field) current applications became possible with introduction of

SiC doping in MgB_2, the properties of SiC-doped MgB_2 wires have also been tested with Al used as a stabilizer.

4.2 Samples and experimental techniques

Fe-clad MgB_2 wires were prepared by an *in-situ* reaction method and the standard PIT technique [118; 133]. Powders of magnesium (99%) and amorphous boron (99%) were well mixed for fabrication of pure MgB_2 compound. For fabrication of SiC doped MgB_2 wire, 10 wt.% SiC nanoparticle powder (with size of 10-100 nm) was added to a mixture of Mg:2B with the atomic ratio of MgB_2.

Fe tubes were used that had an outer diameter of 10 mm, a wall thickness of 1 mm, and the desired length with one end of the tube sealed. The mixed powders were packed into the tube, and the remaining end was blocked using an aluminium bar. For fabrication of Al-stabilized pure and SiC-doped MgB_2 wires, the Fe-clad (pure or SiC doped) MgB_2 composite was inserted into an Al tube, which had an inside diameter of 10 mm and a wall thickness of 1 mm. Al alloy 6060 with 99 wt.% Al, 0.5 wt.% Si, and 0.4 wt.% Mg was used in this work. The Al/Fe-clad (pure or SiC-doped) MgB_2 composites were drawn or groove-rolled to a 2.0 mm outer diameter. The Fe- and Al/Fe-clad MgB_2 wires were sintered in a tube furnace at 600-650°C for 30-180 min, and finally furnace-cooled to room temperature. High-purity argon gas flow was maintained throughout the sintering process.

The phase investigation was performed using an X-ray diffractometer with CuKα radiation. The magnetic $J_c(B_a)$ characteristic for the superconducting cores extracted from the wires were measured at 5 and 20 K using a Physical Properties Measurement System (PPMS, Quantum Design) with applied magnetic field up to 8.5 T. The magnetic $J_c(B_a)$ was derived from the Eq. (3.2).

4.3 Phase and crystal structure analysis of MgB_2 compound

Fig. 4.2 shows XRD patterns for the Fe- and Al/Fe-clad MgB_2, and for the Al/Fe/SiC-doped MgB_2 samples annealed at 600°C for 30 min and 180 min respectively.

It should be noted that all samples have small traces of unreacted magnesium as a result of the relatively low sintering temperature (below the melting temperature of Mg). However, the majority of peaks are related to MgB_2 phase in the pure MgB_2 and Mg_2Si phases in the SiC-doped MgB_2 samples. The results observed imply that annealing of samples at a temperature of 600°C for 30 min is sufficient for fabrication of pure samples, while SiC-doped MgB_2 samples require longer annealing time (180 min) for reaction at this temperature.

We note that there are strong peaks of Mg_2Si in the SiC doped samples annealed at 600°C (Fig. 4.2(a)). As reported in previous work [103], Mg_2Si forms at a temperature of about 600°C, releasing fresh carbon, but it decomposes with increasing sintering temperature and disappears as the temperature reaches about 900°C. Nanosized Mg_2Si particles are highly dispersed in the MgB_2 matrix and play an important role in flux pinning (Chapter 7).

As Al is much softer compared to Fe, it is expected that after drawing the precursor powder, the density of the Al/Fe-clad MgB_2 wires may be reduced compared to Fe-clad MgB_2 samples. Indeed, at T = 600°C, the higher packing density of the Mg+2B mixture facilitate solid-state formation of MgB_2 phase. Slightly higher values of the FWHM of the (101) MgB_2 peak for Al/Fe-clad MgB_2 wire (FWMH(101) = 0.707°) were observed, which indicates slightly deteriorated crystallinity in this sample compared to Fe-clad MgB_2 samples (FWMH(101) = 0.677°). However, the XRD patterns for the two undoped samples (Fig. 4.2) demonstrate

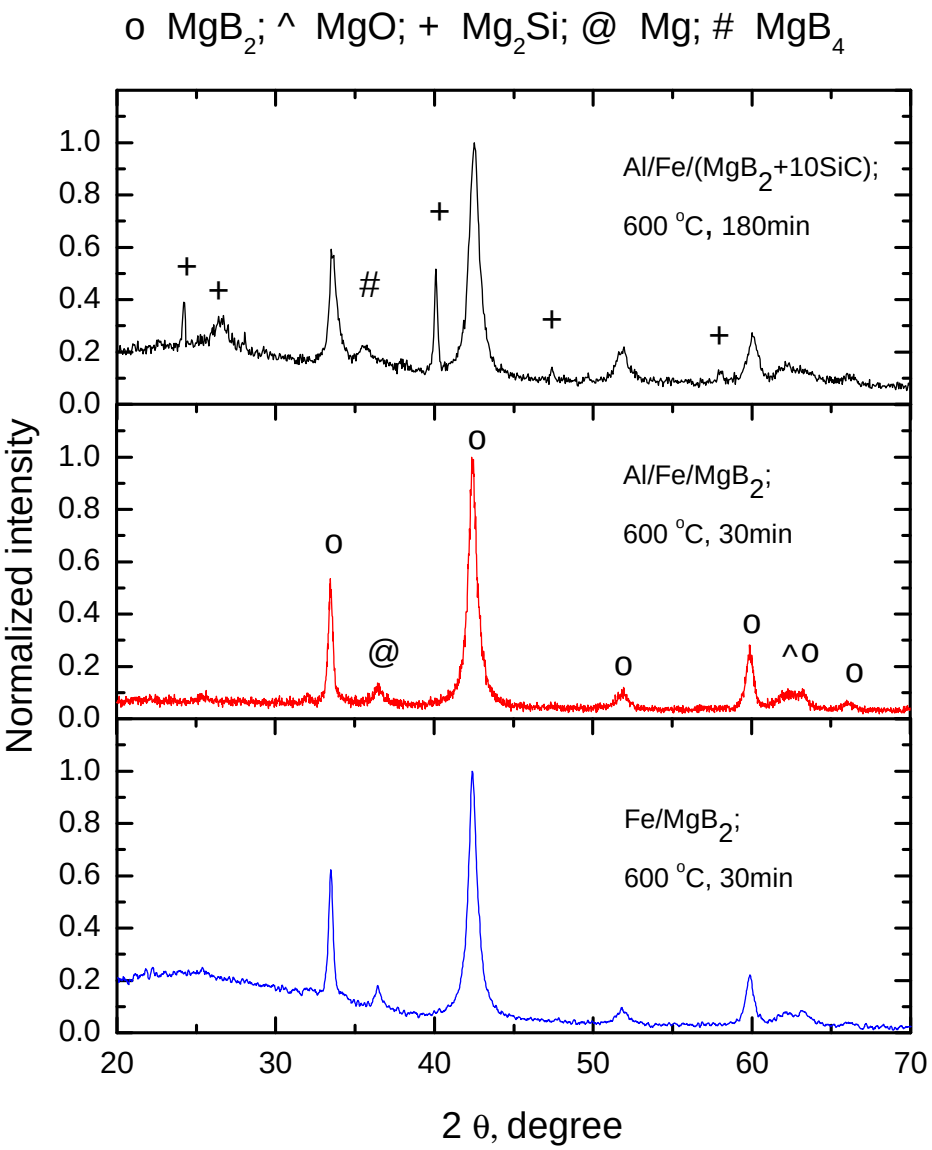

Figure 4.2: *X-ray diffraction patterns for the Fe and Al-Fe clad pure and SiC doped MgB_2 samples prepared at a temperature of 600°C for 30 or 180 min.*

that a sintering temperature of 600°C is sufficient for MgB_2 formation and fabrication of both Fe- and Al/Fe-clad MgB_2 wires.

Fig. 4.3(a) and (b) shows XRD patterns for Al/Fe-clad pure and doped MgB_2 samples sintered at temperatures of up to 630°C for 30 or 180 min. Note, that increasing the sintering temperature or duration results in more complete MgB_2

Table 4.1: *Structural parameters of samples studied.* $\triangle$a *defines changes in the* a *lattice parameter as a result of C substitution into B sites in the* MgB_2 *crystal lattice in SiC-doped* MgB_2*samples.*

Sample, sintering profile (°C × min)	c, Å	a, Å	$\triangle a$, Å	FWHM (101), deg.	Mg_2Si wt.%	T_c, K
Fe/MgB_2, 600×30	3.523	3.077	-	0.6984	-	
$Al/Fe/MgB_2$, 600×30	3.520	3.076	-	0.7073	-	
$Al/Fe/MgB_2$, 600×180	3.526	3.078	-	0.6771	-	35.7
$Al/Fe/MgB_2$, 620×30	3.518	3.077	-	0.6845	-	35.4
$Al/Fe/MgB_2$, 620×90	3.520	3.081	-	0.5416	-	36.0
$Al/Fe/MgB_2$, 630×30	3.524	3.084	-	0.6695	-	36.7
$Al/Fe/SiC\text{-}MgB_2$, 600×180	3.520	3.072	0.006	0.948	45	32.9
$Al/Fe/SiC\text{-}MgB_2$, 620×30	3.520	3.072	0.005	0.8945	39	32.7
$Al/Fe/SiC\text{-}MgB_2$, 620×90	3.523	3.073	0.008	0.8125	49	32.8
$Al/Fe/SiC\text{-}MgB_2$, 630×30	3.529	3.074	0.010	0.7862	42	33.2

formation, as is evident from the vanishing of the Mg peak in samples processed at 620°C for 90 min or 630°C for 30 min. Crystal lattice parameters a and c were calculated from the positions of the (110) and (002) peaks, respectively (Table 4.1). As can be seen, increasing the sintering temperature or sintering time results in increases on the crystal lattice parameters to match the standard value of $a = 3.086\ \mathring{A}$ and c = $3.524\ \mathring{A}$ [25]. This occurs due to improved crystallinity (indicated by smaller FWHM values of the (101) peak, Table 4.1) in MgB_2 compound.

It should be noted that for the SiC-doped MgB_2 sample, the a lattice parameter is reduced due to C substitution into B sites in the MgB_2 crystal lattice (Table 4.1) [103]. This also degrades the MgB_2 crystallinity in SiC-doped samples, as demonstrated by increased FWHM values in these samples. In addition, the large amount of Mg_2Si phase (estimated from the height of the strongest Mg_2Si peak in the XRD patterns) was obtained in SiC-doped MgB_2 samples, as shown in Table 4.1. Note that the amount of Mg_2Si phase increases with increasing sintering temperature or duration (over the studied temperature range).

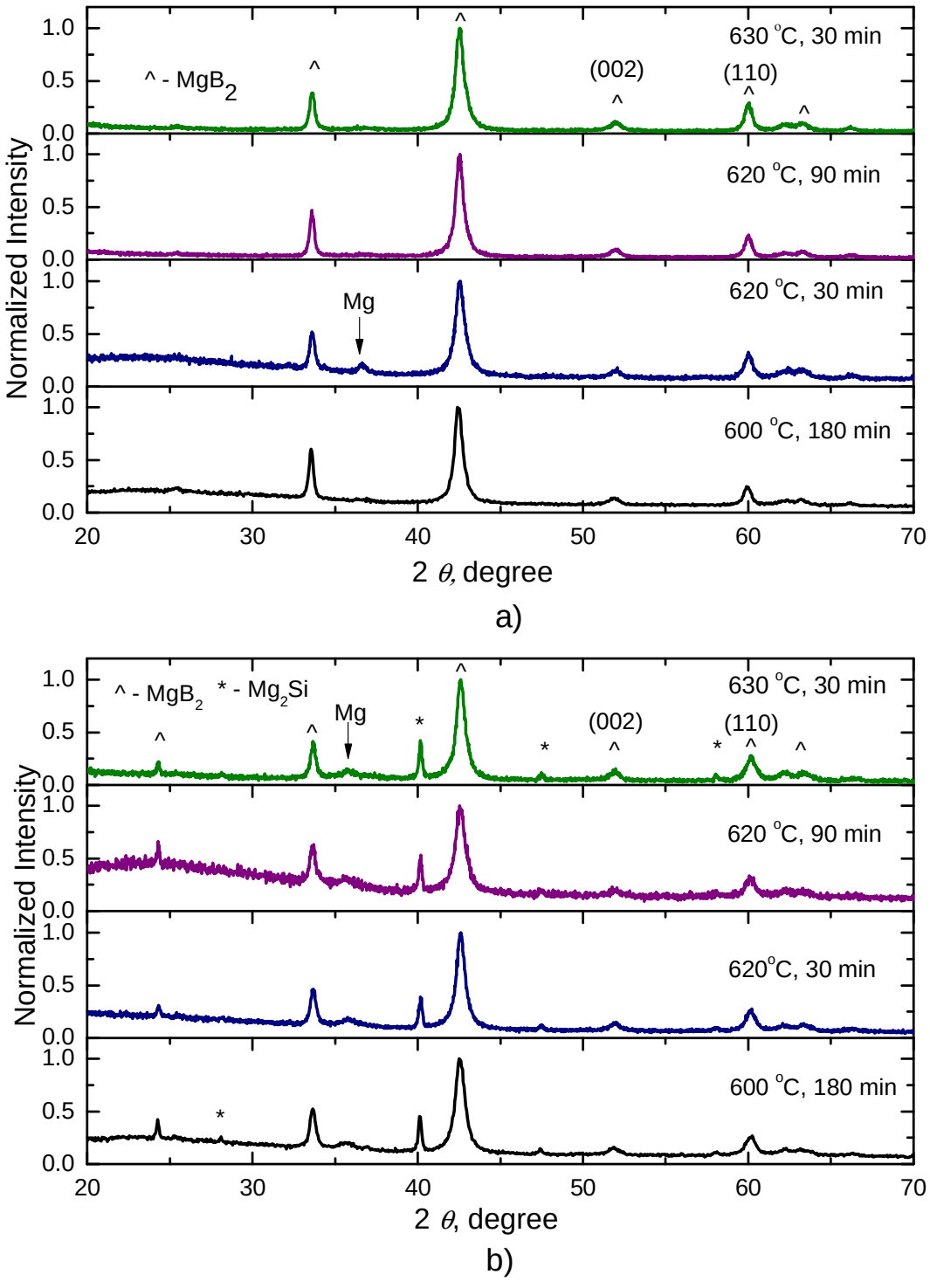

Figure 4.3: *X-ray diffraction patterns for the Al/Fe-clad pure (a) or SiC-doped (b) MgB_2 samples prepared at different sintering temperatures and durations.*

4.4 Superconducting properties

Fig. 4.4 shows the transition temperature, T_c, for the doped and undoped samples as determined by ac susceptibility measurements.

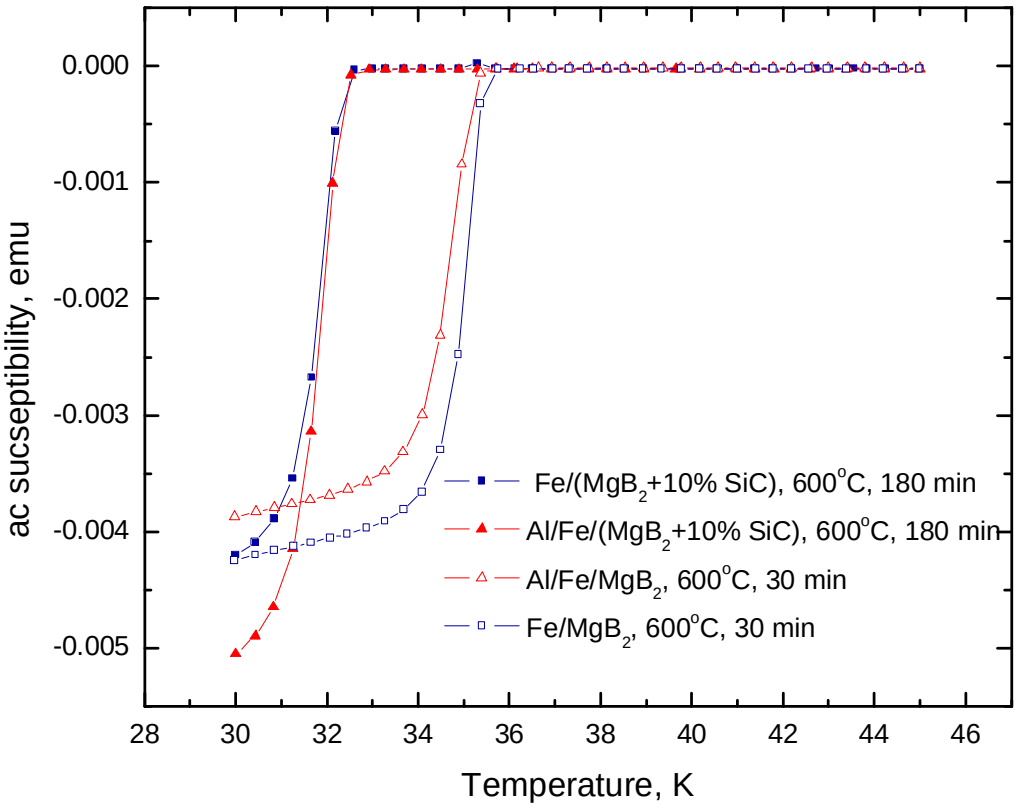

Figure 4.4: *Critical temperature for Fe- and Al/Fe-clad pure and SiC doped MgB_2 samples fabricated at 600°C for 30 or 180 min.*

The T_c obtained for the Fe-clad MgB_2 and Al/Fe-clad MgB_2 samples annealed at 600°C for 30 min is 35.7 K and 35.4 K, respectively. As has been mentioned above, the Al/Fe-clad MgB_2 sample has lower crystallinity, and, therefore, more disorder in the crystal structure [60; 261], which resulted in T_c reduction in this sample.

In contrast, the T_c dropped to 32.5 K for the Fe- and Al/Fe-clad SiC doped MgB_2 annealed at 600°C for 180 min. The reduction of T_c is attributed to the partial substitution of C for B during *in-situ* MgB_2 formation [103].

The T_c values of samples sintered at higher temperatures are presented in the Table 4.1. Generally, higher sintering temperatures result in higher T_c values for both pure and doped MgB_2 samples due to improved crystallinity in these samples.

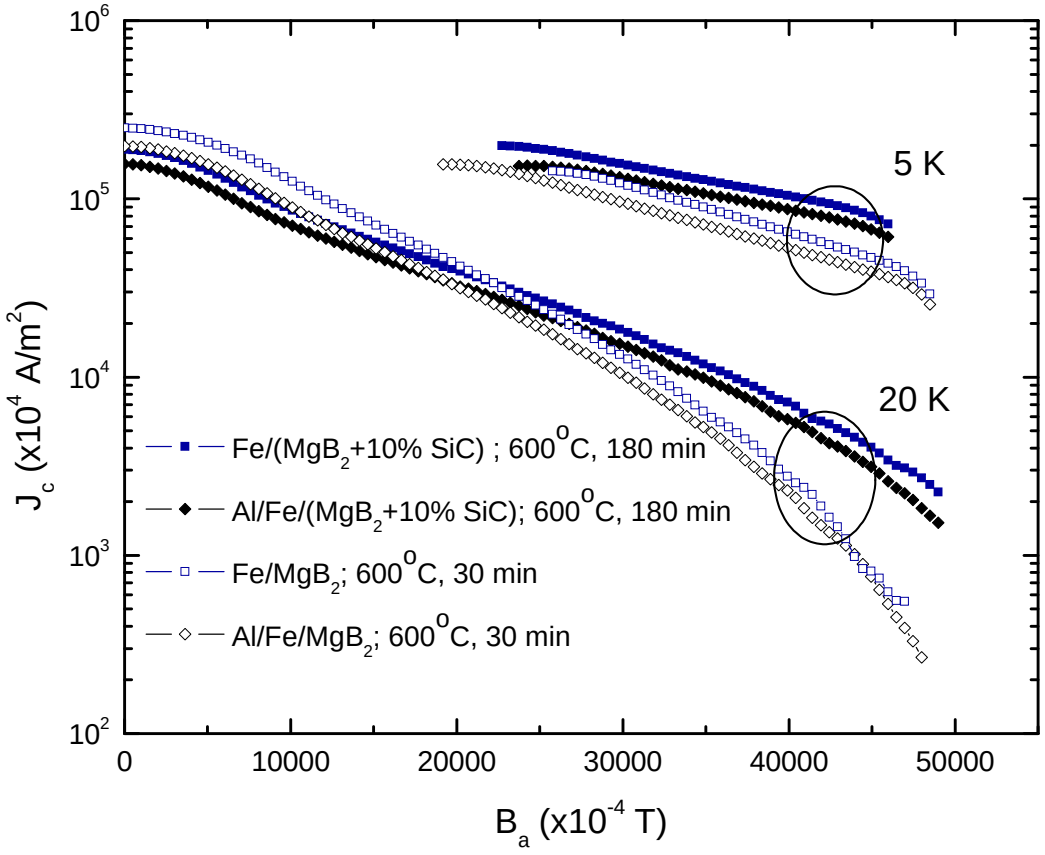

Figure 4.5: *A comparison of $J_c(B_a)$ for the Fe- and Al/Fe-clad pure and SiC doped MgB_2 samples.*

Fig. 4.5 shows the $J_c(B_a)$ curves at 5 and 20 K for the Fe- and Al/Fe-clad pure and SiC-doped MgB_2 sintered at 600°C for 30 or 180 min. These results are consistent with those reported previously on both SiC doped MgB_2 and pure MgB_2 wires [262]. The $J_c(B_a)$ curves of the SiC doped samples show a crossover with the undoped samples at about 2 T and 20 K, confirming that the decrease in $J_c(0T)$ is better compensated by increased pinning above 2 T in SiC doped MgB_2 samples. It should be noted that the $J_c(B_a)$ curves for both the Fe- and Al/Fe-clad

wires show the same trend, although the former is slightly higher than the latter. This is because the Al is relatively softer than Fe, and thus, the compaction of the wire core for Al/Fe sheath is not as high as for Fe sheath. This resulted in relatively lower density of the final core and thus, slightly lower $J_c(B_a)$ for Al/Fe sheathed wire.

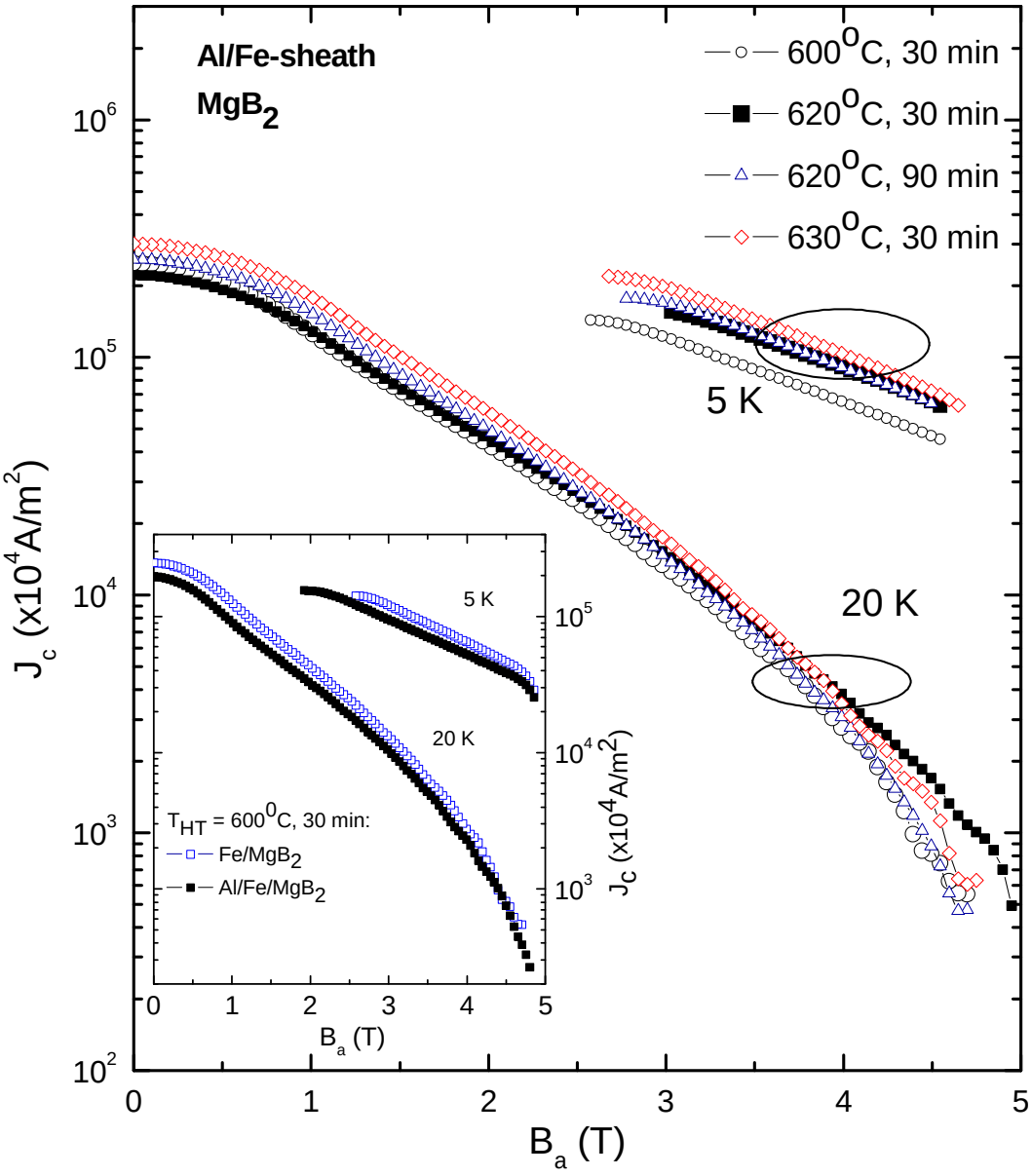

Figure 4.6: *Critical current density for Al/Fe-clad pure MgB_2 samples prepared at different sintering temperatures. The inset compares the Fe and Al/Fe clad samples that were sintered at 600°C for 30 min*

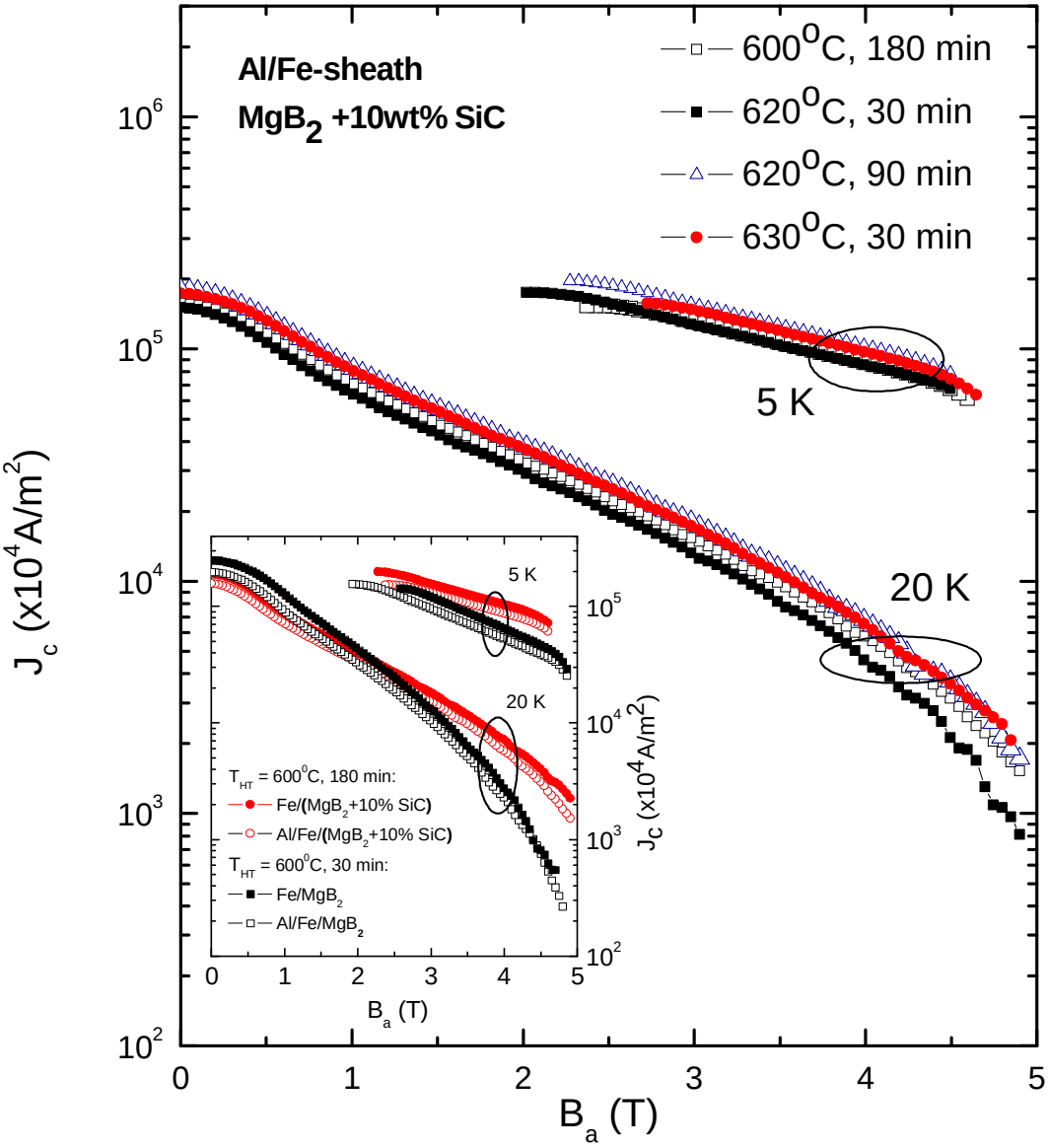

Figure 4.7: *Critical current density for Al/Fe-clad SiC-doped MgB_2 samples prepared at different sintering temperatures. The inset compares selected samples with same sintering temperature and time.*

Figs. 4.6 and 4.7 show the effect of sintering temperature and time on the $J_c(B_a)$ for the samples studied. Although a nearly pure MgB_2 phase is formed by annealing at 600°C for 180 min (Fig. 4.3), the highest $J_c(B_a)$ among pure the MgB_2 samples is achieved by annealing at 630°C for 30 min. This is due to

the observed increase in the critical temperature and improved grain connectivity (or effective, electrically connected area of superconductor, A_{eff}, Chapter 2) in samples fabricated at higher temperature. Note that in the higher field region (B_a >4 T), $J_c(B_a)$ performance is higher for the sample sintered at lower temperature (620°C). This is due to improved pinning on a large amount of grain boundaries, as well as the poor crystallinity which is generally observed in these samples.

In SiC-doped MgB_2 samples, there is a clear correlation between $J_c(B_a)$ performance (Fig. 4.7) and the amount of Mg_2Si phase (Table 4.1). That is, the higher the level of Mg_2Si phase, the higher the $J_c(B_a)$ performance is. The highest $J_c(B_a)$ performances were observed in samples prepared at 630°C for 30 min and 620°C for 90 min, which have 42 wt.% and 49 wt.% Mg_2Si, respectively. In addition, increasing the sintering temperature or time results in substitution of a higher level of C for B in the MgB_2 crystal lattice, which is evident from the large change in the a-lattice parameter ($\triangle a$, Table 4.1). The C substitution and Mg_2Si impurities generate a denser network of defects in SiC doped MgB_2 sample compared to pure MgB_2 samples. These enhance pinning, the upper critical field and thus, in-field critical current density of SiC-doped MgB_2 samples (Chapter 7).

Therefore, the results of this study indicate that sintering of MgB_2 samples at low temperatures (600-630°C) is sufficient for fabrication of MgB_2 wires with adequate superconducting properties.

4.5 SEM investigation of Al/Fe/MgB_2 wires

One of the major concerns relating to the use of aluminium as a stabilizer is whether the Al is compatible with the Fe barrier. Fig. 4.8 shows SEM micrographs for the Al/Fe-clad MgB_2 wires annealed under different conditions.

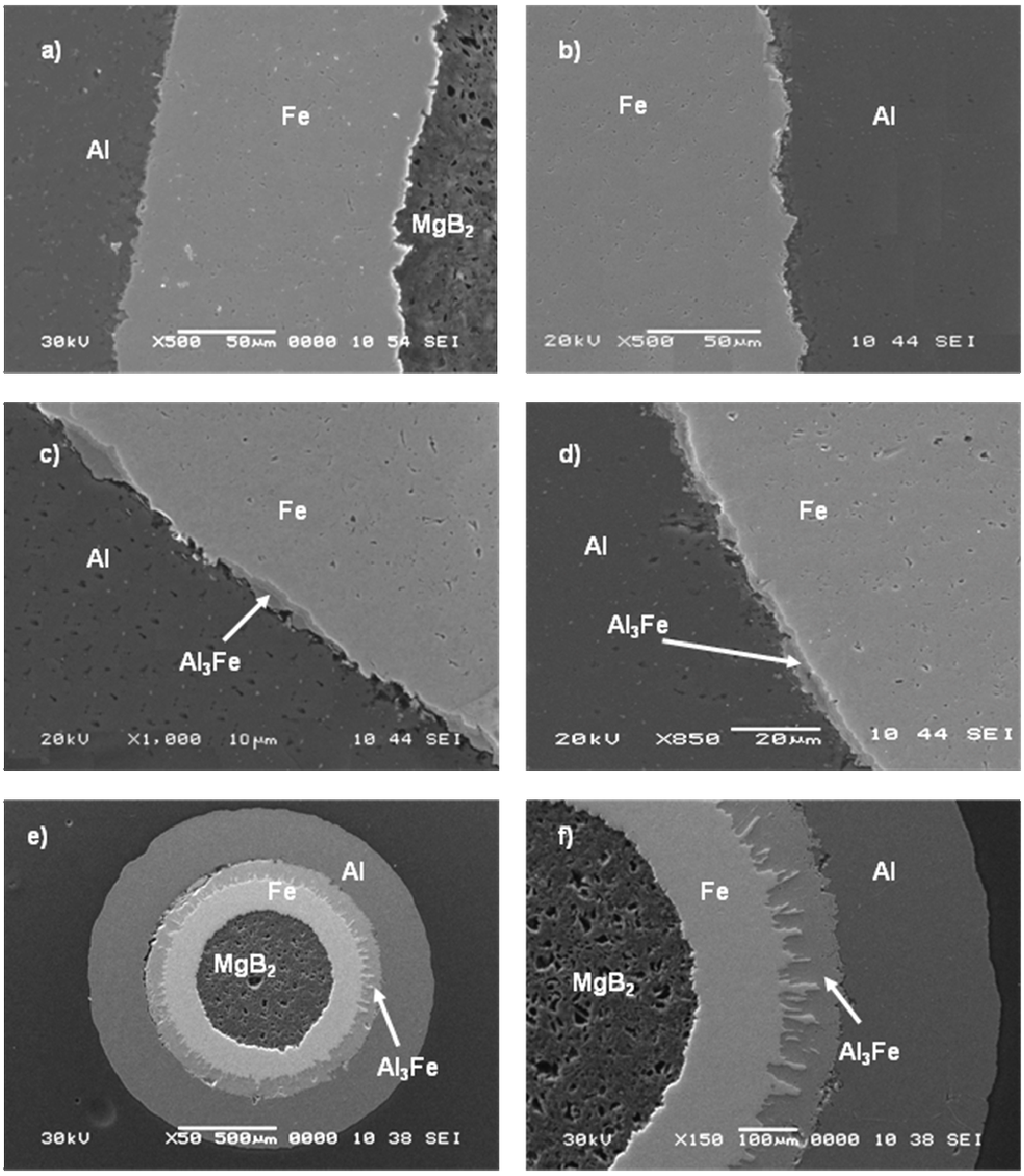

Figure 4.8: *SEM micrographs of the interfaces between the Fe and Al sheath for the single core MgB_2/Fe/Al wire annealed at (a) 600°C for 180 min, (b) 620°C for 30 min, (c) 620°C for 90 min, (d) 640°C for 30 min and ((e)-(f)) 650°C for 30 min.*

It is evident that aluminium and iron remain chemically compatible at an annealing temperature of 600°C for 180 min and 620°C for 30 min (Fig. 4.8(a, b)). The Al/Fe interface remains clean and sharp with no evidence of reaction between Fe and Al under these processing conditions.

The alloy phase of Al_3Fe, as defined by EDS study, starts to form as a thin

layer (about 5 μm) at an annealing temperature of 620°C for 90 min, but remains small up to an annealing temperature of 640°C for 30 min. The Al_3Fe phase grows rapidly at an annealing temperature of 650°C for 30 min, resulting in a 100 μm thick interface layer.

At higher sintering temperature (650°C) there is a crack between Al and Fe, which is likely to be the result of the different thermal expansion coefficients for Al and Fe. Thus, cracks may form during cooling of samples to room temperature.

The thermal conductivity of Fe-Al alloy is lower (0.27 W/cmK) than the thermal conductivity of Fe (0.8 W/cm K) and Al (2.37 W/cm K) [265] and thus, is not desirable for stabilization issues. However, the thin alloy layer may improve the contact between the Al and Fe materials.The formation of Al alloy may set the upper limit of the annealing temperature for processing Al/Fe-sheathed MgB_2 wires, as the Al diffusion into the Fe layer may reach the MgB_2 core and cause a reaction between Al and MgB_2. However, the results observed demonstrate that there is a reasonable annealing-temperature range from 600 to 630°C, where the formation of Al_3Fe alloy would not cause a detrimental effect.

4.6 Summary

In summary, it has been demonstrated that Al/Fe-clad pure and SiC-doped MgB_2 superconductors can be formed by the PIT method and sintering of the corresponding wires at a temperature of 600-630°C. The formation of MgB_2 phase is completed for 30 or 180 min in pure or SiC-doped MgB_2 wires, respectively. Processing of soft Al metal slightly deteriorates the density of MgB_2 core resulting in poor crystallinity and thus degraded T_c values of final Al-stabilized Fe-clad MgB_2 wires. However, higher temperature or longer duration of heat-treatment procedure leads to higher critical temperature of final MgB_2 compound. The critical

current density and flux pinning behavior of Al/Fe-clad MgB_2 wires are found to be comparable with those of Fe-sheathed MgB_2 wires. The Al and Fe sheath materials are compatible at temperature of 600°C, while some reaction with formation of Al_3Fe alloy starts at temperatures above 620°C for longer sintering time (90 min). This interfacial layer is not uniform and has undesirable low thermal conductivity coefficient, but could assure good mechanical contact between Al and Fe-barrier of the final Al/Fe-clad MgB_2 wire.

The feasibility of fabrication of Al-stabilized MgB_2 wires has been demonstrated in this Chapter. This is paving the way for possible use of the lighter and cheaper Al/MgB_2 superconductors in airborne, aerospace, and other applications where weight is important. High-purity Al stabilizer may require extra strengthening for some applications, but in this case it will be possible to add an outer sheath of an Al alloy, such as AA5083 or AA6082, either in the pure-or internally-oxidized state.

Chapter 5

New method for the fabrication of Al-Stabilized MgB_2/Fe superconductor

5.1 Introduction

As explained in previous Chapter, the replacement of Cu by Al in cryogenic and superconducting applications is accompanied by several important advantages: (i) relatively low structural mass, (ii) greater thermal conductivity to the cryogen bath or cryocooler; (iii) more efficient stabilization. The feasibility for fabrication of Al-stabilized MgB_2 wire with Fe as a barrier using the solid-state diffusion approach has also been demonstrated. Although this method is shown to be practical, this has undesirable limitations. These are reduced superconducting MgB_2 core density and possible degradation of mechanical (and electrical) contact between Fe and Al layers, which is not desirable for long length wire fabrication. In addition, this method is restricted by relatively low ($\leq 630°C$) sintering temperatures, while higher sintering temperatures would increase critical temperature of the final Al-

stabilized MgB_2 conductors.

To overcome these problems and enhance superconducting properties of Al-stabilized MgB_2 wires, we have employed the hot aluminizing technique [275]. The present technique allows us to apply Al stabilizer to a completely fabricated and optimized Fe/MgB_2 composite. In this case, Fe plays the role of a barrier preventing diffusion of Al into MgB_2. In addition, the high toughness of Fe enables us to produce a reasonably high-density MgB_2 superconducting core. Furthermore, the hot aluminizing technique can be modified to achieve the simultaneous process of fabrication of Al stabilized wires/coils and *in-situ* MgB_2 formation because the processing temperature of *in-situ* MgB_2 formation (650^{o}C) is similar to the melting temperature of Al (660°C) [229]. This process is very attractive for the construction of MgB_2 superconducting magnets. In this Chapter, we report the first results on simultaneous combined fabrication of *in-situ* Fe/MgB_2 wire and coating of this Fe/MgB_2 wire with an Al-layer for stabilization purposes.

5.2 Experimental procedure

Fe-sheathed MgB_2 wire was fabricated using the *in-situ* process and the standard PIT method. An Fe tube with an outer diameter (OD) of 10 mm and a wall thickness of 1 mm was filled with a mixture of pure Mg (99%) and amorphous B (99%) with the stoichiometry of MgB_2. The composite was drawn to an OD of 1.4 mm. Several short samples were sintered in a tube furnace at 750°C for 30 min in flowing high purity argon to prevent oxidation. The resultant Fe/MgB_2 with no Al is referred to below as the reference sample. After completing the heat treatment process, the surface of the reacted Fe/MgB_2 wires was plated with Al using the hot aluminizing technique. Short samples of reacted Fe/MgB_2 wire were immersed for 3 min in a molten Al bath kept at a temperature of 750°C under flowing high

purity argon. After coating, the sample had an OD of 1.32 ± 0.05 mm. These samples are denoted as the "reacted" Al/Fe/MgB_2 in the text. To investigate the possibility of a simultaneous process for Al plating and *in-situ* MgB_2 formation, short samples of unreacted Fe/MgB_2 wire were immersed for 5 to 30 min in a molten Al bath kept at a temperature of 670 or 770°C under flowing high purity argon. These samples are denoted as "green" Al/Fe/MgB_2 in the text.

The phase investigation was performed with the help of an x-ray diffractometer with CuKα radiation. The magnetization loops for the Fe and Al/Fe sheathed MgB_2 wires were measured at 10 and 20 K using a Physical Properties Measurement System (PPMS, Quantum Design) with a magnetic field applied perpendicular to the wire long axis. The magnetic J_c was derived using Eq.(3.3). The transport J_c was measured with the four-probe method using a pulsed current source. This technique is described in detail in Ref. [276]. The voltage contacts were attached directly onto the Al surface with Sn-9%Zn solder.

5.3 Results and discussion

Fig. 5.1 shows XRD patterns for the core of the "green" Al/Fe/MgB_2 samples after immersing unreacted Fe/MgB_2 wire in an Al bath kept at a temperature of 670°C for 5, 15 and 30 min and at a temperature of 770°C for 5 and 10 min. As can be seen, at lower temperature (670°C) the reaction between Mg and B could be achieved after 30 min. Only a small peak of unreacted magnesium could be found. For the higher temperature Al bath (770°C), the *in-situ* reaction of MgB_2 formation was fully completed in 10 min. A small peak of MgO could be found in all the samples studied. It should be noted that there is no evidence of any reaction between Al and MgB_2 after the aluminizing routine, indicating the good properties of Fe as a barrier.

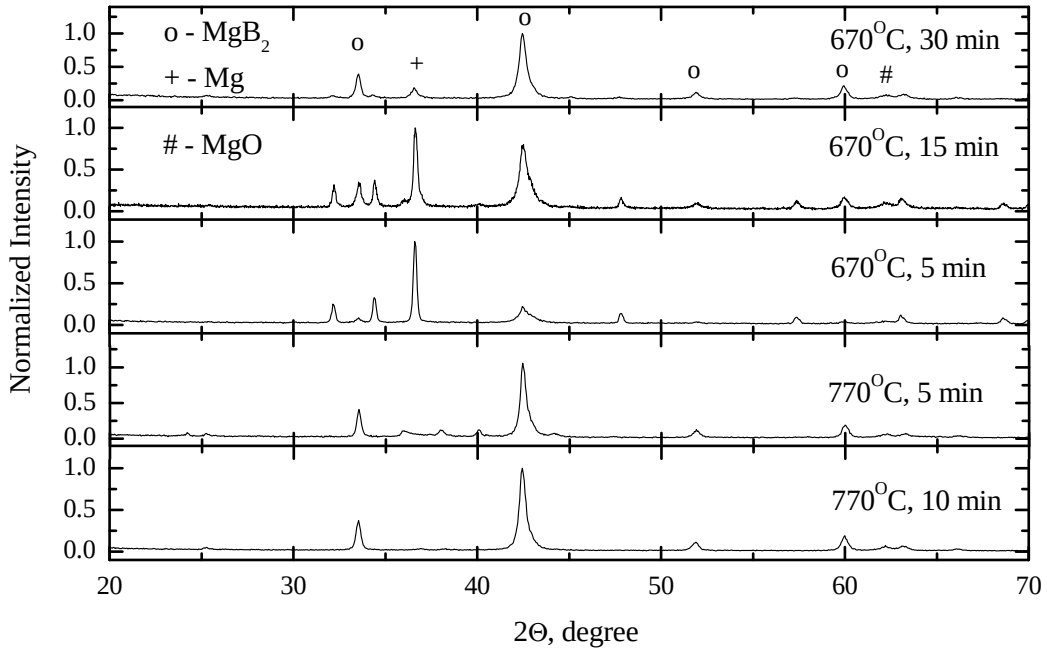

Figure 5.1: *X-ray diffraction patterns for the "green" MgB_2/Fe wire samples immersed in an Al bath at 670°C for 5, 15, and 30 min and at 770°C for 5 and 10 min.*

SEM investigation of the Al/Fe/MgB_2 wire cross-section showed that there was a continuous coating of the Fe sheathed MgB_2 wire with an $\sim$ 10 μm thin Al layer (Figs. 5.2 and 5.3). A diffusion layer of Al_3Fe alloy had a thickness of about 9 μm at the Al/Fe interface. This diffusion alloy layer indicates good connectivity between the two materials (Fe and Al). It is worth noting that as a result of the hot aluminizing procedure, the thickness of the Fe barrier was slightly reduced compared to the Fe/MgB_2 sample due to the reaction between Fe and Al. Increasing the Al bath temperature or time of exposure in hot Al resulted in a further reduction of the Fe barrier thickness (Fig. 5.3). This is beneficial for wire stabilization. As was discussed above, Fe has undesirably low thermal conductivity. On the other hand, the Fe barrier should prevent the diffusion of Al into the MgB_2 core, which may cause severe damage to the superconductor. The formation of the diffusion Al_3Fe alloy may set limits to the desirable Fe barrier thickness and sintering parameters for the hot aluminizing process.

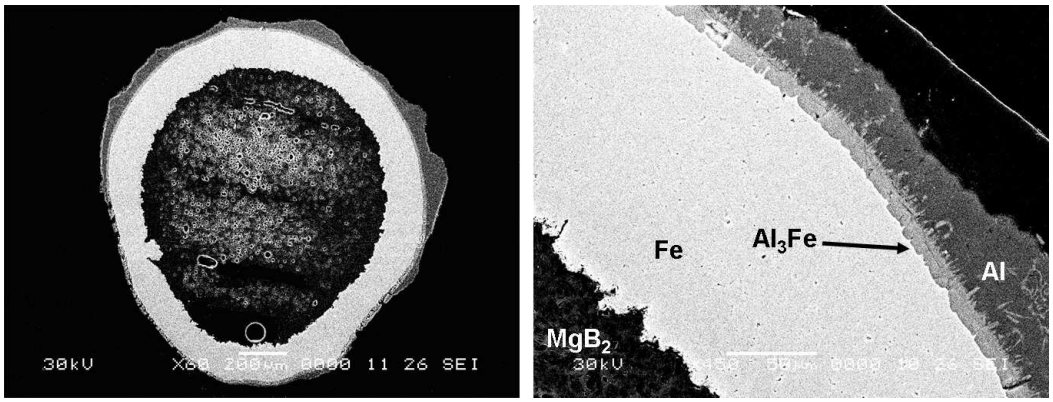

Figure 5.2: *SEM images of the "reacted" Al/Fe/MgB_2.*

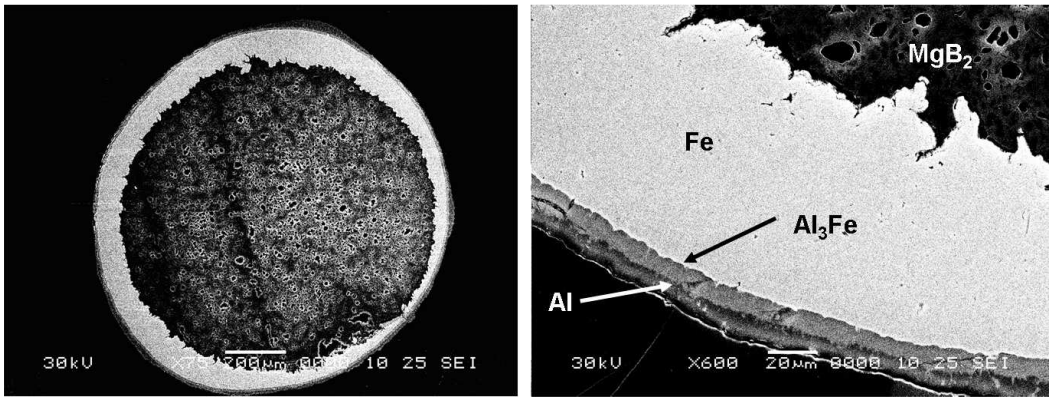

Figure 5.3: *SEM images of the "green" Fe/MgB_2 wire sample immersed for 10 min in an Al bath kept at 770°C.*

Fig. 5.4 shows the magnetic J_c values for the reference Fe/MgB_2, as well as for the "reacted" and "green" Al/Fe/MgB_2 wires with the magnetic field applied perpendicular to the wire long axis. For the MgB_2 with only the Fe sheath and the "reacted" Al/Fe/MgB_2 wire samples, magnetic J_c values are similar over the entire range of temperatures and fields measured, although they are slightly higher for the former than the latter. It is worth noting that the Fe-sheathed MgB_2 wire exhibited more strongly pronounced flux-jump behavior in the low field region (0−2 T) compared to the Al-stabilized MgB_2 wire at 10 K. On the other hand, the similar magnetic $J_c(B_a)$ performance indicates that the hot aluminizing process did not affect the properties of the MgB_2 superconducting core. This is a significant

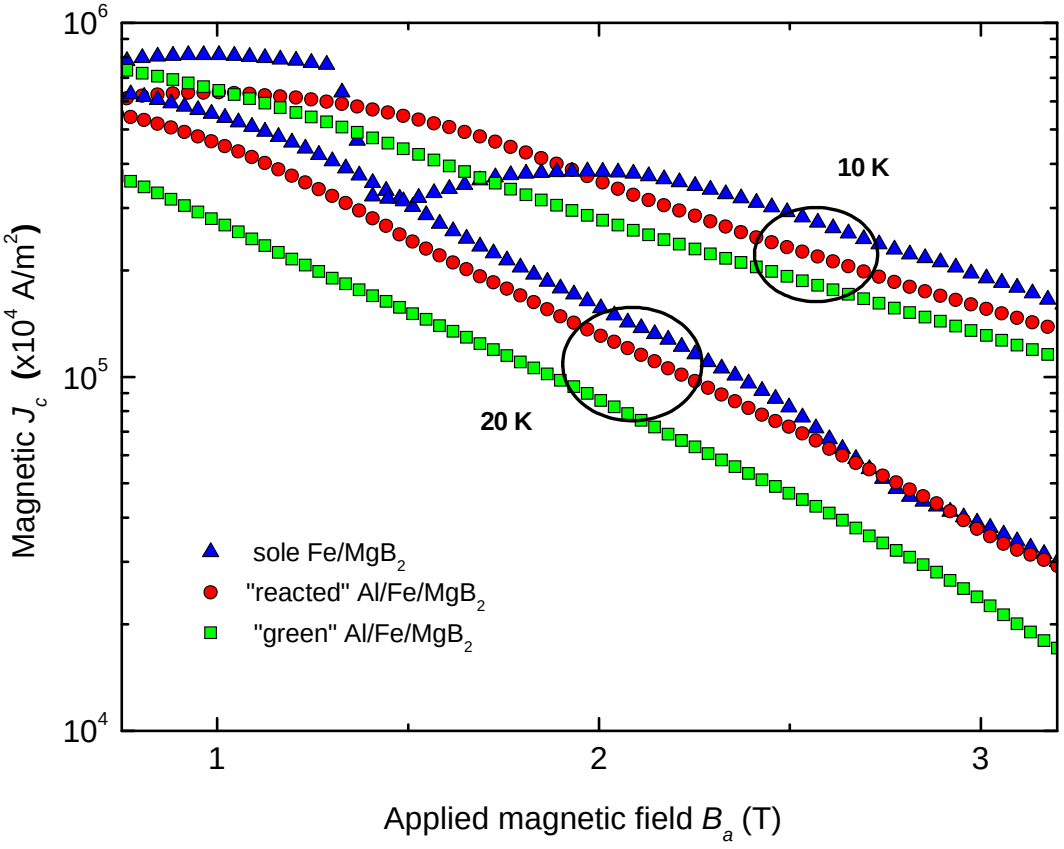

Figure 5.4: *Magnetic* $J_c(B_a)$ *curves at 10 K and 20 K for the reference Fe/MgB*$_2$*, and for the "reacted" and "green" Al/Fe/MgB*$_2$ *wires. The "green" Al/Fe/MgB*$_2$ *wire was reacted in an molten Al bath kept at 670°C for 30 min.*

advantage of the aluminizing process, which turns out to be a non-destructive approach to thermomagnetic stabilization.

As can be seen from Fig. 5.4, Al-coating of the Fe-sheathed MgB_2 wires results in better thermomagnetic stabilization at 10 K. Further improvement of stabilization at temperatures below 10 K can be achieved by increasing the Al to superconductor ratio, decreasing the thickness of the Fe barrier, and reducing the Fe/MgB_2 wire diameter.

It should be noted that the "green" $Al/Fe/MgB_2$ wire showed a similar trend in the magnetic $J_c(B_a)$ curve to the reference Fe/MgB_2 and the "reacted" $Al/Fe/MgB_2$

wire, although the $J_c(B_a)$ values are slightly lower (Fig. 5.4). J_c values of 3.6×10^8 and 2.3×10^8 A/m^2 were reached at 20 K and 3 T for the "reacted" and "green" Al/Fe/MgB_2 wires, respectively. These results are in agreement with those for Fe/MgB_2 wires reported by other groups [204; 207].

The transport $J_c(B_a)$ values of the reference Fe/MgB_2, and the "reacted" and "green" Al/Fe/MgB_2 wires are presented in Fig. 5.5. The $J_c(B_a)$ curves nearly coincide for Fe-sheathed MgB_2 and "reacted" Al/Fe-sheathed MgB_2 wires at $B_a > 4$ T at 10 K, as well as at $B_a > 3.3$ T at 20 K. The transport J_c values of "reacted" Al/Fe/MgB_2 wire are in agreement with previous results on Fe/MgB_2 [268; 269; 277], included for comparison in Fig. 5.5. As can be seen, at 20 K and 3 T the J_c values reached 3.7×10^8, 3.6×10^8, and 2.2×10^8 A/m^2 for sole Fe/MgB_2, and the "reacted" and for "green" Al/Fe/MgB_2 wires, respectively.

It is expected that the application of the hot aluminizing technique can be further improved by optimization of the melt-processing temperature and dipping time, Fe sheath thickness, and other parameters. Moreover, the aluminizing technique, which is demonstrated in this work for Fe/MgB_2 wires, can be further extended to fabrication of Al-stabilized Fe/MgB_2 coils. We expect that a coil with a wound Fe-sheathed MgB_2 "green" wire, can be heated up to the MgB_2 reaction temperature. While the reaction is complete or in process, the spool can be immersed in a molten Al bath and cooled down. It is obvious that this dual process of *in-situ* MgB_2 formation and coating of the Fe/MgB_2 wire/coil by Al will simplify the coil fabrication and markedly improve the cost feasibility of the MgB_2 conductor applications. In addition, Al/Fe/MgB_2 conductors mainly made up of low-density components will be advantageous for airborne, aerospace, and other applications where weight is an important issue.

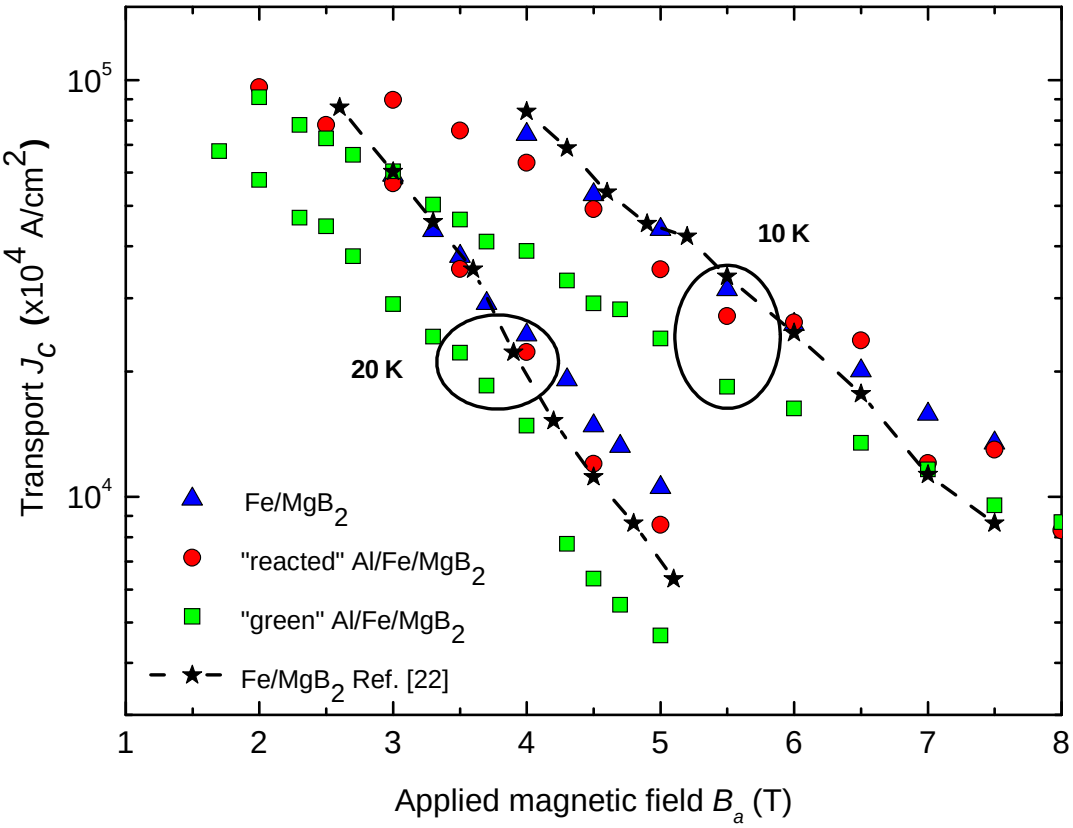

Figure 5.5: *Transport* $J_c(B_a)$ *of sole Fe/MgB*$_2$*, and the "reacted" and "green" Al/Fe-MgB*$_2$ *wires. The "green" Al/Fe/MgB*$_2$ *wire was reacted in an molten Al bath kept at 670°C for 30 min.*

5.4 Summary

In summary, we have demonstrated a new approach for simultaneous (i) fabrication of *in-situ* Fe/MgB_2 wires and (ii) coating with the Al stabilizer. The transport critical current density of thus-fabricated $Al/Fe/MgB_2$ wire achieved the level of 2.2×10^8 A/m^2 at 20 K and 3.5 T, which is only slightly lower than $J_c = 3.7\times10^8$ A/m^2 of the reference Fe/MgB_2 sample. The magnetic measurements show that the Al layer stabilizes the Fe/MgB_2 wires in the lower field region over the measured temperature range. This method can be easily extended to the production of coils, resulting in reduction of the fabrication time and cost of MgB_2

conductor products due to eliminating one processing stage. The light weight of most elements in the Al/Fe/MgB_2 system pave the way for possible use of this superconductor in various applications where weight is a crucial parameter.

Chapter 6

Effect of Fe-based doping on superconducting properties of MgB_2 conductors

6.1 Introduction

Recently, there has been considerable interest in improvement of flux pinning in MgB_2 by the use of magnetic nanoparticle additions. This was motivated by theoretical predictions of current carrying ability enhancement in ferromagnet/superconductor hybrids [278; 279]. These investigations were performed on thin film samples, however, this attracted the attention of researchers working on powdered MgB_2.

Several attempts were undertaken in order to fabricate this type of hybrid with enhanced functionalities for magnesium diboride superconductor. Some publications report enhancement of in-field $J_c(B_a)$ and B_{irr} upon doping MgB_2 with magnetic nanoparticles: Fe_2O_3 [163], Ho_2O_3 [280], Fe_3O_4 [281], Co_3O_4 [282]. However, there are some observations of detrimental influence of magnetic Fe nanoparticles

on $J_c(B_a)$ in MgB_2 [262; 283].

In this Chapter, we aim to clarify the effect of Fe and Fe-based doping on the electromagnetic performance of MgB_2 wires. For this purpose, Fe-based nanoparticles (Fe_2B and SiO_2 coated Fe_2B) were synthesized (in University of Zagreb) and structurally analyzed in a frame of collaborating work between our group and group from University of Zagreb [284]. In this thesis, structural and magnetic properties of home synthesized Fe_2B and SiO_2 coated Fe_2B particles are used for comparison with properties of pure nano-Fe particles. Furthermore, a comparative study of the effects caused by nano Fe and Fe-based materials on MgB_2 samples was conducted. The idea behind this type of material (Fe_2B and Fe_2B/SiO_2) is to reduce the effect of doping on the stoichiometric Mg/B ratio, which occurs for pure Fe doping to MgB_2 due to F_2B impurity formation [262; 283]. The SiO_2 coated Fe_2B particles were expected to eliminate the problems with clustering of magnetic particles, thus enabling fabrication of more homogeneous Fe-clad MgB_2 wires. An SiO_2 layer may also work as an insulator between ferromagnetic and superconducting phases. On the other hand, these particles could introduce multiple/diverse pinning centers resulting in increased flux pinning and critical current density. Furthermore, particles larger than the usual particle size (80 nm vs. usual 25 nm) were selected in order to investigate recent suggestions that magnetic pinning force increases with increasing particle size [163]. All these issues will be explored in this Chapter.

6.2 Samples and experimental techniques

Nanoparticles of iron boride (Fe_2B) and SiO_2 coated Fe_2B (called Fe_2B/SiO_2 later in the text) were synthesized, using reduction of metal ions by sodium borohydride as described in Ref. [284].

Pure and doped Fe-sheathed MgB_2 wires were prepared by the *in-situ* powder-in tube-method. For preparation of doped wires, as synthesized Fe_2B and Fe_2B/SiO_2 particles were added at the levels of 3 and 7.5 wt% to the Mg + 2B mixture. Mixed powders were packed into Fe-tubes with 10 and 6.5 mm outer and inner diameter, respectively. The tubes were drawn to wires 1.41 mm in diameter. Finally, the reaction heat treatment was performed at 750°C for 60 min in pure argon atmosphere.

Pure and Fe doped MgB_2 samples were also prepared *in-situ* in the form of bulks. Nano-Fe powder with a particle size of 25 nm was added to Mg + 2B mixture at the levels of 1 and 5 wt%. Pellets were sealed in Fe tubes and annealed at temperature of 800°C for 60 min in pure argon atmosphere to avoid oxidation.

As-synthesized Fe_2B and Fe_2B/SiO_2 dopants, as well as nano-Fe particles, and pure and Fe-based doped MgB_2 samples were examined by X-ray powder diffraction. The nanostructures of the synthesized Fe_2B and Fe_2B/SiO_2 particles were studied using Scanning Electron Microscopy (SEM).

Magnetization measurements of dopant particles were performed in a PPMS (Quantum Design) magnetometer at magnetic fields that varied from -5 T to +5 T. The Fe, Fe_2B and Fe_2B/SiO_2 powder samples for magnetic measurements were dispersed and fixed in paraffin in a measuring ampoule to avoid rotation of particles in changing magnetic fields. The magnetization of pure and Fe-based doped MgB_2 samples was measured at temperatures of 5 and 20 K in magnetic fields up to 9 T. Magnetic critical current density values were determined from Eqs. (3.1) and (3.3) for bulk and wire samples, respectively. The irreversibility field, B_{irr}, was defined as a field at which critical current density reaches the value of 10^6 A/m^2.

6.3 Characterization of Fe, Fe_2B, and Fe_2B/SiO_2 doping materials

In order to clarify the effects of Fe-based dopants on performance of MgB_2 superconductor, we first performed systematic structural and magnetic characterization of the synthesized Fe_2B and Fe_2B/SiO_2, as well as the pure Fe nano-particles.

6.3.1 Structural analysis

The XRD pattern for Fe particles in Fig. 6.1 shows two peaks at 2θ of 44.7° and 65°, corresponding to elemental Fe and indicating that Fe powder is crystalline. There are several broad peaks related to (amorphous) Fe_3O_4 impurities in the starting nano-Fe powder. These are due to the fact that the surface of the nano-sized Fe is highly reactive and becomes easily oxidized when exposed to the air [262].

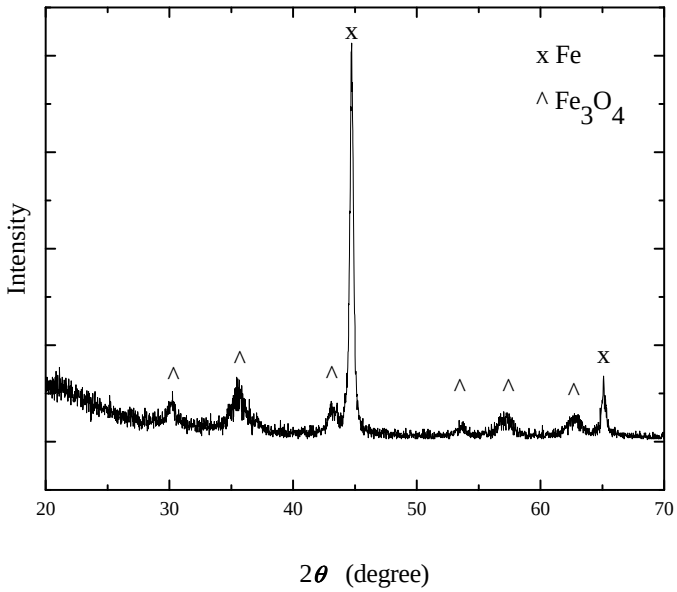

Figure 6.1: *X-ray diffraction pattern for nano-Fe powder (as received from the supplier).*

The XRD pattern [284] for synthesized Fe_2B material in Fig. 6.2 consists of

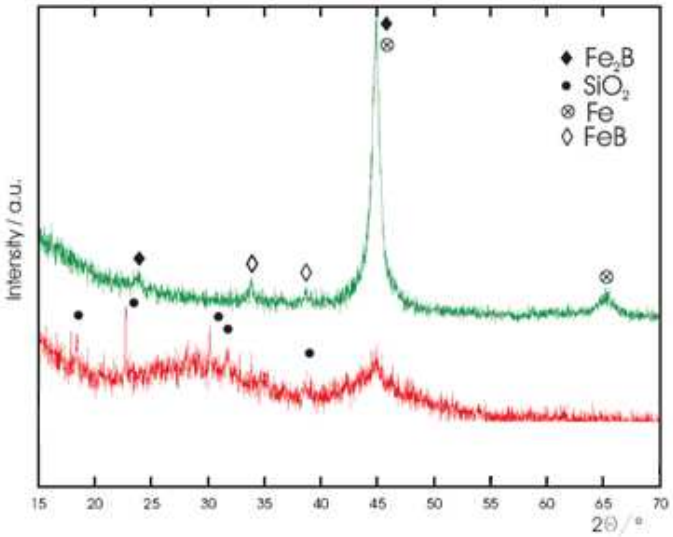

Figure 6.2: *X-ray diffraction patterns for dopant materials: (a) home-made Fe_2B (green), Fe_2B/SiO_2 (red) particles [284].*

three phases: Fe (at 2θ of 44.7° and 65°), FeB (at 2θ of 34.8° and 40°) and Fe_2B (at 2θ of 24.7° and 45.1°) particles. The intensity of the peaks is correlated with the amount of phase presented in the material, with (crystalline) Fe_2B phase being dominant. The broad width of the Fe diffraction line suggests that the size of Fe particles is small ($\leq$ 10 nm).

In the XRD pattern of Fe_2B/SiO_2 material in Fig. 6.2 [284], there are two broad maxima corresponding to Fe_2B (at 2θ of about 45.1°) and SiO_2 (at 2θ of about 28°) phases. The broadness of these peaks indicates the amorphous state of the corresponding phases. Several sharp peaks were also detected, and they indicate the presence of crystalline SiO_2 phase in the Fe_2B/SiO_2 dopant.

6.3.2 SEM investigation of dopants

Typical SEM images of the synthesized Fe_2B and SiO_2 coated Fe_2B particles are presented in Fig. 6.3(a) and 6.3(b) [284], respectively.

As can be seen, Fe_2B particles tend to group in chain-like structures. This is due to the magnetic interaction of these particles. In contrast, the coated particles (Fe_2B/SiO_2) are grouped in stacks, indicating weak non-directional surface

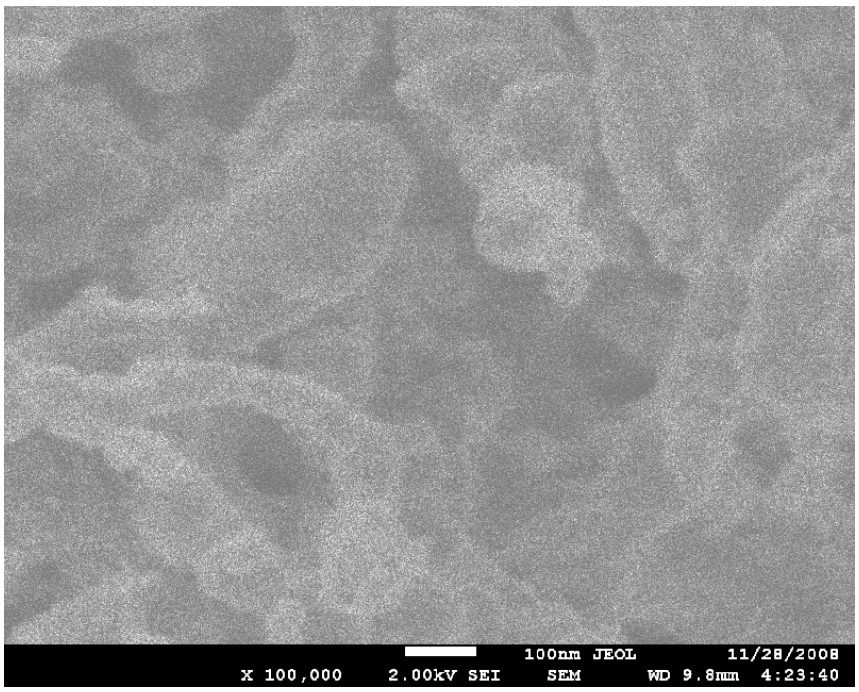

(a)

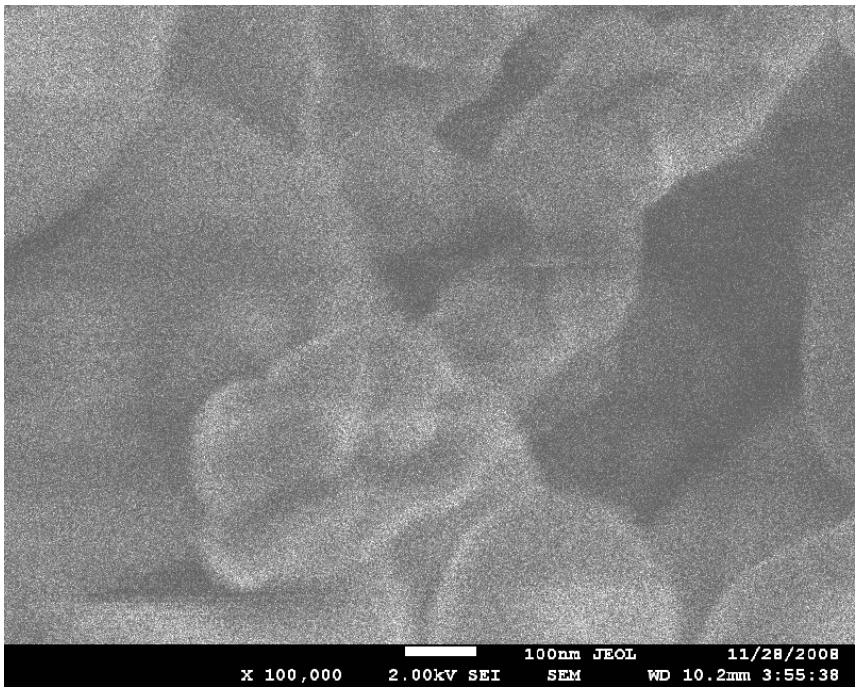

(b)

Figure 6.3: *SEM images of synthesized Fe_2B (a) and SiO_2 coated Fe_2B (b) particles [284].*

interactions.

Several SEM images were used to determine the size distribution of the Fe_2B and Fe_2B/SiO_2 particles seen in the pictures. The size distributions of both types of particles were quite broad, with a mean particle diameter of 84 nm for Fe_2B (Fig. 6.4(a)) and 177 nm for Fe_2B/SiO_2 particles (Fig. 6.4(b)) [284].

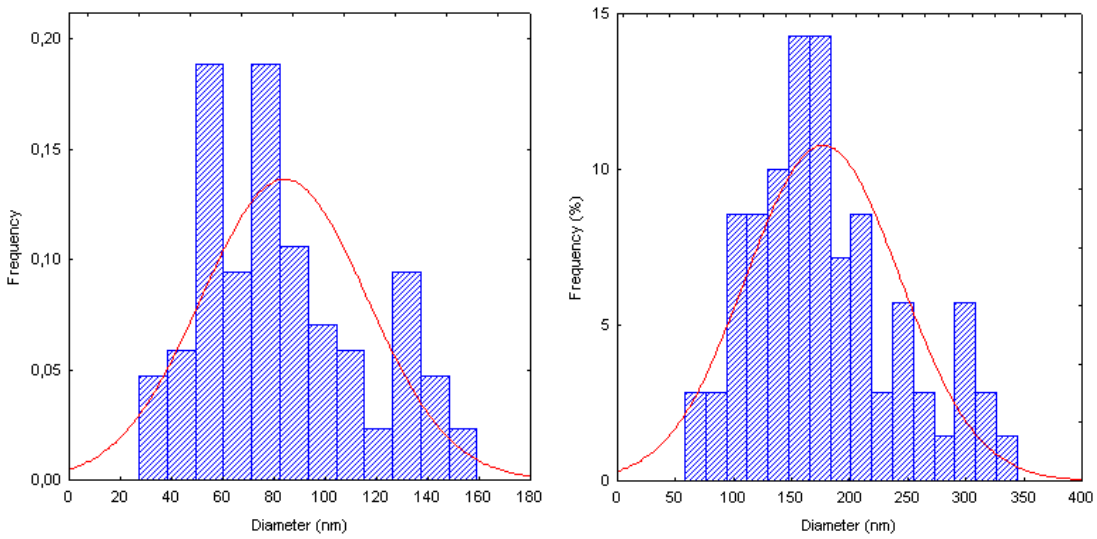

(a) (b)

Figure 6.4: *Size distributions of Fe_2B (a) and SiO_2 coated Fe_2B (b) particles [284].*

6.3.3 Magnetic moment of doping materials

Magnetic hysteresis loops at magnetic fields up to 5 T collected for the investigated Fe-based dopants are presented in Fig. 6.5. The hysteresis loops for Fe_2B and Fe_2B/SiO_2 materials [284] have curved shapes, pointing to a blocked superparamagnetic ensemble of particles, similar to ones observed in the literature [285; 286].

The saturation magnetization, M_s, at 5 K is about 210, 103, and 26 Am^2/kg for the investigated nano-Fe, Fe_2B, and Fe_2B/SiO_2 particles, respectively. For nanocrystalline Fe_2B particles, an M_s value of 80 Am^2/kg is reported in the litera-

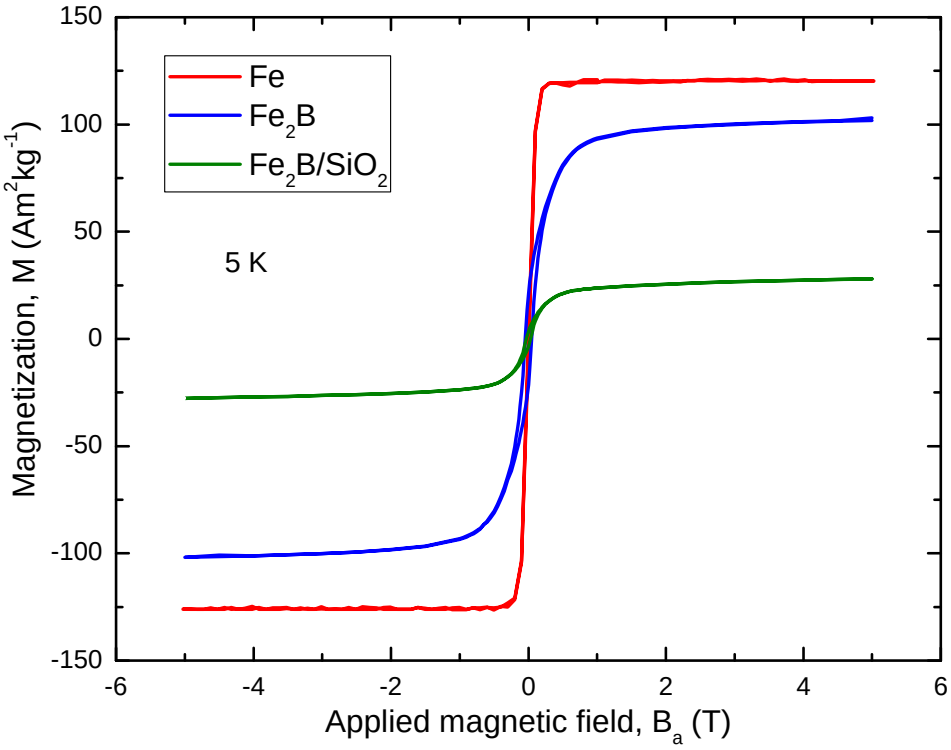

Figure 6.5: *Magnetic hysteresis loops for Fe, as well as Fe_2B and Fe_2B/SiO_2 [284] dopants studied measured at temperature of 5 K.*

ture [287]. It is proposed that the higher M_s value of synthesized Fe_2B particles is due to the presence of Fe phase, as was detected in the XRD patterns. Nanocrystalline Fe has a saturation magnetization of about 210 Am^2/kg (Fig. 6.5 and Ref. [288]). If we assume that Fe and Fe_2B are the only significant magnetic components and that the mass of any others is negligible, we can estimate that the mass content of Fe and Fe_2B is 17 % and 83 % [284], respectively.

For Fe_2B/SiO_2 particles, the saturation magnetization is reduced to 26 Am^2/kg, due to presence of the SiO_2 shell around the magnetic Fe_2B core. From the ratio of M_s at 5 T (Fig. 6.5) for Fe_2B and Fe_2B/SiO_2 particles, we estimate the mass ratio between SiO_2 and Fe_2B to be about 3. Combining this value with the mass densities of SiO_2 and Fe_2B we estimate that the thickness of the SiO_2 coating is the same as the radius of the Fe_2B core. This is in agreement with SEM results

suggesting that the mean radius of Fe_2B/SiO_2 particles is about twice that of Fe_2B [284].

6.4 Structural and superconducting properties of Fe-based doped MgB_2 compounds

Nano-Fe and as-synthesized nano-Fe_2B and Fe_2B/SiO_2 particles were added to MgB_2 compound. The effect of magnetic doping on the properties of MgB_2 superconductor will be described in this section.

6.4.1 Structural analysis

Results of X-ray diffraction analysis performed on pure and doped MgB_2 samples are presented in Figs. 6.6-6.7. As can be noted, MgB_2 is the main phase observed in all samples. All samples also contain a minor amount of MgO impurity, which is common in *in-situ* fabricated MgB_2 compound.

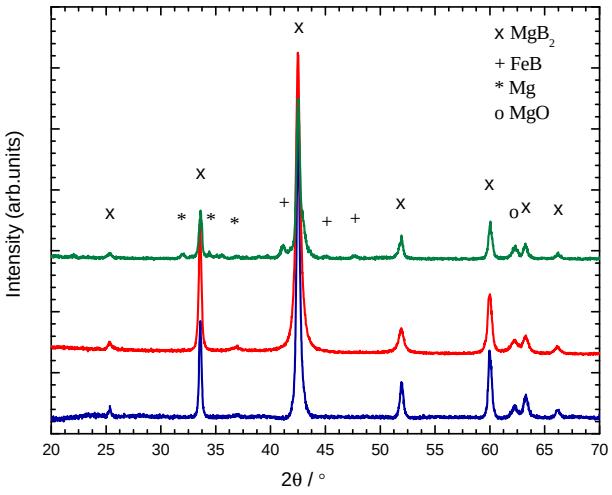

Figure 6.6: *X-ray diffraction patterns for 0 % (blue), 1 % (red) and 5 % (green) Fe-doped MgB_2 samples.*

Addition of 1 wt.% of Fe into MgB_2 does not result in the formation of (de-

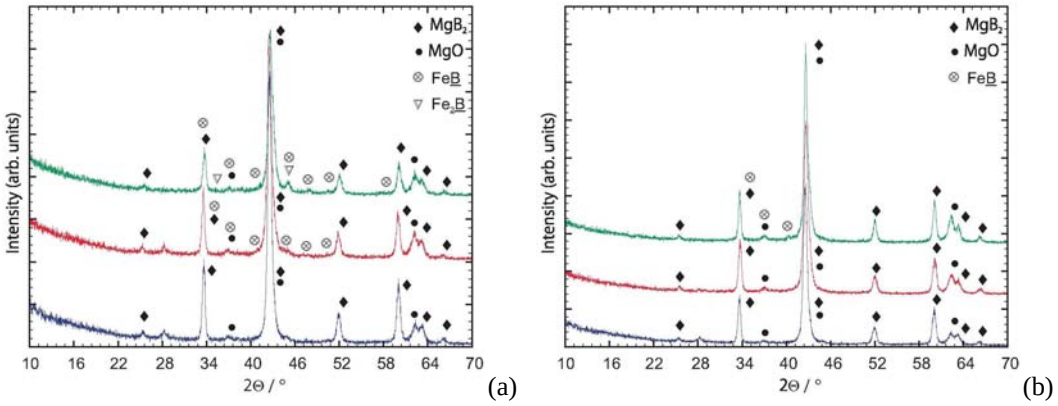

Figure 6.7: *X-ray diffraction patterns for 0 % (blue), 3 % (red) and 7.5 % (green) of Fe_2B-doped (a) and Fe_2B/SiO_2-doped (b) MgB_2 samples [290].*

tectable) new phases in the sample (Fig. 6.6). It is well known from the literature [289] that Fe can substitute for Mg up to 1.2 %. However, it is not possible to detect any noticeable shift of the a or c-lattice parameters in the XRD patterns to confirm this. By increasing the Fe doping level up to 5 wt.%, it became evident that Fe was reacting with B to form FeB phase. This causes the deficiency of B and leaves some unreacted Mg (Fig. 6.6).

Samples doped with nano Fe_2B particles (Fig. 6.7(a)) show the presence of Fe_2B and FeB phases [290], the amounts of which increase with increasing (from 3 to 7.5 wt.%) Fe_2B doping level. Note, similar phases were detected in as-synthesized Fe_2B particles (Fig. 6.2).

MgB_2 samples doped with Fe_2B/SiO_2 (Fig 6.7(b)) [290] do not show the presence of Fe_2B/SiO_2 particles, as they were in the amorphous state (Fig. 6.2). In the sample doped with 7.5 wt.% Fe_2B/SiO_2 some minor amount of FeB phase was observed. In addition, increasing the Fe_2B/SiO_2 doping level resulted in higher levels of MgO impurities. The appearance of FeB phase and increased MgO phase indicate that, to some extent, the reaction between Mg, B, and SiO_2 and Fe_2B occurred during thermal treatment of the samples.

6.4.2 Critical temperature

Fig. 6.8 shows the real part of the ac susceptibility of MgB_2 samples with addition of 0, 1, and 5 wt.% nano Fe particles. As can be seen, T_c of the pure sample is 38 K, while it drops to 36 and 34.5 K with increasing Fe-doping level from 1 to 5 wt.%.

Figs. 6.9 and 6.10 [290] present the temperature dependence of the resistance for MgB_2 wires with different levels of Fe_2B and Fe_2B/SiO_2 doping at zero applied magnetic field, which were used for determination of T_c values. As can be seen, the critical temperature is reduced as the doping level increases.

Fig. 6.11 shows the dependence of T_c on doping levels of Fe, Fe_2B, and Fe_2B/SiO_2 materials. The suppression rate, dT_c/dx, is estimated to be 0.4 K/wt.%, 0.6 K/wt.% and 0.5 K/wt.% for Fe, Fe_2B, and Fe_2B/SiO_2 dopants, respectively. This suppression of T_c caused by the Fe-based dopants studied is rather moderate compared to Mn doping, which destroys superconductivity in MgB_2 at the doping level of only 2 % Ref.[112]. It is established that the major source for the rapid T_c drop in Mn-doped MgB_2 is the magnetic pair-breaking effect through spin-flip scattering [112; 291; 292; 293]. On the other hand, dT_c/dx is higher than in the Al-doped samples, for which the depression of T_c was attributed to the band filling effect and, therefore, reduction in the density of states. A theoretical study [293] and following NMR investigation [289] showed the *nonmagnetic* nature of Fe in the MgB_2 lattice, as well as the absence of magnetic impurities which could act as a source for spin-flip scattering and a nearly unchanged density of states. The reduction of T_c in Fe-doped MgB_2 samples can be explained by the specific electronic nature of Fe, which changes the phonon frequency and/or electron-phonon coupling strength [294], which are crucial for T_c in a BCS phonon-mediated (MgB_2) superconductor.

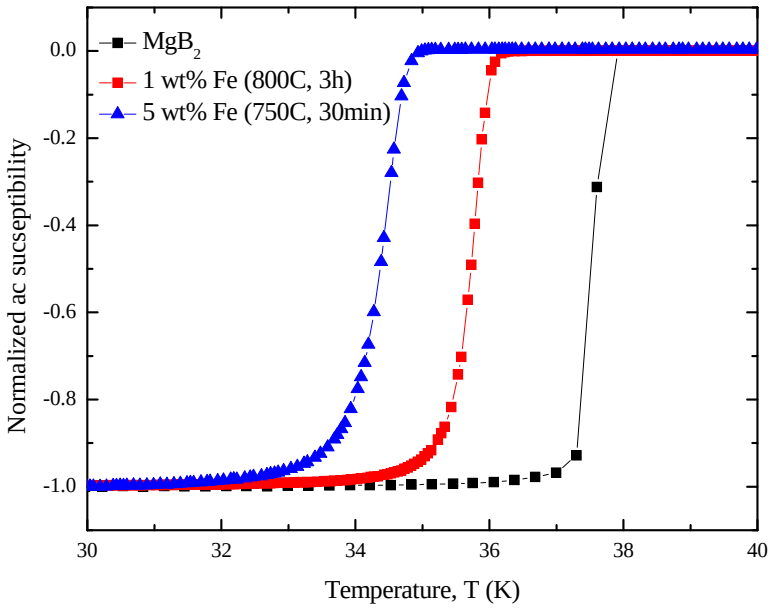

Figure 6.8: *Normalized ac susceptibility vs. temperature for Fe-doped MgB_2 samples (T_c defined at the upper transition point).*

6.4.3 Critical current density and irreversibility field. Kramer plot.

Magnetic field dependencies of the critical current density of MgB_2 samples doped with nano-Fe, Fe_2B, and Fe_2B/SiO_2 particles are presented in Figs. 6.12 - 6.14, re-

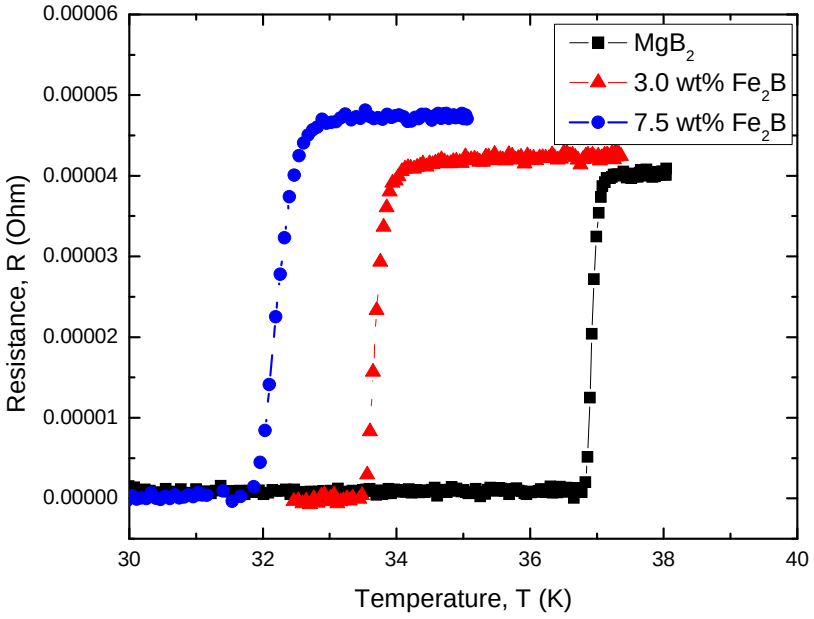

Figure 6.9: *Resistivity vs. temperature curves at 0 T for Fe_2B-doped MgB_2 samples (T_c defined from the lower transition point) [290].*

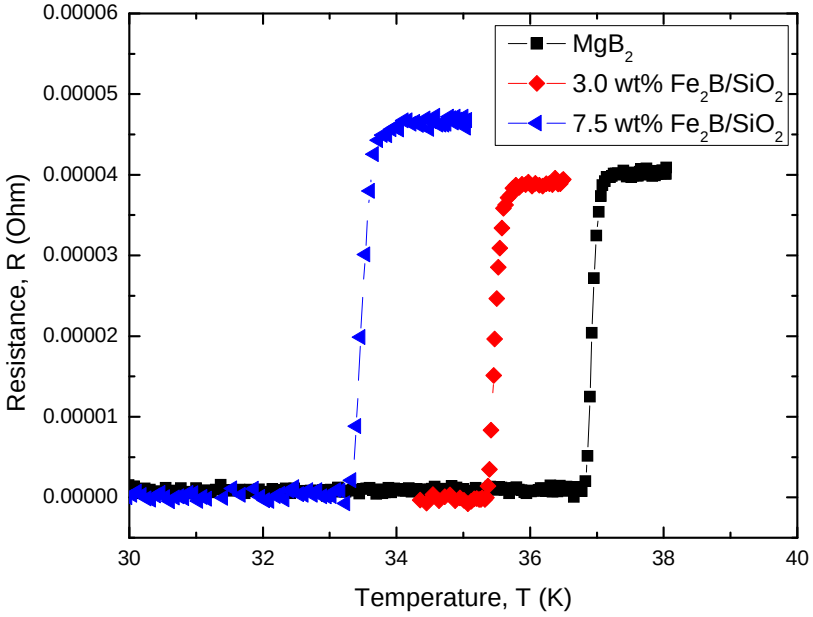

Figure 6.10: *Resistivity vs. temperature curves for Fe_2B/SiO_2-doped MgB_2 samples (T_c defined from the lower transition point) [290].*

spectively. Critical current densities of Fe_2B (Fig. 6.13) and Fe_2B/SiO_2 (Fig. 6.14) doped MgB_2 wires are slightly lower than those for bulk the Fe-doped MgB_2 (Fig. 6.12) sample in the low field region. This is a commonly observed feature for

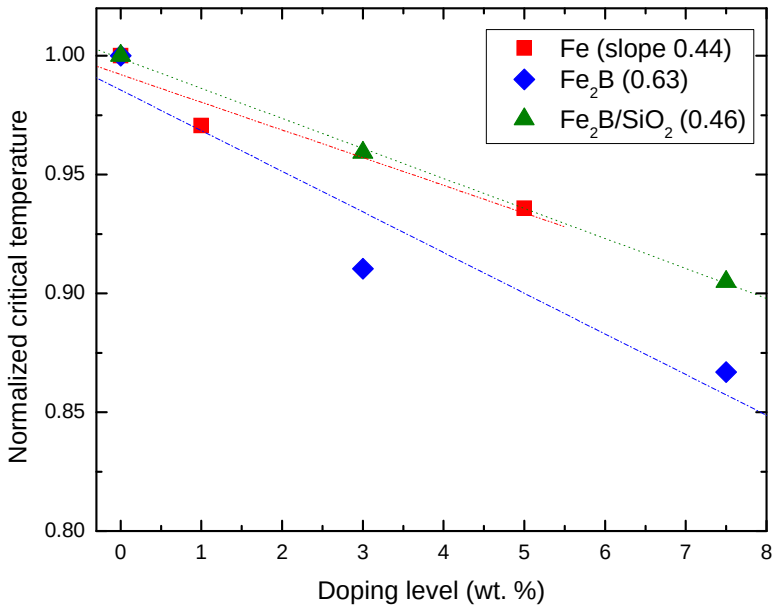

Figure 6.11: *Critical temperature versus doping level for Fe_2B and Fe_2B/SiO_2-doped MgB_2 wires [290] and Fe-doped MgB_2 bulk samples.*

samples in the form of wires due to reduced density of the superconducting core compared to bulk samples.

As can be seen, Fe-based doping results in decreased $J_c(B_a)$ performance of MgB_2 superconductors over a whole range of magnetic fields and at both temperatures studied. Increasing the Fe-based doping level leads to further $J_c(B_a)$ degradation. Among the samples studied, Fe doping results in more substantial depression of critical current density of MgB_2 superconductor. In contrast, Fe_2B/SiO_2 doping is the least detrimental to the superconducting properties in MgB_2.

As Fe-based dopants lose their magnetic nature in the MgB_2 environment [293; 289; 294], we speculate that the reason for $J_c(B_a)$ degradation lies in the reduced T_c values (Figs. 6.8-6.10) and the increased number of impurity phases, as observed by XRD (Figs. 6.1-6.2) of the studied Fe-based doped MgB_2 samples. Indeed, the dT/dx values observed were reduced in a sequence for Fe_2B, Fe, and Fe_2B/SiO_2-doped MgB_2 samples. Similarly, the amount of impurity phases was smallest in the Fe_2B/SiO_2-doped MgB_2 sample (Fig. 6.10), which showed the least detrimental effects on $J_c(B_a)$ performance.

The irreversibility field values, B_{irr}, are plotted as a function of doping level in Fig. 6.15. All doped samples show reduced B_{irr} values; samples with higher doping levels have lower values of B_{irr} over the whole temperature range. The dB_{irr}/dx rate is highest in the Fe doped and smallest in the Fe_2B/SiO_2 doped samples. As B_{irr} is sensitive to pinning, reduction of B_{irr} with increasing doping in MgB_2 samples shows that pinning strength was not enhanced by the Fe-based dopants studied, which is in contrast to the data obtained in [163; 280; 281; 282].

We used the B_{irr} values presented in Fig. 6.15 to plot J_c(20 K) versus normalized magnetic field B/B_{irr} for the samples studied Fig 6.16. We note that the curves show a similar trend for pure and doped samples, which indicates similar

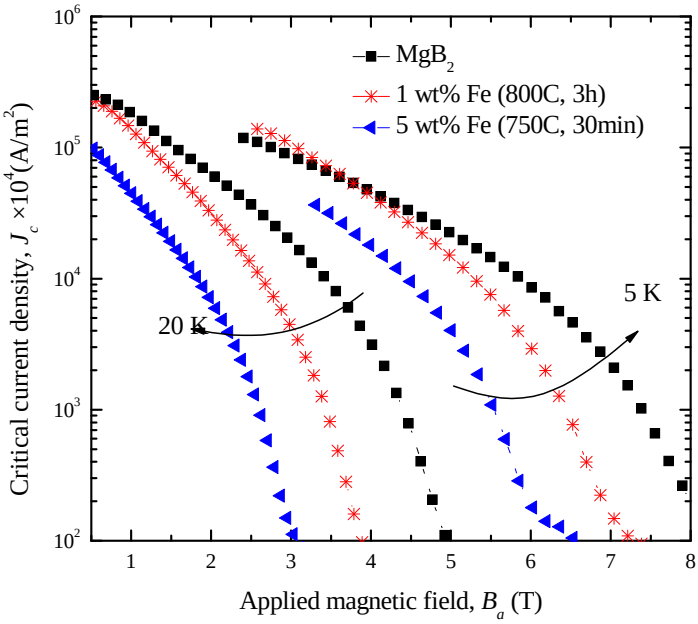

Figure 6.12: *Magnetic critical current density vs. applied magnetic field for Fe-doped MgB_2 samples.*

pinning types (e.g. grain boundaries as in pure MgB_2) in all samples. This confirms that magnetic pinning of vortices was not achieved in Fe-based doped MgB_2 samples.

Fig. 6.17 shows Kramer's plots of $J^{1/2}B^{1/4}$ versus applied magnetic field B_a.

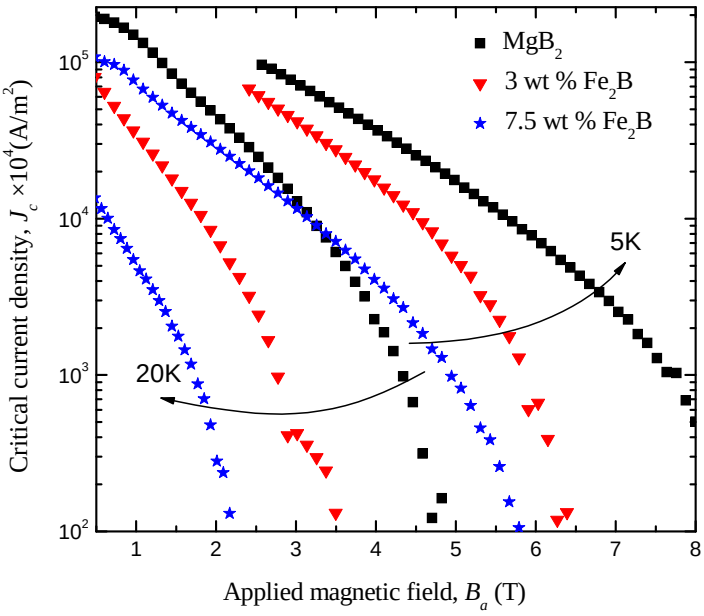

Figure 6.13: *Magnetic critical current density vs. applied magnetic field for Fe_2B-doped MgB_2 wires.*

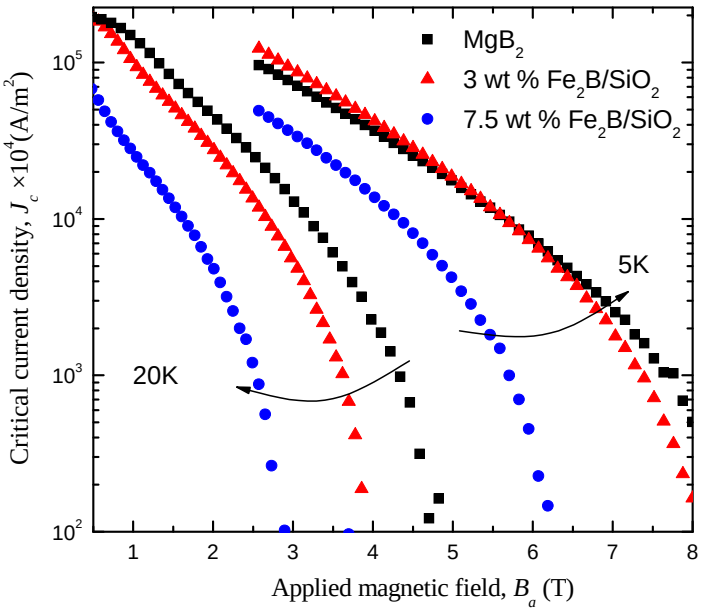

Figure 6.14: *Magnetic critical current density vs. applied magnetic field for Fe_2B/SiO_2-doped MgB_2 wires.*

Deviation of $J^{1/2}B^{1/4}(B_a)$ curves from linear behaviour indicates on considerable inhomogeneity in all samples studied. We believe that, due to magnetic nature of Fe-based dopants (Fig. 6.5), magnetic nanoparticles were not well dispersed in the samples studied, which thus had large agglomerations of initial Fe, F_2B, and

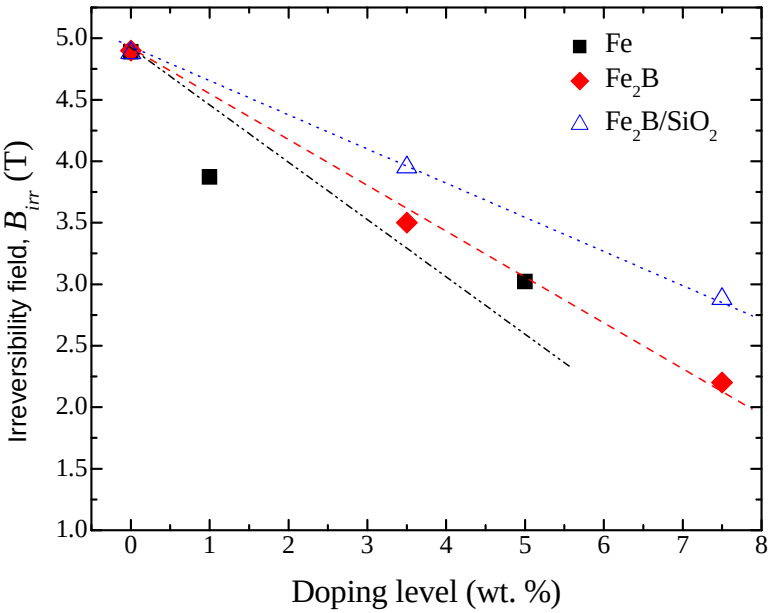

Figure 6.15: *20 K irreversibility fields of MgB_2 samples vs. doping level of Fe-based particles.*

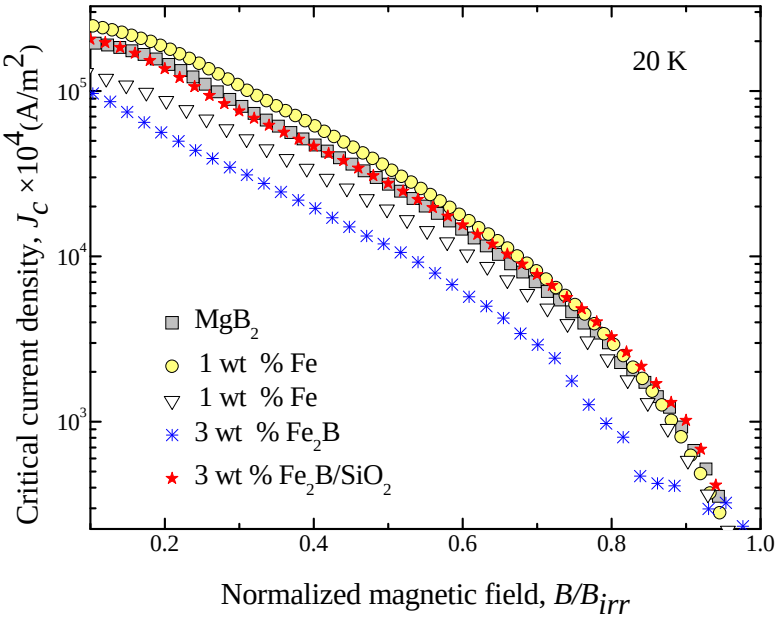

Figure 6.16: *Critical current density versus normalized magnetic field B/B_{irr} for undoped and doped (Fe, Fe_2B and Fe_2B/SiO_2) MgB_2 wires at 20 K.*

Fe_2B/SiO_2 particles. After MgB_2 formation, Fe_2B and FeB impurity phases may appear not only inside, but also between the grains. In addition, large agglomerations of dopants do not serve as flux pinning centers, but they do act as weak links degrading current flow in the samples, as shown in Figs. 6.12-6.14.

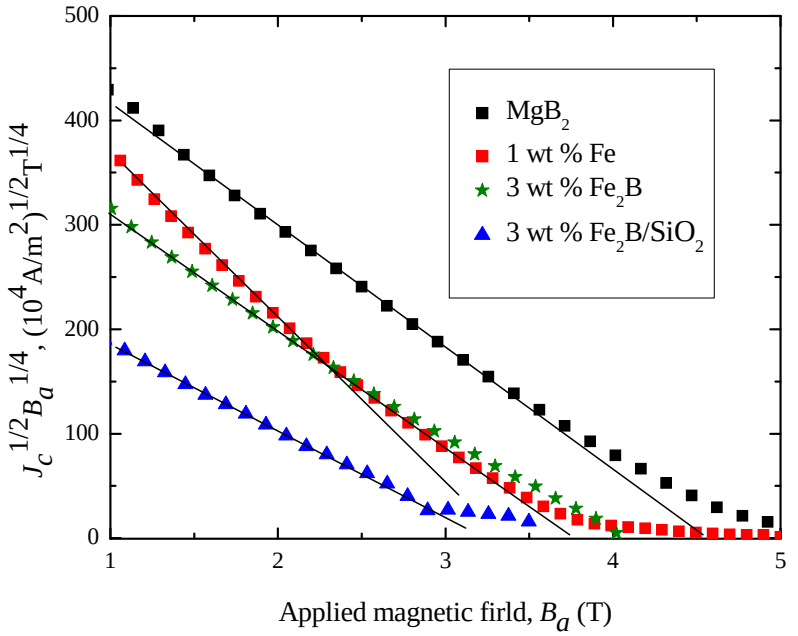

Figure 6.17: *Kramer's plots for undoped and doped (Fe, Fe_2B, and Fe_2B/SiO_2) MgB_2 samples.*

6.5 Conclusions

F_2B and Fe_2B/SiO_2 magnetic particles were prepared via aqueous chemical synthesis. Magneto-structural characteristics of the Fe-based dopants studied showed that the Fe and Fe_2B dopants were in crystalline form, while the Fe_2B/SiO_2 particles were amorphous. The mean size of as-synthesized Fe_2B and Fe_2B/SiO_2 particles is 84 and 177 nm, respectively. Magnetic moment was reduced for the studied particles with the highest moment observed for nano-Fe and the smallest for Fe_2B/SiO_2 particles. In terms of MgB_2 wire preparation, this property can enhance the mixing and dispersion of magnetic particles within the superconductor.

In the MgB_2 with Fe-based dopants samples we did not find any detectable level of Fe substitution on Mg or B sites. All the magnetic materials studied as dopants caused strong suppression of the transition temperature of MgB_2 with increasing content of the magnetic additions. The rate for dT/dx suppression was highest in the Fe_2B-doped MgB_2 sample and smallest in the Fe_2B/SiO_2 doped MgB_2 sample. This is correlated with reduction of magnetization in Fe_2B/SiO_2 doping material and possibly less deterioration of the Mg/B ratio in these samples.

Degradation with increasing doping level of critical current density ($J_c(B_a)$) and irreversibility field, B_{irr}, values implies that magnetic doping was not achieved. Subsequent Kramer's plot analysis indicated that one of the reasons for the $J_c(B_a)$ degradation was inhomogeneous distribution of magnetic dopants.

Chapter 7

Electromagnetic performance of polymer C-based doped MgB_2 superconductors

7.1 Introduction

In recent years the rapid development of MgB_2 superconductor has been based on the simple fabrication and relatively high transition temperature of 39 K in this compound (compared to low temperature superconductors). This temperature enables the application of MgB_2 superconductor at temperatures of around 20 K, facilitating the use of simple, cost-effective, and reliable cryocoolers. Additional benefits of the MgB_2 compound are the simple crystal structure, the low cost of the starting materials, and the fact that grain boundaries have a less detrimental effect on the supercurrent flow than in high temperature superconductors [66]. MgB_2 superconductor is a promising candidate for large-scale applications, such as magnetic resonance imaging systems, fault current limiters, and high field magnets [16; 193]. However, the in-field critical current density, $J_c(B_a)$, is still below the

practical level. This has stimulated the research community to find the way to improve both the upper critical field value, B_{c2}, which sets the limit to existence of superconductivity, and the $J_c(B_a)$ performance for the desired 20 K application of MgB_2 superconductors.

Enormous efforts have been made to improve the superconducting properties of MgB_2 via chemical doping. It was experimentally established that a significant enhancement of MgB_2 superconducting properties at high fields can be achieved with carbon-based doping. Among nano-C based dopants, nano-SiC results in the most effective enhancement of electromagnetic properties of MgB_2 superconductor [118; 103; 298].

Recently, a new "liquid mixing" approach for C-doping has been developed in our group. This significantly simplifies fabrication of MgB_2 superconductor with carbon doping and enhances the effectiveness of doping. In this new technique [146], the doping material (glucose, $C_6H_{12}O_6$) is dissolved in water and mixed with the boron powder. This technique results in coating of each individual boron particle by a nanolayer of highly reactive amorphous carbon [149]. This configuration facilitates incorporation of C into B sites in the MgB_2 lattice during the sintering and results in enhancement of the electromagnetic characteristics in the final $MgB_{2-x}C_x$ superconductor [146; 149; 148]. Importantly, the "liquid mixing" approach would assure homogeneous distribution of the dopant in $MgB_{2-x}C_x$ superconductor in the form of *wire*.

It was shown that "liquid mixing" technique is applicable to a wide range of carbohydrates [148] and C-based organic materials [126; 150; 152; 299; 300; 301; 305]. The majority of these polymer C-based dopants were studied in $MgB_{2-x}C_x$ bulk samples. However, for practical application, demonstration of the properties of MgB_2 doped wires is required. Among the wide range of studied polymers, polycarbosilane (C_2H_6Si) and sugar ($C_{12}H_{22}O_{11}$) are particularly promising for

practical application. This is because polycarbosilane is oxygen free and is a polymer analog to nano-SiC compound [150], known as the best dopant among the nano-C based dopants, while table sugar (or sucrose) is a readily available source of carbon. Moreover, the bulk MgB_2 samples with these dopants demonstrated the highest improvement of (i) critical current density at high magnetic fields (J_c (5 K, 8 T) = 3×10^9 A/m^2 for polycarbosilane-doped MgB_2 [302]), and (ii) very high upper critical field for the sample with sugar doping (36 T at 5 K) [147], compared to their nano-C based analogs. It was also suggested that further increase in the sintering temperature (> 870°C) for sugar-doped samples may result in more significant B_{c2} enhancement.

Thus, in this Chapter, the work reported on doping the MgB_2 pellets by sucrose ($C_{12}H_{22}O_{11}$) and polycarbosilane (C_2H_6Si) [147; 305] is extended to doping of MgB_2 wires with the same compounds. This is important because MgB_2 is expected to be used in practical applications mostly in the form of wires and the reaction process and vortex pinning could be different than for MgB_2 prepared in pellet form. The effects of sintering temperature on the microstructure and superconducting properties of MgB_2 samples have been systematically investigated.

7.2 Experimental

Pure and doped Fe-clad MgB_2 wires were fabricated by *in-situ* processing using the standard PIT technique. Powders of Mg (99% purity, particle size of 1-11 μm) and amorphous B (99% purity) were used as host materials. The sucrose (CHO) and polycarbosilane (CHSi)-doped samples were prepared by the "liquid mixing" approach. The level of added dopants was 10 wt.%. The CHO and CHSi compounds were dissolved in deionized water and toluene (C_7H_8), respectively. An appropriate amount of B powder was added to the dopant in the solvent and

well mixed with a mortar and pestle by hand. After the liquid mixing stage, the wet slurry of boron, dopant, and solvent was dried in a vacuum chamber at 200°C overnight to remove the remaining solvent and moisture. After drying, the powder was ground, mixed with Mg powder, and ground again.

Mixed powders were packed into Fe tubes and then drawn to a diameter of 1.42 mm. Several short samples from each wire were sintered at temperatures of 600, 650, 700, 870, or 950°C for 30 min followed by cooling to room temperature in the furnace. A high purity argon gas flow was maintained throughout the sintering process to avoid oxidation. The samples prepared at 600 and/or 650, 700, 870, or 950°C were designated as MB-650, MB-700 or MB-950 for reference samples, CHSi-600, CHSi-650, CHSi-700 or CHSi-950 for polycarbosilane doped MgB_2 samples, and CHO-650, CHO-870 or CHO-950 for sucrose doped MgB_2 samples, respectively.

Phase investigation was performed using an X-ray diffractometer with Cu Kα radiation. The fraction of phases and lattice parameters were estimated via Rietveld refinement of the XRD patterns. The microstructure of samples was investigated by Scanning Electron Microscopy (SEM). The magnetization of the superconducting cores extracted from the wires was measured at 20 K using a Physical Properties Measurement System (PPMS, Quantum Design) with a magnetic field applied perpendicular to the wire long axis. The magnetic J_c was derived using Eq. (3.3). Resistivity vs temperature curves were collected using the 4-points technique at applied magnetic fields up to 16 T. Transport current was measured by the pulsed method with rectangular pulse duration of 1 ms and a maximum current of 370 A.

7.3 Phase and crystal structure

XRD patterns for samples fabricated at temperatures of 650 and 950°C are presented in Fig. 7.1(a) and (b), respectively. Data obtained by Rietveld refinement (crystal lattice parameters and phase fraction), as well as some superconducting characteristics for the samples studied are summarized in Table 7.1.

As can be seen, all samples investigated have MgB_2 as the main phase and some amount of MgO. It should be noted that pure and CHSi-doped MgB_2 samples have the same amount of MgO phase, while in CHO doped samples higher levels of MgO are detected (Table 7.1). This is due to the fact that sucrose originally has high amount of oxygen ($C_{12}H_{22}O_{11}$). This sample was processed with deionized water, which also could increase the level of oxygen in the system. In the CHSi-doped samples, a high level (17.21 wt.%) of Mg_2Si phase was observed for the sample sintered at low (650°C) temperature, but it dropped to nearly zero (0.15 wt.%) in the sample treated at high (950°C) temperature (Fig. 7.1 and Table 7.1). This trend for Mg_2Si formation is similar to what is seen in the literature for samples with nano-SiC doping [134; 251; 304]. In CHSi-doped samples, free

Table 7.1: *Some parameters of samples studied. $\triangle a$ defines changes in the a lattice parameter as a result of C incorporated into the MgB_2 lattice on B sites; x - actual level of C in $Mg(B_{1-x}C_x)_2$ estimated from $\triangle$a values [303].*

Sample	a, Å	$\triangle a$, Å	x, %	non-s/c phase, %	FWHM of (101) peak, deg.	T_c, K	B_{c2}, (5 K), T
MB-650	3.081	-	-	8.55 (MgO)	0.5	36.8	21
CHO-650	3.071	0.010	2.3	16.36 (MgO)	0.626	35.0	34
CHSi-650	3.076	0.005	1.2	7.70 (MgO)	0.542	34.5	32
				17.21 (Mg_2Si)			
MB-950	3.087	-	-	7.34(MgO)	0.364	38.3	17
CHO-950	3.072	0.014	3.2	18.06 (MgO)	0.508	36.2	37
CHSi-950	3.077	0.010	2.2	9.15 (MgO)	0.396	36.6	30
				0.15 (Mg_2Si)			

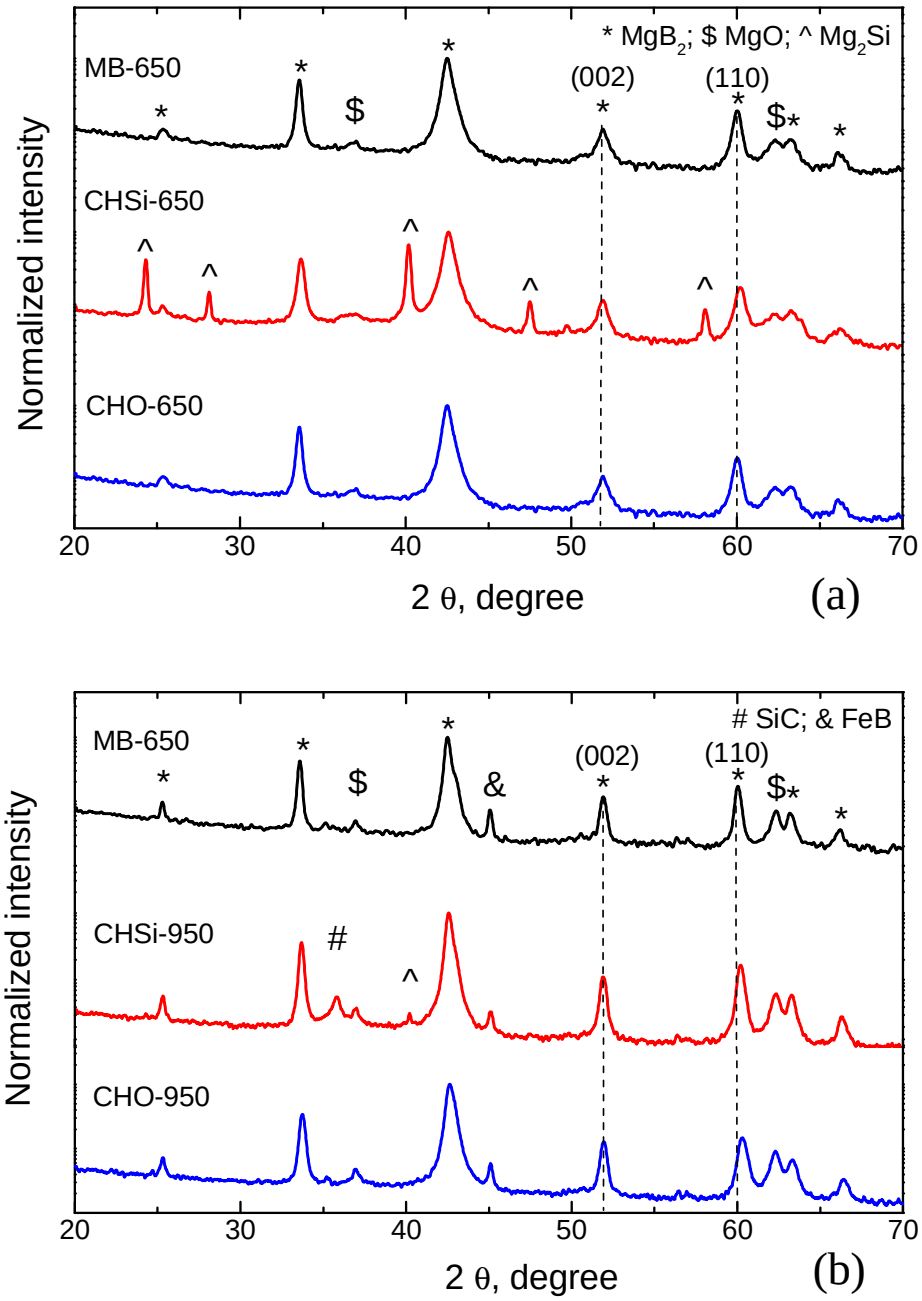

Figure 7.1: *X-ray diffraction patterns of samples sintered at temperatures of 650°C (a) and 950°C (b).*

atoms of Si and some of the C released after CHSi decomposition at 300°C [150] form SiC compound at a temperature of 950°C (Fig. 7.1(b)). At higher sintering temperature (> 900°C) Fe from the sheath material reacts with boron [223]. Therefore, some amount of FeB phase was detected in samples sintered at 950°C.

Fig. 7.2 shows the position of the (110) and (002) peaks in the XRD patterns, which reflect changes in the a and c lattice parameters of the hexagonal MgB_2 crystal lattice, respectively. There is no shift observed in the (002) peak position for the C-doped MgB_2 samples, indicating that the c lattice parameter remains unaffected by C-based doping. The estimated value of the c parameter is 3.526±0.004Å for all samples. In contrast, shift of the (110) peak to higher 2θ values is observed in C-doped MgB_2 samples indicating on reduction of a parameter (Δa) due to C substitution for B in the MgB_2 crystal lattice. The larger the Δa value the higher the level of C incorporated in the MgB_2 crystal lattice [303; 117].

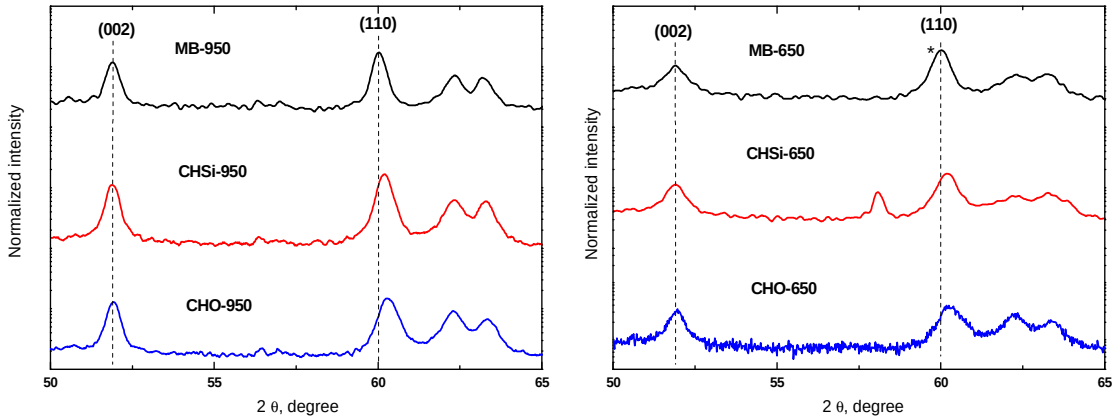

Figure 7.2: *Selected region of X-ray diffraction pattern demonstrating change of* a *and* c*-lattice parameters (corresponding to (110) and (002) peak position respectively) of samples sintered at temperatures of 650°C (a) and 950°C (b).*

Analysis of Δa values obtained in samples studied (Table 7.1) indicate that: i) CHSi doping results in a smaller level of C substitution for B in MgB_2 lattice than CHO doping at both temperatures studied; and ii) the higher the sintering temperature, the larger the level of C is substituted for B in both CHSi and CHO-doped MgB_2 samples. These are in agreement with the results obtained in polycarbosilane- and sugar-doped bulk MgB_2 samples [147; 305].

7.4 Micro- and nanostructure

SEM images of the typical microstructure of pure and doped samples subjected to high and low sintering temperatures are presented in Fig. 7.3. Notably sintering at 650°C yields samples with small loosely connected grains (Fig. 7.3(a,c,e)), while high temperature sintering (950°C) results in samples with larger and better consolidated grains (Fig. 7.3(b,d,f)).

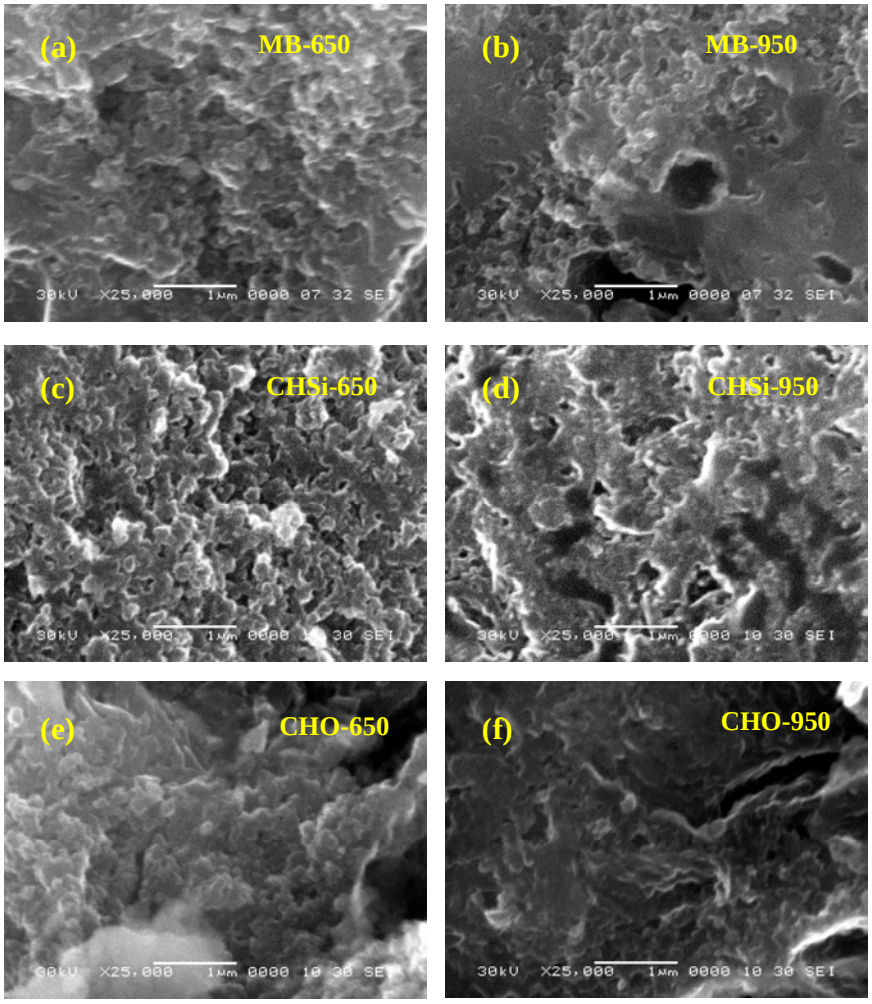

Figure 7.3: *SEM images of the microstructure of pure (a, b), CHSi- (c, d) and CHO-doped (e, f) MgB_2 samples fabricated at 650°C and 950°C.*

This conclusion is also supported by FWHM (Full Width at Half Maximum) values estimated from XRD patterns of studied samples (Table 7.1). According

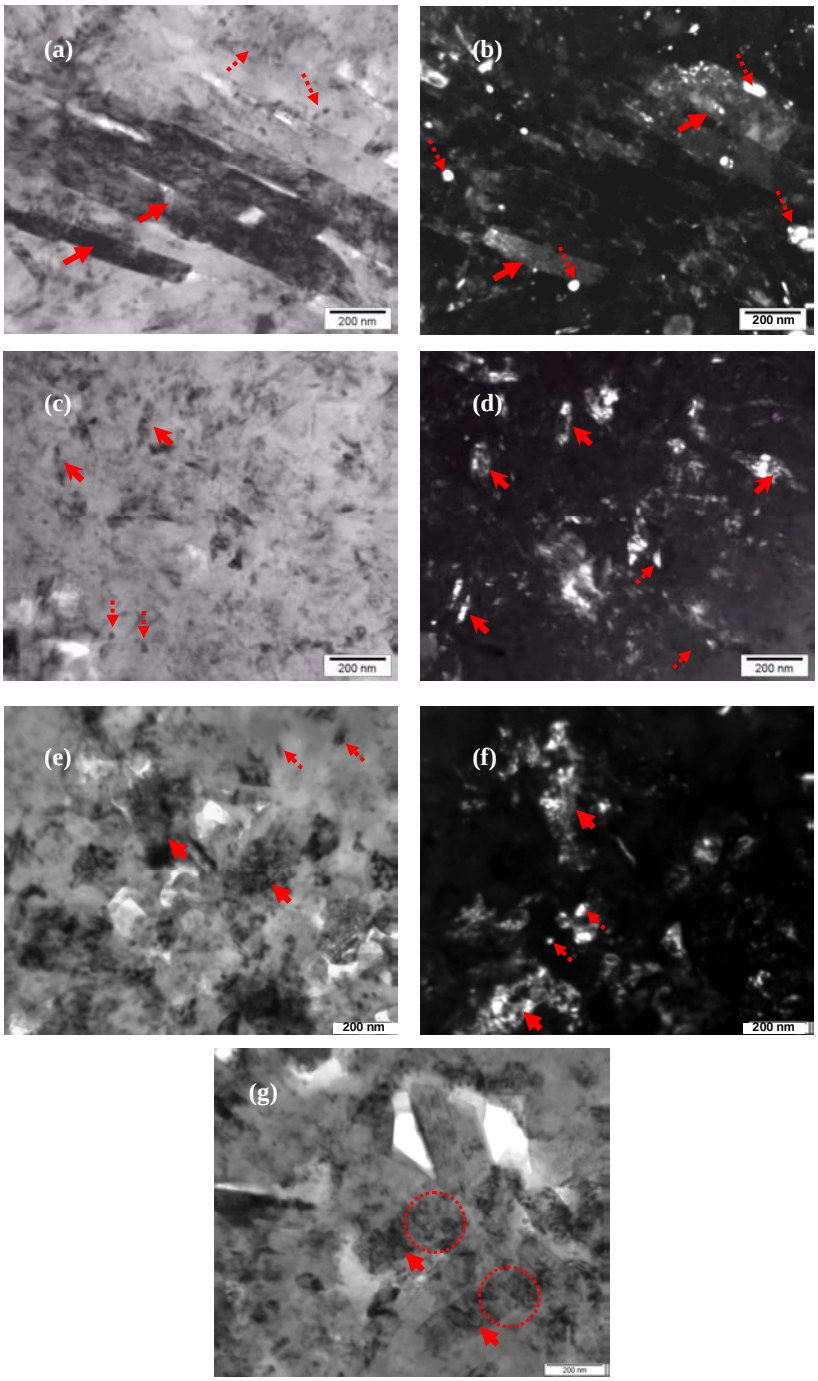

Figure 7.4: *Bright field (left) and dark field (right) TEM images of the nanostructure of MB-650 (a, b), CHSi-650 (c, d), and CHO-950 (g, e, f) samples. The arrows and circled areas are explained in the text.*

to the Scherrer equation, grain size is inversely proportional to the FWHM value ($D_p = 0.94\lambda/FWHM\cos\theta$, where D_p is crystal size, λ is wavelength, and θ is the peak position). Thus, the decreasing FWHM values for all samples with increasing

sintering temperature indicates growth of grain size in the samples.

In addition, FWHM values of C-doped samples are larger than for the reference MgB_2 sample due to worse MgB_2 crystallinity associated with C-substitution for B in these samples and reduction of grain size compared to reference sample, which is likely induced by doping. Note that high values of FWHM are obtained for CHO doped samples. Indeed, the increase in the FWHM values is a collective effect of several factors, including the high level of C substitution into the MgB_2 lattice, high intrinsic strain caused by large amounts of MgO (and/or Mg_2Si for CHSi-doping) impurities and defects generated by C-substitution [261].

A TEM study was performed on corresponding bulk [305; 147] samples prepared simultaneously with samples in the form of wire. Bright- and dark-field TEM images of the MB-650, CHSi-650, and CHO-950 samples are presented on Fig. 7.4. These help to estimate the grain size within each sample and demonstrate the defective nanostructure of samples studied.

The grain size is varied within each sample. As can be seen, the microstructure of samples consists of round grains with sizes up to 50 nm (marked by broken arrows), and grains elongated in one direction (shown by solid arrows). The elongated grains have sizes up to 50 nm×400 nm and 50 nm×150 nm in MB-650 [Fig. 7.4(a, b)] and CHSi-650 samples [Fig. 7.4(c, d)], respectively [305]. Increas-

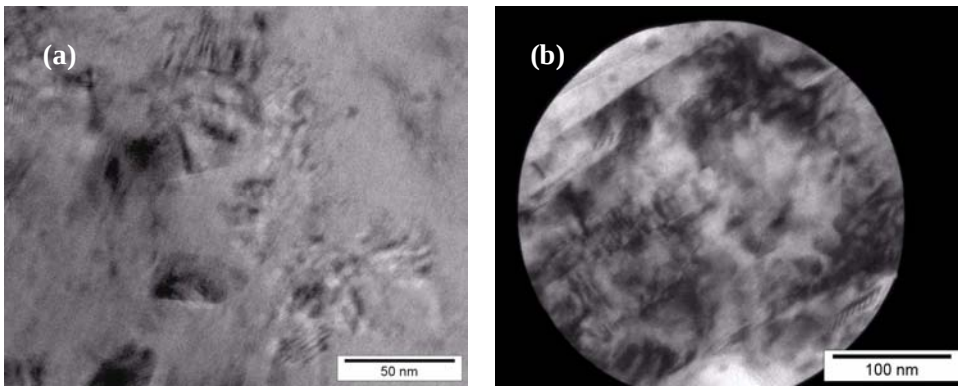

Figure 7.5: *Nanoimpurities (a) and crystal lattice defects (b) observed in C-doped MgB_2 samples.*

ing the sintering temperature results in significant grain growth. For instance, the grain size is about 100 nm×400 nm in the CHO-950 sample [Fig. 7.4 (e, f)] [147].

It is remarkable that the doped samples have high levels of nanoimpurities [MgO and/or Mg_2Si, Fig. 7.5(a)] and crystal lattice defects, such as dislocations and stacking faults [Fig. 7.4 (g) and shown in Fig. 7.5(b)], which are clearly seen in the doped samples and are in agreement with previously published data [72; 73; 82; 306]. A dense network of crystal lattice defects within MgB_2 grains in the doped samples is generated by incorporation of C on B sites in the MgB_2 crystal lattice and by large numbers of inclusions such as MgO in CHO-doped samples, and MgO and/or Mg_2Si in polycarbosilane doped MgB_2.

7.5 Superconducting properties of the CHO and CHSi-doped MgB_2 superconductors

7.5.1 Critical temperature

Critical temperature (T_c) values of the studied samples are presented in Table 7.1. In carbon-doped samples the decrease in T_c is due to carbon being incorporated into the crystal lattice [103; 140; 141; 307]. At the sintering temperature of 650°C, the T_c value of the CHSi-650 sample is lower compared to the CHO-650 sample in spite of the fact that the level of C substitution is higher in the CHO-650 sample. This is due to the high level of impurities (Mg_2Si, MgO) in the CHSi-650 sample (Table 7.1), which result in inhomogeneity of this sample and reduce its apparent T_c.

Higher sintering temperature (950°C) results in better crystallinity and homogeneity of all samples, and, thus, higher T_c values are observed in all samples. For more homogeneous samples (CHO-950 and CHSi-950), the higher the level of C in

the MgB_2 lattice, the lower the T_c value is (Table 7.1).

7.5.2 Resistivity and effective cross section

Resistivity values at 40 K and 300 K for the studied samples are presented in Table 7.2. It is well known that the resistivity depends on several parameters, including porosity, grain connectivity, inclusions/defects within the grains, and alloying [75; 140]. As can be seen from Table 7.2, doped samples have higher resistivity values compared to pure samples. This is consequence of increased electron scattering on the larger number of grain boundaries, impurities, and denser network of crystal lattice defects, which were observed in the CHSi and CHO doped samples (Table 7.1, Fig. 7.4).

Increasing the sintering temperature results in formation of bigger and better

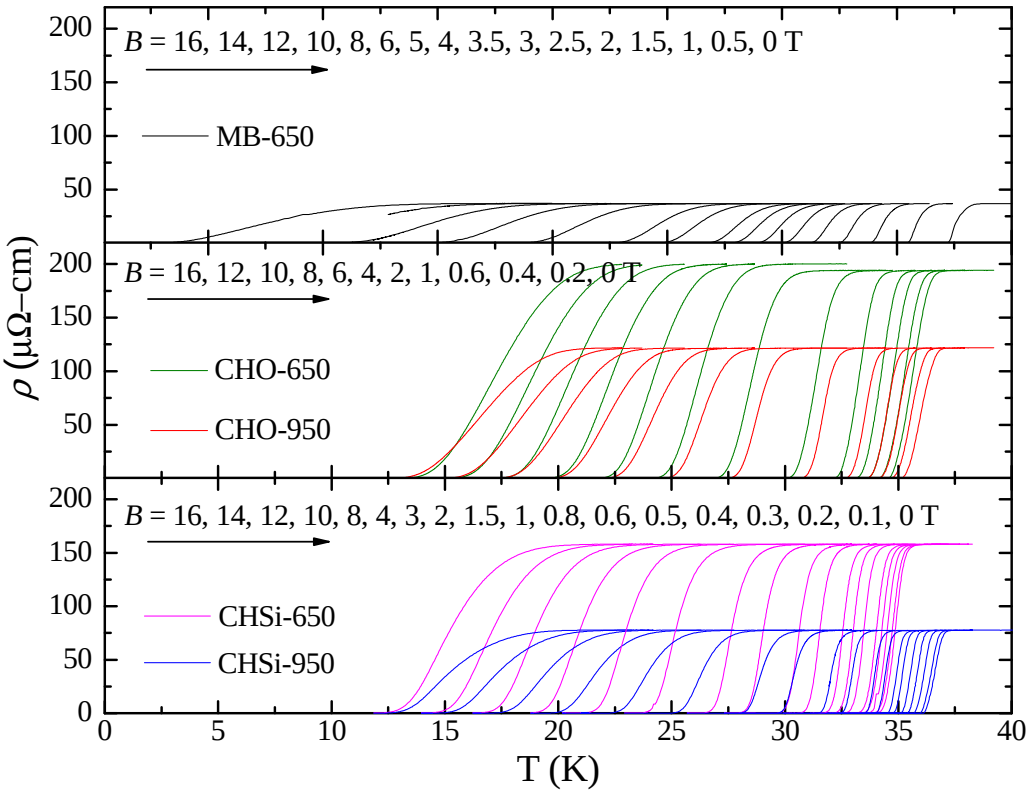

Figure 7.6: *Resistivity of pure and doped MgB_2 wires sintered at different temperatures and applied magnetic fields.*

Table 7.2: *Resistivity and effective cross section (A_{eff}) of the samples.*

Sample	$\rho(40\ K)$, $\mu\ \Omega$cm	$\rho(300\ K)$, $\mu\ \Omega$cm	$\Delta\ \rho$ $\mu\ \Omega$cm	A_{eff} %
MB-650	37	86	46	15
CHO-650	194	290	96	7.6
CHSi-650	158	230	72	10.1
MB-950	32	74	39	19
CHO-950	122	177	55	13.3
CHSi-950	78	124	46	15.8

consolidated grains (i. e. improved connectivity between grains) (Fig. 7.3), and, thus, decreased ρ_{40K} and ρ_{300K} values for all pure and doped samples (Table 7.2). However, resistivity values for the doped samples are still higher that those for pure MgB_2. This is again due to the increased number of crystal lattice defects in the doped samples as a result of the observed higher level of C substitution on B sites in the MgB_2 crystal lattice at high temperature.

It should be noted that at both sintering temperatures, CHO doped samples have higher resistivity values than CHSi-doped MgB_2 (Fig. 7.6). This indicates that CHO doping generates a higher level of defects, which results in more significant electron scattering during current flow, and/or more impurities that are detrimental to the current flow.

According to Rowell [75], values of resistivity at 40 and 300 K can be employed for estimation of the effective crosssection of samples (A_{eff}) which carries electrical current: $A_{eff} = \Delta\rho_{ideal}/\Delta\rho$, where $\Delta\rho = \rho_{300K} - \rho_{40K}$ of the sample and the $\Delta\rho_{ideal}$ value is obtained from a fully connected sample. The values of A_{eff} for the studied samples are presented in Table 7.2. $\Delta\rho_{ideal}$ is assumed to be 7.3 $\mu\Omega$cm, as for dense MgB_2 filament made by chemical vapor deposition [77].

As can be seen from Table 7.2, doping results in reduction of the effective crosssection. This may be due to the fact that doping induces large numbers of impurities such as MgO and Mg_2Si (Table 7.1). Increasing the sintering temper-

ature results in larger A_{eff} values in all samples. This is likely to be due to the fact that grains are much better connected in these samples, which correlates well with the microstructural changes observed in Fig. 7.3.

7.5.3 Upper critical field

The upper critical field $B_{c2}(T)$ values were obtained from the $\rho(B_a, T)$ curves using Eq. (1.4) (Fig. 7.7). The B_{c2}(5 K) values for the samples studied were estimated by a linear extrapolation of the $B_{c2}(T)$ curves to lower temperatures, and the resulting values are presented in Table 7.1.

The $B_{c2}(\sim 1/\xi^2)$ in the dirty limit is inversely proportional to the electron mean free path, ℓ ($1/\xi = 1/\ell + 1/\xi_0$) [308]. Electron scattering in pure MgB_2 samples mainly occurs on grain boundaries and crystal disorder, the amounts of which are higher in samples sintered at lower temperatures than in samples subjected to higher sintering temperature [249]. Thus, the pure MgB_2 sample sintered at lower temperature (MB-650) shows a higher B_{c2} value than the sample prepared at higher temperature (MB-950).

The doping of MgB_2 with C-based dopants increases B_{c2} values when compared to the pure sample. The highest (among all the samples studied) B_{c2} value of 37 T was obtained for the CHO doped wire sintered at 950°C. This value is the highest for nano-C doped samples reported in the literature. For comparison, the B_{c2} value of 32 T has been measured in nano-C doped samples [307], and B_{c2} of 30 T has been obtained for $MgB_{2-x}C_x$ wire segments [140], double-wall carbon nanotubes [141] and nano-SiC doped samples [264].

The observed enhancement of B_{c2} in CHSi and CHO-doped samples is due to structural changes, which affect the scattering mechanism in the two-band MgB_2 superconductor [308]. A higher level of C substitution (higher x value) in the CHO doped samples correlates well with a more significant enhancement of the

upper critical field, as observed for the CHO-650 (x = 2.3 %, B_{c2} = 34 T) and the CHO-950 (x = 3.2 %, B_{c2} =37 T) samples. However, it is not the case for CHSi-doped wires. As can be seen, the B_{c2} value is as high as 32 T for the CHSi-650 sample having a lower level of C-substitution (x = 1.2 %, Table 7.1) compared to 30 T for the CHSi-950 sample with a higher level of C-substitution (x = 2.2 %). This implies that electron scattering on MgO and a large amount of Mg_2Si (17.21 wt.%) impurities, as well as defects caused by these impurities (dislocations, staking faults, etc.), and small grain size play the major role in the improvement of the upper critical field in the CHSi-650 sample. Indeed, it was emphasized above that the amount of Mg_2Si impurities drops to nearly zero in the CHSi-950 sample. Combining this fact with the large, more crystalline and

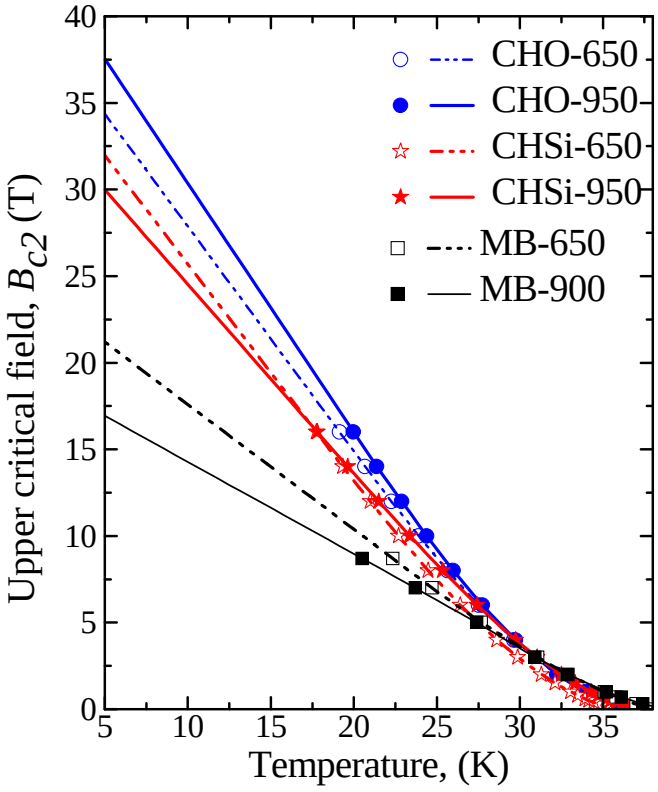

Figure 7.7: *The upper critical field vs. temperature dependence, $B_{c2}(T)$, for the samples studied. Symbols represents experimentally observed data, while the lines show corresponding linear extrapolations.*

better consolidated grains formed at 950°C, the electron mean free path and the coherence length were increased, but the B_{c2} value was decreased in CHSi-950 sample, in spite of the fact that the level of C substitution was nearly doubled.

7.5.4 Critical current density. Pinning mechanism

Fig. 7.8 shows the field dependence of the critical current densities for pure, and the CHSi- (Fig. 7.8(a)) and CHO-doped (Fig. 7.8(b)) MgB_2 samples. As can be seen, increasing the sintering temperature results in enhancement of the $J_c(B_a)$ performance over the entire field range for both dopants investigated.

It should be noted that doping MgB_2 superconductor with CHSi and CHO results in J_c degradation at low applied magnetic field (at 20 K: $B_a <$ 4 T for CHSi and $B_a <$ 4.2 T for CHO doping) compared to pure MgB_2 sample. This is consistent with the high level of secondary phases and thus smaller values of the effective crosssection (A_{eff}, Table 7.2) in the doped samples when compared to pure MgB_2 samples. Increasing the sintering temperature from 650 to 950°C results in higher T_c (Table 7.1) and A_{eff} (Table 7.2) values in all samples, and thus, improves current-carrying ability in all samples studied.

In contrast, at higher applied magnetic fields ($B_a \geq$ 4.2 T), $J_c(B_a)$ of doped samples outperforms one for the pure MgB_2 sample. Among the dopants studied, a higher in-field $J_c(B_a)$ performance is observed for the CHSi-950 sample compared to the CHO-950 sample (Fig. 7.9(a)). In order to explain the in-field $J_c(B_a)$ behaviour, the pinning mechanism in the pure and doped samples has been analyzed.

The average pinning force, F_p, has been estimated using the equation $F_p = J_c \times B_a$. The normalized pinning force (F_p/F_p^{max}) as a function of reduced magnetic field $b = B_a/B_{irr}$ is shown in Fig. 7.9(b, c, d) for pure, CHSi-doped and CHO-doped samples, respectively. The B_{irr} values were obtained as fields for which

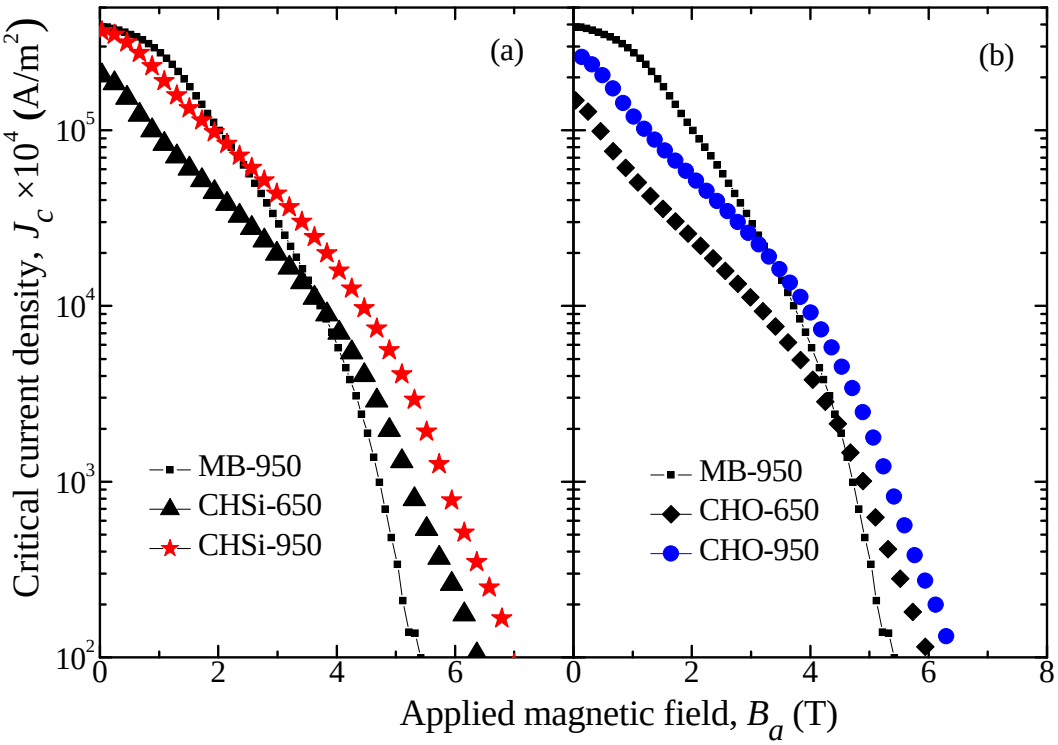

Figure 7.8: *20 K $J_c(B_a)$ performances of CHSi (a) and CHO-doped (b) MgB_2 samples sintered at temperatures of 650 and 950°C.*

$J_c(20K) = 10^6 A/m^2$. Fits to the experimental F_p/F_p^{max} curves for pure and doped samples were made the using equation $F_p/F_p^{max} \propto b^p(1-b)^q$, as shown by Dew-Hughes [78].

For the CHSi-950 and CHO-950 samples the fitting parameters $p = 0.5$ and $q = 2.2 \pm 0.2$ for normalized pinning force were obtained at $T = 20$ K. According to the Dew-Hughes model [78], these values correspond to normal core pinning on surface pins, such as grain boundaries and crystal lattice defects (dislocations, staking faults, etc.) As demonstrated above, the level of these defects generated by high levels of MgO impurities and C-substitution is higher in the CHO-950 sample, and this results in higher B_{c2} and, therefore, should lead to enhanced $J_c(B_a)$ behaviour compared to the CHSi-950 sample. However, the $J_c(B_a)$ performance observed in Fig. 7.9(a) does not follow this prediction. We believe that this occurs due to the formation of the large amount of MgO phase, which likely results in

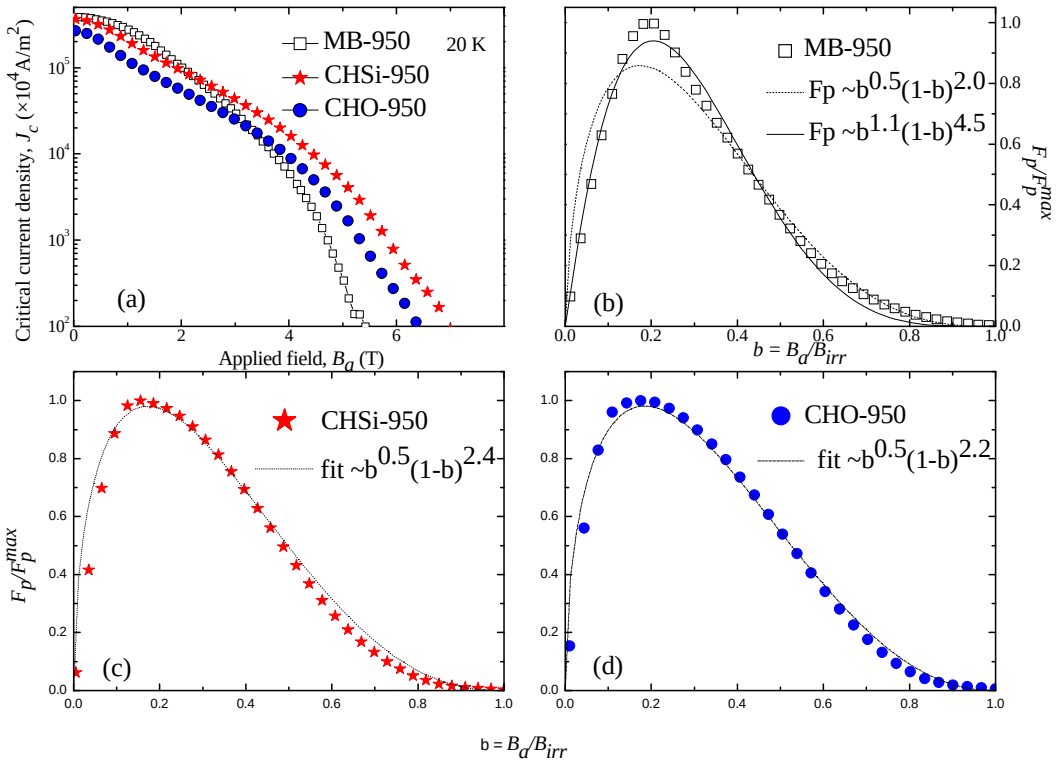

Figure 7.9: *(a) 20 K $J_c(B_a)$ performances of CHSi and CHO-doped MgB_2 samples sintered at 950°C. (b-d) Normalized volume pinning force (F_p/F_p^{max}) versus reduced magnetic field (B_a/B_{irr}) at 20 K with fitting curves.*

formation of supercurrent blocking layers around the grains and reduces the total critical current density in the CHO doped sample.

It was confirmed by a number of studies [71; 84; 147; 309; 310] that in pure MgB_2 samples, the grain boundaries provide the main pinning source. However, the fitting parameters for F_p/F_p^{max} curve with $p = 0.5$ and $q = 2$ do not fit the experimental data, especially at low fields (Fig. 7.9(b)). With the aim of accurate fitting, we obtained values of $p \simeq 0.95$ and $q \simeq 3.06$ [dotted line in Fig. 7.9(b)], which seem to be in good agreement with fitting parameters reported in the literature [70; 311; 312]. The observed pinning force behavior has not yet been explained. We speculate that in the low field region, the current carrying ability is mainly determined by connectivity and structural transparency rather than by the pinning properties in the pure MgB_2 samples [313; 312]; thus, a

reasonable fit of the pinning force in the low field region is not achieved, as shown in Fig. 7.9(b).

In order to demonstrate the potential of CHO and CHSi-doped MgB_2 samples for practical application, the electromagnetic behaviour of the corresponding MgB_2 wires was investigated. Figs. 7.10 and 7.11 show the transport $J_c(B_a)$ performances of the CHSi- and CHO-doped MgB_2 wires, respectively, measured in the temperature range from 5 to 30 K with applied magnetic fields up to 16 T.

As can be seen, the transport supercurrent properties of CHSi and CHO-doped samples are in good agreement with the magnetic properties of the superconducting core. First, the values of (transport) critical current densities of doped wires exceed the ones for pure MgB_2 in the temperature range from 5 to 20 K. Therefore doping enhances the performance and enables application of MgB_2 superconductor at high magnetic fields. Second, an obvious tendency has been observed, where increasing sintering temperature results in higher critical current density values for doped samples. Similar behaviour was observed from magnetic measurements of superconducting cores (Fig. 7.8), which has been explained by enhanced upper critical fields (Fig. 7.7), large number of pinning cites (defects) and, therefore, a large pinning force (Fig. 7.9) in doped samples.

Transport measurements, performed at lower temperatures, clearly demonstrate that the level of critical current density improvement is different at high (20 K) and low (5 K) temperatures (Figs. 7.10, 7.11). For instance, the values of J_c at 5 K (10 T) are about one order of magnitude higher for CHO and CHSi-doped samples compared to pure MgB_2 samples (at 5 K J_c(10 T) are 2×10^7, $\sim10^8$ and 2×10^8 A/m^2 for MB-700, CHO-950 and CHSi-700 samples, respectively). However, the ratio of J_c values for doped and non-doped samples at 20 K (6 T) is reduced to factors of 4 and 3.2 in CHSi and CHO-doped samples compared to pure MgB_2. This is due to the fact that B_{c2} becomes considerably larger (Fig. 7.7), while

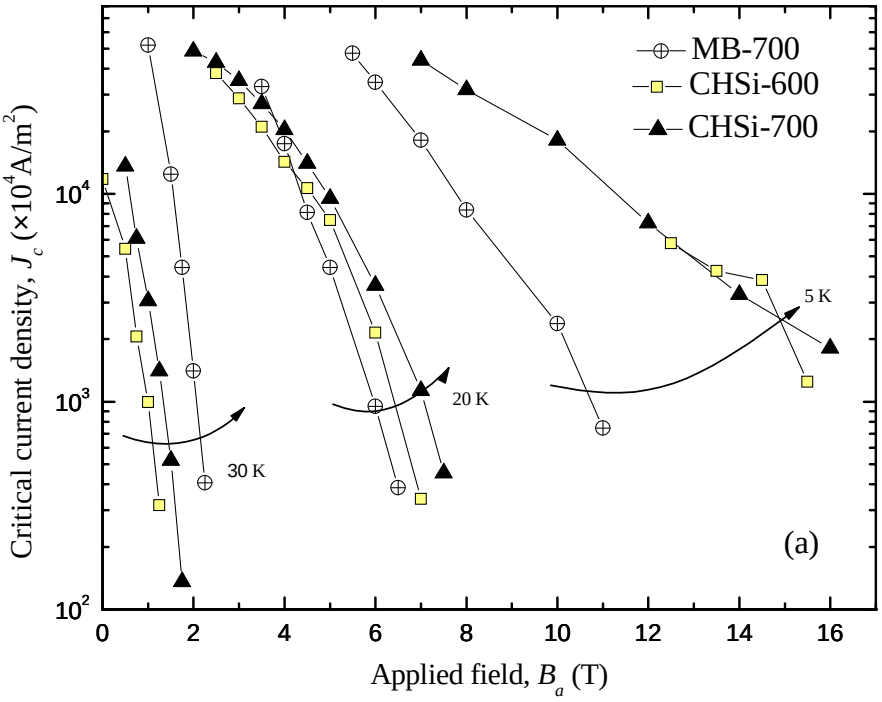

Figure 7.10: *Transport $J_c(B_a)$ performances of CHSi-doped MgB_2 samples sintered at temperatures of 600 and 700°C.*

the coherence length ξ ($B_{c2} \sim 1/\xi^2$) is smaller for doped samples. Generally, the crystal lattice is much more defective in doped than in pure MgB_2, and thus, defects with smaller sizes, such as crystal lattice defects (dislocations, nanodomains, stacking faults, etc.), which are less effective for pure samples with larger ξ, become effective pinning sites. Therefore, the generally stronger enhancement of $J_c(B_a)$ for the doped samples at lower temperatures (5 K, Fig. 7.8), at which $\xi(T)$ is the smallest (i. e. $B_{c2}(T)$ is larger) has been observed.

It can also be noted that enhancement of critical current density is observed at high field regions. The steep slope of the $J_c(B_a)$ characteristic for pure MgB_2 sample suggests that this sample has higher supercurrent values in the field regions $B_a \leq 6$ T at 5 K and $B_a \leq 4$ T at 20 K. This correlates well with data observed by magnetization measurements (Fig. 7.6). These observations imply that in the low field region connectivity of grains and transparency of structure are crucial factors

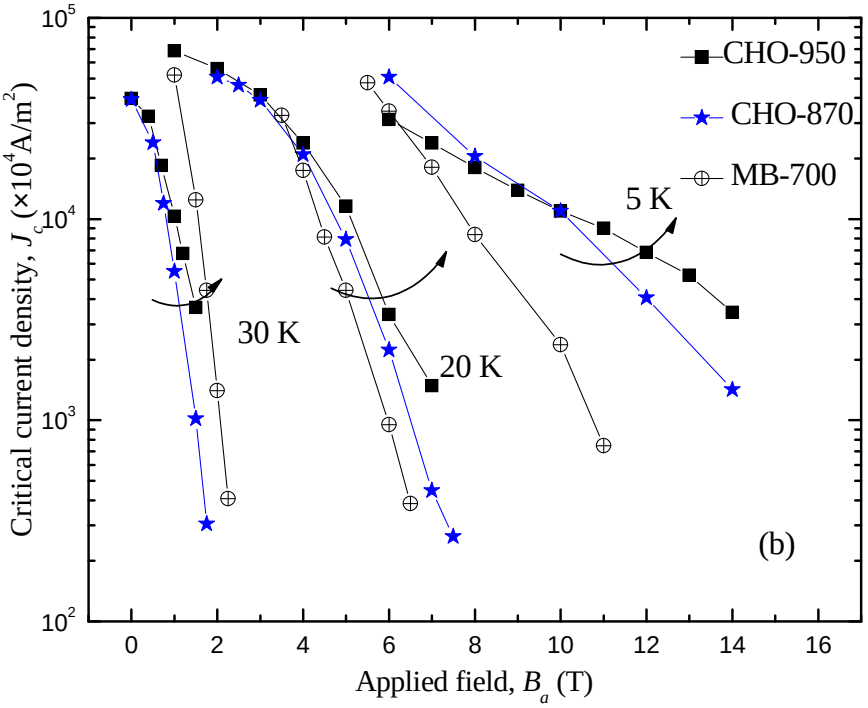

Figure 7.11: *Transport $J_c(B_a)$ performances of CHO-doped MgB_2 samples sintered at temperatures of 700-950°C.*

for current carrying ability in polycrystalline MgB_2 samples. Indeed, the large amount of impurities (Mg_2Si and/or MgO) in doped samples, which may reside not only within, but also in between grains, results in greater current dissipation in bottlenecks to current flow, as compared to pure MgB_2 samples, particularly at low magnetic fields, where supercurrent is large.

At the measurement temperature of 30 K, the $J_c(B_a)$ of the pure MgB_2 sample outperforms those for the doped MgB_2 samples. this is due to the fact that superconductivity is generally suppressed in the close vicinity of the transition temperature in the doped samples, i.e. T/T_c for doped samples is substantially smaller than for non-doped ones at 30 K. At lower temperatures, this difference is not as large. Note, the higher the sintering temperature, the smaller the degradation of $J_c(B_a)$ that is observed as a result of improved crystallinity, and higher T_c and A_{eff} values in these samples.

7.6 Summary

The effect of processing temperature on the structure and superconducting properties of CHSi and CHO doped MgB_2 wires have been investigated. It is observed that increasing sintering temperature results in higher levels of C substitution on B sites in the MgB_2 crystal lattice. This substitution is larger in CHO doped samples compared to CHSi doped samples. Increasing sintering temperature results in higher B_{c2} values for CHO doped samples. A B_{c2} value of 37 T (at 5 K) is estimated for the CHO-950 sample, which exceeds the B_{c2} values achieved by nano-C doping. In contrast, B_{c2} decreases in CHSi-doped samples with increasing sintering temperature. The in-field $J_c(B_a)$ performance in doped wires is improved compared to the reference wires due to enhanced B_{c2} values and stronger pinning on lattice defects caused by impurities and C substitution. However, the high level of MgO impurities (up to 18 wt.%) reduces transparency for current flow and results in lower $J_c(B_a)$ performance of CHO doped samples compared to CHSi doped MgB_2 samples.

Chapter 8

Conclusion

In this work, two issues that are important from a practical point of view - *thermal stabilization* and *improvement of electromagnetic performance by doping* - of MgB_2 superconductor have been systematically investigated.

In order to achieve thermal stabilization, a layer of Al outside of Fe-clad MgB_2 wires was created by the powder-in-tube (PIT) technique. Fe was used as a barrier between the Al and the Mg+2B unreacted mixture to prevent reaction between these components during sintering. In addition, Fe assured a higher density in the superconducting core of the final wires due to better compaction of unreacted Mg and B powders during drawing. It was demonstrated that the PIT technique can be used for fabrication of Al/Fe-clad MgB_2 wires with outer diameters of 1.42 mm. It also was observed by x-ray diffraction that a low temperature sintering at temperatures in the range of 600-630°C for a duration of 30 min is sufficient for formation of MgB_2 compound. In contrast, when fabricated in a similar way, Al/Fe-clad SiC-doped MgB_2 wires required longer sintering time (180 min) at the temperature of 600°C. Low temperature sintering results in less crystalline MgB_2 and thus a lower (compared to 39 K) critical temperature (T_c), which slightly increases from 35.7 K to 36.7 K with increasing sintering temperature from 600°C

to 630°C. SiC doping of MgB_2 wires resulted in C substitution on B sites and subsequent further reduction of T_c to 32.9 K (for 600°C) and 33.2 K (for 630°C). The Al/Fe-clad pure and SiC-doped MgB_2 wires had (magnetic) critical current density values of 7×10^6 - 1.8×10^7 A/m^2 and 2×10^7 - 3.8×10^7 A/m^2 at 20 K and 4.5 T, respectively, which are sufficient for practical application. SEM study of Al-stabilized Fe-clad MgB_2 wires demonstrated that Al is compatible with the Fe barrier under sintering conditions 600-620 °C for 30 min. Under these conditions, there is no reaction between Fe and Al materials. However, increasing the sintering temperature (640-650 °C) or the duration (620 °C for 90 min) results in formation of Al_3Fe alloy. The formation of this alloy may result in reduction of the thermal conductivity of the stabilizer, but is preferable for better connectivity between Fe and Al layers.

In order to assure better connectivity of the Al stabilizer and the Fe barrier in Al/Fe-clad MgB_2 wires, a new hot aluminizing approach was developed. The benefit of this technique is that it can be applied on already optimized Fe/MgB_2 wires. Alternatively, this can be used for simultaneous formation of Fe/MgB_2 conductor and its coating with Al stabilizer. The results of this study demonstrated that submerging the unreacted Fe/MgB_2 wire in a molten Al bath kept at temperatures of 670°C and 770 °C for durations of 30 and 10 min, respectively, is essential for complete MgB_2 phase formation and fabrication of a thin (about 10 μm) Al layer. Favorably, the thickness of the Fe-barrier was systematically reduced for samples prepared at higher temperatures. Magnetic measurements performed at 10 K on Fe-clad MgB_2 wire showed more strongly pronounced flux-jump behaviour in the low field region (0-2 T) compared to Al/Fe-clad MgB_2 wires (having a similar thickness of Fe layer). Furthermore, the transport critical current density of Al/Fe/MgB_2 wires with reaction during aluminizing achieved the level of 2.2×10^8 A/m^2 at 20 K and 3.5 T, which is only slightly lower than

$J_c = 3.7\times10^8$ A/m^2 for the reference Fe/MgB_2 sample.

Importantly, the results of this work imply that powder-in-tube and hot aluminizing demonstrate feasible approaches for fabrication of Al-stabilized MgB_2 wires, which are required for practical application of high current magnesium diboride superconductor. Moreover, these open up the opportunity for fabrication of lightweight Al/MgB_2 superconductors for airborne and aerospace applications, where weight is a critical parameter.

The feasibility of introducing magnetic pinning sites into *in-situ* MgB_2 conductor has been investigated with the help of Fe-based dopants. As systematic study of nano-Fe particles, as well as home-made Fe_2B and SiO_2 coated Fe_2B particles was performed. It was found that precursor Fe and Fe_2B were in crystalline form, while Fe_2B particles covered by SiO_2 were in the amorphous phase. Fe_2B and SiO_2 coated Fe_2B particles had sizes of 84 and 177 nm, respectively. Magnetization of precursor dopants is reduced in a sequence 210 Am^2/kg, 103 Am^2/kg to 26 Am^2/kg for the investigated nano-Fe, Fe_2B, and Fe_2B/SiO_2 particles, respectively. The Fe-based dopants studied resulted in significant degradation of the critical temperature of MgB_2 conductor. Based on theoretical studies and nuclear magnetic resonance (NMR) studies found in the literature, the studied Fe-based dopants have a non-magnetic nature in MgB_2. We believe that one of the possible reasons for the degradation of T_c in the samples studied was the large amount of impurity phases formed between Mg, B, and the doping materials during sintering. Magnetic critical current densities, $J_c(B_a)$ and irreversibility field values, B_{irr}, of undoped and doped MgB_2 samples with different amounts of Fe, Fe_2B, and SiO_2-coated Fe_2B magnetic nanoparticles do not show any enhancement of flux pinning associated with the magnetic interaction between vortices and magnetic nanoparticles. Moreover, rather good scaling of $J_c(B_a/B_{irr})$ curves for doped wires with that for undoped wire seems to indicate that the dominant

pinning mechanism is the same (grain boundary pinning) in both undoped and doped samples. Strongly curved Kramer's plots of the doped samples indicate a rather inhomogeneous distribution of the magnetic dopants. We believe that the observed $J_c(B_a)$ and B_{irr} degradation for MgB_2 superconductor with the introduction and increasing doping level of the studied Fe-based dopants is due to (i) alteration of the phonon frequency and/or electron-phonon coupling strength by the electronic nature of Fe-based dopants, causing T_c *reduction*, (ii) *inhomogeneity* introduced by the magnetic nature of the dopants studied, and (iii) the presence of *impurity* phases, which act as weak links between superconducting MgB_2 grains. Thus, our results do not confirm the theoretical prediction of improved superconducting characteristics in Fe/MgB_2 structures fabricated in bulk and tape *in-situ* MgB_2 samples.

For practical application it is crucial to enhance the electromagnetic characteristics of MgB_2 *wires*. In this thesis, the work on structural and superconducting properties of polymer C-based doped MgB_2 pellets was extended to the wires, which are required for practical applications. The effects of sintering temperature were investigated, and comparative study of $C_2H_{12}Si_6$ (CHSi) and $C_{12}H_{22}O_{11}$ (CHO) dopants on performance of MgB_2 wires was performed. First, it was observed that polymer-C doping enhances the effectiveness of doping. This was demonstrated by a larger level of C substitution on B sites in the MgB_2 crystal lattice when compared to nano-C doping. For the dopants studied, a larger level of C substitution, x, was observed in $C_{12}H_{22}O_{11}$ doped MgB_2 wires. The x values further increased with increasing sintering temperature from 650°C to 950°C for both types of dopants studied. A higher level of C substitution for B (x values) results in a higher density of nanostructural crystal lattice defects (stacking faults, dislocations, etc.) in the doped samples. Moreover, X-ray diffraction analysis revealed large number of secondary phases: MgO (for CHO-doped MgB_2), and

MgO and Mg_2Si for CHSi-doped MgB_2. In both, nano-defects and impurities reduce the electronic mean free path and increase electron scattering, resulting in the enhanced upper critical field (B_{c2}) of CHSi and CHO-doped MgB_2 wires. For instance, at a temperature of 5 K, B_{c2} of 37 K was observed for the CHO-doped MgB_2 sample sintered at 950°C (with $x = 3.2$ wt.%), and B_{c2} of 32 K was observed for CHSi-doped MgB_2 wire fabricated at 650°C (with $x = 1.2$ wt.%). Furthermore, the dense network of nano-defects formed in polymer C-doped MgB_2 samples improved pinning, and thus resulted in enhanced current current density ($J_c(B_a)$) in the doped samples. This improvement is more strongly pronounced in samples prepared at higher sintering temperatures, at which more nano-defects (pinning sites) and better connectivity of grains were observed. In particularly, at the temperature of 5 K and applied magnetic field of 10 T, (transport) critical current densities are 2×10^7, $\sim10^8$ and 2×10^8 A/m^2 for pure (fabricated at 700°C), CHO-doped (950°C) and CHSi-doped (700°C) MgB_2 wires. This trend is consistent with magnetic measurements. Note that in spite of the large B_{c2} value, the CHO-doped MgB_2 sample has lower $J_c(B_a)$ performance. We believe that this is due to formation of a large amount of MgO impurities in the CHO-doped MgB_2 sample, which degrades current flow in the wire. *Thus, oxygen free $C_2H_{12}Si_6$ dopant has high potential for fabrication of C-doped MgB_2 wires for practical applications. Furthermore, the density of the superconducting core should be enhanced in order to obtain higher current carrying ability in Fe-clad MgB_2 wires.*

Bibliography

[1] H. Kamerlingh Onnes, *Comm. Phys. Lab. Univ. Liden* **122**, and **124**, 1226 (1911).

[2] BES Report on Basic Research Needs for Superconductivity, http://www.sc.doe.gov/bes/reports/abstracts.html♯SC

[3] W. Meissner and R. Ochsenfeld, *Naturwissenschaften* **21**, 787 (1933).

[4] M. Tinkham, "Introduction to superconductivity", New York: McGraw-Hill, (1996).

[5] F. London and H. London, Proc. Roy. Soc. (London) **A149**, 71 (1935).

[6] V. L. Ginzburg and L. D. Landau, Zh. Eksp. i Teor. Fiz. (Rus.) **20**, 1064 (1950).

[7] J. Bardeen, L. Cooper, and R. Schriffer, *Phys.Rev.* **108**, 1175 (1957).

[8] A. A. Abrikosov, Zh. Eksp. i Teor. Fiz. (Rus.) **32**, 1442 (1957).

[9] J. G. Bednirz and A. Z. Muller, *Physik B* **64**, 189 (1986).

[10] J. Nagamatsu, N. Nakagawa, T. Muranaka, Y. Zenitani, and J. Akimitsu, *Nature* **410**, 63 (2001).

[11] X. H. Chen, T. Wu, G. Wu, R. H. Liu, H. Chen, and D. F. Fang, *Nature* **453**, 761 (2008).

[12] http://www.superconductors.org.

[13] E. A. Bretz, Superconductors on the high seas, *IEEE Spectrum* **41**, 52 (2004).

[14] G. B. Lubkin, *Phys. Today* **49**, 48 (1996).

[15] http://www.zenergypower.com (Zenergy Power).

[16] V. Braccini, D. Nardelli, R. Penco, and G. Grasso, *Physica C* **456**, 209 (2007).

[17] http://www.oxinst.com (OXFORD Instruments).

[18] J. Clark (ed.)., "The SQUID Handbook", Wiley-VCH, (2004).

[19] http://www.iter.org.

[20] M. Jones and R. Marsh, *Journal of American Chemical Society* **76**, 1434 (1954).

[21] O. F. de Lima, R. A. Ribeiro, M. A. Avila, C. A. Cardoso, and A. A. Coelho, *Phys. Rev. Lett.* **86**, 5974 (2001).

[22] H. Suhl, B. T. Matthias, and L. R. Walker, *Phys. Rev. Lett.* **3**, 552 (1959).

[23] H. J. Choi, D. Roundy, H. Sun, M. L. Cohen, and S. G. Louie, *Nature* **418**, 758 (2002).

[24] Y. Iwasa, D. C. Larbalestier, M. Okada, R. Penco, M. D. Sumption, and X. Xi, *IEEE Trans. Appl. Supercond.* **16**, 1457 (2006).

[25] C. Buzea and T. Yamashita, *Supercond. Sci. Technol.* **14**, R115-R146 (2001).

[26] J. Kortus, I. I. Mazin, K. D. Belashchenko, V. P. Antropov, and L. L. Boyer, *Phys. Rev. Lett.* **86**, 4656 (2001).

[27] X. X. Xi, *Rep. Prog. Phys.* **71**, 116501 (2008).

[28] D. Tzeli and A. Mavridis, *J. Phys. Chem. A* **109**, 10663 (2005).

[29] L. Ivanovskii, *Phys. Solid State* **45**, 1829 (2003).

[30] K. Vinod, Neson Varghese and U. Syamaprasad, *Supercond. Sci. Technol.* **20**, R31-R45 (2007).

[31] P. Szabo, P. Samuely, J. Kacmarcik, T. Klein, J. Marcus, D. Fruchart, S. Miraglia, C. Marcenat, and A. G. M. Jansen, *Phys. Rev. Lett.* **87**, 137005 (2001).

[32] H. Schmidt, J. F. Zasadzinski, K. E. Gray, and D. G. Hinks, *Phys. Rev. Lett.* **88**, 127002 (2002).

[33] R. S. Gonnelli, D. Daghero, G. A. Ummarino, V. A. Stepanov, J. Jun, S. M. Kazakov, and J. Karpinski, *Phys. Rev. Lett.* **89**, 247004 (2002).

[34] W. K. Park and L. H. Greene, *Rev. Sci. Instrum.* **77**, 023905 (2006).

[35] M. Iavarone, G. Karapetrov, A. E. Koshelev, W. K. Kwok, G. W. Crabtree, D. G. Hinks, W. N. Kang, Eun-Mi Choi, Hyun Jung Kim, Hyeong-Jin Kim, and S. I. Lee, *Phys. Rev. Lett.* **89**, 187002 (2002).

[36] F. Giubileo, D. Roditchev, W. Sacks, R. Lamy, D. X. Thanh, and J. Klein, S. Miraglia, D. Fruchart, and J. Marcus, and Ph. Monod, *Phys. Rev. Lett.* **87**, 177008 (2001).

[37] M, R. Eskildsen, M. Kugler, S. Tanaka, J. Jun, S. Kazakov, J. Karpinski, and O. Fischer, *Phys. Rev. Lett.* **89**, 187003 (2002).

[38] X. K. Chen, M. J. Konstantinovic, J. C. Irwin, D. D. Lawrie, and J. P. Franck, *Phys. Rev. Lett.* **87**, 157002 (2001).

[39] S. Tsuda, T. Yokoya, T. Kiss, Y. Takano, K. Togano, H. Kito, H. Ihara, and S. Shin, *Phys. Rev. Lett.* **87**, 177006 (2001).

[40] S. Souma, Y. Machida, T. Sato, T. Takahashi, H. Matsui, S.-C. Wang, H. Ding, A. Kaminski, J. C. Campuzano, S. Sasaki, and K. Kadowaki, *Nature* **423**, 65 (2002).

[41] S. Tsuda, T. Yokoya, Y. Takano, H. Kito, A. Matsushita, F. Yin, J. Itoh, H. Harima, and S. Shin, *Phys. Rev. Lett.* **91**, 127001 (2003).

[42] J.P. Franck, in "Physical properties of high temperature superconductors IV", Ginsberg (Ed.), *World Scientific: Singapore*, 189 (1994).

[43] R. Kishore, in "Studies of high temperature superconductors", A. Narlikar (Ed), *Nova Scientific Publishers: Commack, NY*, 23 (1999).

[44] S. L. Bud'ko, G. Lapertot, C. Petrovic, C. E. Cunningham, N. Anderson, and P. C. Canfield, *Phys. Rev. Lett.* **86**, 1877 (2001).

[45] D. G. Hinks, H. Claus and J. D. Jorgensen, *Nature* **411**, 457 (2001).

[46] T. Takahashi, T. Sato, S. Souma, T. Muranaka, and J. Akimitsu, *Phys. Rev. Lett.* **86**, 4915 (2001).

[47] G. Karapetrov, M. Iavarone, W. K. Kwok, G. W. Crabtree, and D. G. Hinks, *Phys. Rev. Lett.* **86**, 4374 (2001).

[48] R. Osborn, E. A. Goremychkin, A. I. Kolesnikov, and D. G. Hinks, *Phys. Rev. Lett.* **87**, 017005 (2001).

[49] E. F. Skelton, D. U. Gubser, J. O. Willis, R. A. Hein, S. C. Yu, I. L. Spain, R. M. Waterstrat, and A. R. Sweedler, *Phys. Rev. B* **20**, 4538 (1979).

[50] S. Deemyad, T. Tomita, J. J. Hamlin, B. R. Beckett, J. S. Schilling, D. G. Hinks, J. D. Jorgensen, S. Lee, and S. Tajima, *Physica C* **385**, 105 (2003).

[51] M. Monteverde, M. N. Regueiro, N. Rogado, K. A . Regan, M. A. Hayward, T. He, S. M. Loureiro, and R. J. Cava, *Science* **292**, 75 (2001).

[52] P. Bordet, M. Mezouar, M. Nunez-Regueiro, M. Monteverde, M. D. Nunez-Regueiro, N. Rogado, K. A. Regan, M. A. Hayward, T. He, S. M. Loureiro, and R. J. Cava, *Phys. Rev. B* **64**, 172502 (2001).

[53] I. Loa and K. Syassen, *Solid State Commun.* **118**, 279 (2001).

[54] R. Ma, M. Liu, Y. G. Wang, and Y. H. Yang, *Phys. Status Solidi* b **244**, 1082 (2007).

[55] Prabhakar P. Singh, *Phys. Rev. Lett.* **97**, 247002 (2006).

[56] R. H. T.Wilke, S. L. Bud'ko, P. C. Canfield, J. Farmer, and S. T. Hannahs, *Phys. Rev. B* **73**, 134512 (2006).

[57] R. Gandikota, R. K. Singh, J. Kim, B. Wilkens, N. Newman, J. M. Rowell, A. V. Pogrebnyakov, X. X. Xi, J. M. Redwing, S. Y. Xu, and Q. Li, *Appl. Phys. Lett.* **86**, 012508 (2005).

[58] M. Putti, M. Affronte, C. Ferdeghini, P. Manfrinetti, C. Tarantini, and E. Lehmann, *Phys. Rev. Lett.* **96**, 077003 (2006).

[59] A. Serquis, L. Civale, D. L. Hammon, X. Z. Liao, J. Y. Coulter, Y. T. Zhu, M. Jaime, D. E. Peterson, F. M. Mueller, V. F. Nesterenko, and Y. Gu, *Appl. Phys. Lett.* **82**, 2847 (2003).

[60] J. H. Kim, S. X. Dou, J. L. Wang, D. Q. Shi, X. Xu, M. S. A. Hossain, W. K. Yeoh, S. Choi, and T. Kiyoshi, *Supercond. Sci. Technol.* **20**, 448 (2007).

[61] H. Kumakura, A. Matsumoto, T. Nakane, and H. Kitaguchi, *Physica C* **456**, 196 (2007).

[62] X. H. Zeng, A. V. Pogrebnyakov, M. H. Zhu, J. E. Jones, X. X. Xi, S. Y. Xu, E. Wertz, Qi Li, J. M. Redwing, J. Lettieri, V. Vaithyanathan, D. G. Schlom, Z.-K. Liu, O. Trithaveesak, and J. Schubert, *Appl. Phys. Lett.* **82**, 2097 (2003).

[63] W. Pickett, *Nature* **418**, 733 (2002).

[64] K. Vinod, R. G. Abhilash Kumar and U. Syamaprasad, *Supercond. Sci. Technol.* **20**, R1-R13 (2007).

[65] A. Matsumoto, H. Kumakura, H. Kitaguchi, H. Fujii, and K. Togano, *Physica C* **382**, 207 (2002).

[66] D. C. Larbalestier, L. D. Cooley, M. O. Rikel, A. A. Polyanskii, J. Jiang, S. Patnaik, X. Y. Cai, D. M. Feldmann, A. Gurevich, A. A. Squitieri, M. T. Naus, C. B. Eom, E. E. Hellstrom, R. J. Cava, K. A. Regan, N. Rogado, M. A. Hayward, T. He, J. S. Slusky, P. Khalifah, K. Inumaru, and M. Haas, *Nature* **410**, 186 (2001).

[67] Ekin. J. W., A. I. Braginski, A. J. Panson, M. A. Janocko, D. W. Capone II, N. J. Zaluzec, B. Flandermeyer. d.L.O. F., M. Hong. J. Kwo, and S.H. Liou, *J. Appl. Phys.* **62**, 4821 (1987).

[68] Mannhart, J., P. Chaudhari, D. Dimos, C. C. Tsuei, and T. R. McGuire, *Phys. Rev. Lett.* **61**, 2476 (1998).

[69] K.H.P. Kim, W. N. Kang, M.-S. Kim, C. U. Jung, H.-J. Kim, E.-M. Choi, M.-S. Park, and S.-I. Lee, cond-mat 0103176 (2001).

[70] E. W. Collings, M. D. Sumption, M. Bhatia, M. A. Susner, and S. D. Bohnenstiehl, *Supercond. Sci. Technol.* **21**, 103001 (2008).

[71] A. V. Pan, S. Zhou, H. Liu, and S. Dou, *Supercond. Sci. Technol.* **16**, 639 (2003).

[72] R. F. Klie, J. C. Idrobo, N. D. Browning, A. Serquis, Y. T. Zhu, X. Z. Liao, and F. M. Mueller, *Appl. Phys. Lett.* **80**, 3970 (2002).

[73] X. Z. Liao, A. Serquis, Y. T. Zhu, J. Y. Huang, L. Civale, D. E. Peterson, F. M. Mueller, H. F. Xu, *J. Appl. Phys.* **93**, 6208 (2003).

[74] J. Jiang, B. J. Senkowicz, D. C. Larbalestier, and E. E. Hellstrom, *Supercond. Sci. Technol.* **19**, L33 (2006).

[75] J. M. Rowell, *Supercond. Sci. Technol.* **16**, R17 (2003).

[76] J. M. Rowell, S. Y. Xu, X. H. Zeng, A. V. Pogrebnyakov, Q. Li, X. X. Xi, J. M. Redwig, W. Tian, and X. Pan, *Appl. Phys. Lett.* **83**, 102 (2003).

[77] P. C. Canfield, D. K. Finnemore, S. L. Bud'ko, J. E. Ostenson, G. Lapertot, C. E. Cunningham, and C. Petrovic, *Phys. Rev. Lett.* **86**, 2423 (2001).

[78] D. Dew-Hughes, *Phil. Mag.* **30**, 293 (1974).

[79] A. M. Campbell and J. E. Evetts, "Critical Currents in Superconductors", London: Taylor and Francis (1972).

[80] E. W. Collings, "Applied Superconductivity Metallurgy and Physics of Titanium Alloys", Vol. 2, New York: Plenum (1986).

[81] P. Kovac, I. Husek, T. Melisek, J. C. Grivel, W. Pachla, V. Strbik, R. Diduszko, J. Homeyer, and N. H. Andersen, *Supercond. Sci. Technol.* **17**, L41 (2004).

[82] A. Serquis, X. Z. Liao, Y. T. Zhu, J. Y. Coulter, J. Y. Huang, J. O. Willis, D. E. Peterson, F. M. Mueller, N. O. Moreno, J. D. Thompson, V. F. Nesterenko, and S. S. Indrakanti, *J. Appl. Phys.* **92**, 351 (2002).

[83] J. Chen, V. Ferrando, P. Orgiani, A. V. Pogrebnyakov, R. H. T. Wilke, J. B. Betts, C. H. Mielke, J. M. Redwing, X. X. Xi, and Qi Li, *Phys. Rev. B* **74**, 174511 (2006).

[84] H. Kitaguchi, A. Matsumoto, H. Kumakura, T. Doi, H. Yamamoto, K. Saitoh, H. Sosiati, and S. Hata, *Appl. Phys. Lett.* **85**, 2842 (2004).

[85] H. Kitaguchi and T. Doi, *Supercond. Sci. Technol.* **18**, 489 (2005).

[86] H. Sosiati, S. Hata, N. Kuwano, Y. Tomokiyo, H. Kitaguchi, T. Doi, H. Yamamoto, A. Matsumoto, K. Saitoh, and H. Kumakura, *Supercond. Sci. Technol.* **18**, 1275 (2005).

[87] H. Jin, H.-H. Wen, H.-P. Yang, Z.-Y. Liu, Z.-A. Ren, G.-C. Che, and Z.-X. Zhao, *Appl. Phys. Lett.* **83**, 2626 (2003).

[88] S. X. Dou, A. V. Pan, S. Zhou, M. Ionescu, X. L. Wang, J. Horvat, H. K. Liu, and P. R. Munroe, *J. Appl. Phys.* **94**, 1850 (2003).

[89] Xu. M, H. Kitazawa, Y. Takano, J. Ye, K. Nishida, H. Abe, A. Matsushita, N. Tsuji,i and G. Kido, *Appl. Phys. Lett.* **79**, 2779 (2001).

[90] A. D. Caplin, Y. Bugoslavsky, L. F. Cohen, L. Cowey, J. Driscoll, J. Moore, and G. K. Perkins, *Supercond. Sci. Technol.* **16**, 176 (2003).

[91] L. Lyard, P. Szabo, T. Klein, J. Marcus, C. Marcenat, K. H. Kim, B. W. Kang, H.-S. Lee, and S.-I. Lee, *Phys. Rev. Lett.* **92**, 057001 (2004).

[92] U. Welp, A. Rydh, G. Karapetrov, W. K. Kwok, G. W. Crabtree, C. Marcenat, L. M. Paulius, L. Lyard, T. Klein, J. Marcus, S. Blanchard, P. Samuely,

P. Szabo, A. G. M. Jansen, K. H. P. Kim, C. U. Jung, H. -S. Lee, B. Kang, and S. -I. Lee, *Physica C* **385**, 154 (2003).

[93] A. Gurevich, *Phys. Rev. B* **67**, 184515 (2003).

[94] M. Angst, R. Puzniak, A. Wisniewski, J. Jun, S. M. Kazakov, J. Karpinski, J. Roos, and H. Keller, *Phys. Rev. Lett.* **88**, 167004 (2002).

[95] J. Karpinski, M. Angst, J. Jun, S. M. Kazakov, R. Puzniak, A. Wisniewski, J. Roos, H. Keller, A. Perucchi, L. Degiorgi, M. R. Eskildsen, P. Bordet, L. Vinnikov, and A. Mironov, *Supercond. Sci. Technol.* **16**, 221 (2003).

[96] H. S. Lee, K. H. P. Kim, J. H. Choi, C. U. Jung, P. Chowdhury, S. Choi, and S. I. Lee, *J. Low Temp. Phys.* **131**, 1117 (2003).

[97] A. Gurevich, *Physica C* **456**, 160 (2007).

[98] N. R. Werthamer, E. Helfand, and P. C. Hohenberg, *Phys. Rev.* **147**, 295 (1966).

[99] V. Braccini, A. Gurevich, J. E. Giencke, M. C. Jewell, C. B. Eom, D. C. Larbalestier, A. Pogrebnyakov, Y. Cui, B. T. Liu, Y. F. Hu, J. M. Redwing, Qi Li, X. X. Xi, R. K. Singh, R. Gandikota, J. Kim, B. Wilkens, N. Newman, J. Rowell, B. Moeckly, V. Ferrando, C. Tarantini, D. Marre, M. Putti, C. Ferdeghini, R. Vaglio, and E. Haanappel, *Phys. Rev. B* **71**, 012504 (2005).

[100] P. C. Canfield, S. L. Bud'ko, and D. K. Finnemore, *Physica C* **385**, 1 (2003).

[101] A. Carrington and F. Manzano, *Physica C* **385**, 205 (2003).

[102] S. L. Bud'ko, C. Petrovic, G. Lapertot, C. E. Cunningham, P. C. Canfield, M. H. Jung, and A. H. Lacerda, *Phys. Rev. B* **63**, 220503 (2001).

[103] S. X. Dou, O. Shcherbakova, W. K. Yeoh, J. H. Kim, S. Soltanian, X. L. Wang, C. Senatore, R. Flukiger, M. Dhalle, O. Husnjak, and E. Babic, *Phys. Rev. Lett.* **98**, 097002 (2007).

[104] J. S. Slusky, N. Rogado, K. A. Regan, M. A. Haywart, P. Khalifah, T. He, K. Inumaru, S. M. Loureiro, M. K. Haas, H. W. Zandbergen, and R. J. Cava, *Nature* **410**, 343 (2001).

[105] J. Kortus, *Physica C* **456**, 54 (2007).

[106] R. S. Gonnelli, D. Daghero, G. A. Ummarino, M. Tortello, D. Delaude, V. A. Stepanov, and J. Karpinski, *Physica C* **456**, 134 (2007).

[107] P. Samuely, P. Szabo, Z. Pribulova, M. Angst, S.L. Bud'ko, P.C. Canfield, T. Klein, L. Lyard, J. Marcus, C. Marcenat, B.W. Kang, H.-J. Kim, H.-S. Lee, H.-K. Lee, and S.I. Lee, *Physica C* **460**, 84 (2007).

[108] M. Angst, S. L. Bud'ko, R. H. T. Wilke, and P. C. Canfield, *Phys. Rev. B* **71**, 144512 (2005).

[109] J. Karpiski, N. D. Zhigadlo, S. Katrych, R. Puzniak, K. Rogacki, and R. Gonnelli, *Physica C* **456**, 3 (2007).

[110] M. Monni, C. Ferdeghini, M. Putti, P. Manfrinetti, A. Palenzona, M. Affronte, P. Postorino, M. Lavagnini, A. Sacchetti, D. Di Castro, F. Sacchetti, C. Petrillo, and A. Orecchini, *Phys. Rev. B* **73**, 214508 (2006).

[111] F. Bernardini and S. Massidda, *Phys. Rev. B* **74**, 014513 (2006).

[112] K. Rogacki, B. Batlogg, J. Karpinski, N. D. Zhigadlo, G. Schuck, S. M. Kazakov, P. Wagli, R. Puzniak, A. Wisniewski, F. Carbone, A. Brinkman, and D. van der Marel, *Phys. Rev. B* **73**, 174520 (2006).

[113] R. S. Gonnelli, D. Daghero, A. Calzolari, G. A. Ummarino, V. Dellarocca, V. A. Stepanov, S. M. Kazakov, N. Zhigadlo and J. Karpinski, *Phys. Rev. B* **71**, 060503 (2005).

[114] P. Szabo, P. Samuely, Z. Pribulova, M. Angst, S. Bud'ko, P. C. Canfield and J. Marcus, *Phys. Rev. B* **75**, 144507 (2007).

[115] S. Tsuda, T. Yokoya, T. Kiss, T. Shimojima, S. Shin, T. Togashi, S. Watanabe, C. Zhang, C. T. Chen, S. Lee, H. Uchiyama, S. Tajima, N. Nakai, and K. Machida, *Phys. Rev. B* **72**, 064527 (2005).

[116] S. Tsuda, T. Yokoya and S. Shin, *Physica C* **456**, 126 (2007).

[117] M. Avdeev, J. D. Jorgensen, R. A. Ribeiro, S. L. Bud'ko, and P. C. Canfield, *Physica C* **387**, 301 (2003).

[118] S. X. Dou, A. V. Pan, S. Zhou, M. Ionescu, H. K. Liu, and P. R. Munroe, *Supercond. Sci. Technol.* **15**, 1587 (2002).

[119] S. Hata, T. Yoshidome, H. Sosiati, Y. Tomokiyo, N. Kuwano, A. Matsumoto, H. Kitaguchi, and H. Kumakura, *Supercond. Sci. Technol.* **19**, 161 (2006).

[120] S. X. Dou, V. Braccini, S. Soltanian, R. Klie, Y. Zhu, S. Li, X. L. Wang, and D. Larbalestier, *J. Appl. Phys.* **96**, 7549 (2004).

[121] W. K. Yeoh, J. H. Kim, J. Horvat, X. Xu, M. J. Qin, S. X. Dou, C. H. Jiang, T. Nakane, H. Kumakura, and P. Munroe, *Supercond. Sci. Technol.* **19**, 596 (2006).

[122] Y. Ma, X. Zhang, G. Nishijima, K. Watanabe, S. Awaji, X. Bai, *Appl. Phys. Lett.* **88**, 072502 (2006).

[123] A. V. Pogrebnyakov, X. X. Xi, J. M. Redwing, V. Vaithyanathan, D. G. Schlom, A. Soukiassian, S. B. Mi, C. L. Jia, J. E. Giencke, C. B. Eom, J. Chen, Y. F. Hu, Y. Cui, and Q. Li, *Appl. Phys. Lett.* **85**, 2017 (2004).

[124] M. D. Sumption, M. Bhatia, S. X. Dou, M. Rindfliesch, M. Tomsic, L. Arda, M. Ozdemir, Y. Hascicek, and E. W. Collings, *Supercond. Sci. Technol.* **17**, 1180 (2004).

[125] M. A. Susner, M. D. Sumption, M. Bhatia, X. Peng, M. J. Tomsic, M. A. Rindfleisch, and E. W. Collings, *Physica C* **456**, 180 (2007).

[126] Z. Gao, Y. Ma, X. Zhang, D. Wang, Z. Yu, H. Yang, H. Wen, and E. Mossang, *J. Appl. Phys.* **102**, 013914 (2007).

[127] J. H. Kim, W. K. Yeoh, M. J. Qin, X. Xu, S. X. Dou, P. Munroe, H. Kumakura, T. Nakane, and C. H. Jiang, *Appl. Phys. Lett.* **89**, 122510 (2006).

[128] W.X. Li, Y. Li, R.H. Chen, W.K. Yoeh, and S.X. Dou, *Physica C* **460-462**, 570 (2007).

[129] Y. Zhao, Y. Yang, C.H. Cheng, and Y. Zhang, *Physica C* **463-465**, 165 (2007).

[130] Y. Zhao, C. H. Cheng, X. F. Rui, H. Zhang, P. Munroe, H. M. Zeng, N. Koshizuka, and M. Murakami, *Appl. Phys. Lett.* **83**, 2916 (2003).

[131] C. H. Cheng, H. Zhang, Y. Zhao, Y. Feng, X. F. Rui, P. Munroe, H. M. Zeng, N. Koshizuka, and M. Murakami, *Supercond. Sci. Technol.* **16**, 1182 (2003).

[132] A. Yamamoto, J. Shimoyama, I. Iwayama, Y. Katsura, S. Horii, and K. Kishio, *Physica C* **463-465**, 807 (2007).

[133] S. X. Dou, S. Soltanian, J. Horvat, X. L. Wang, S. H. Zhou, M. Ionescu, H. K. Liu, P. Munroe, and M. Tomsic, *Appl. Phys. Lett.* **81**, 3419 (2002).

[134] A. Matsumoto, H. Kumakura, H. Kitaguchi, and H. Hatakeyama, *Supercond. Sci. Technol.* **16**, 926 (2003).

[135] A. Yamamoto, J. Shimoyama, S. Ueda, I. Iwayama, S. Horii, and K. Kishio, *Supercond. Sci. Technol.* **18**, 1323 (2005).

[136] R. Flukiger, P. Lezza, M. Cesaretti, C. Senatore, and R. Gladyshevskii, *IEEE Trans. Appl. Supercond.* **17**, 2846 (2007).

[137] S. Ueda, J. Shimoyama, A. Yamamoto, S. Horii, and K. Kishio, *Supercond. Sci. Technol.* **17**, 926 (2004).

[138] R. M. Scanlan, A. P. Malozemoff, and D. C. Larbalestier, *IEEE Proc.* **92**, 1639 (2004).

[139] M. Herrmann, W. Haessler, C. Rodig, W. Gruner, B. Holzapfel, and L. Schultz, *Appl. Phys. Lett.* **91**, 082507 (2007).

[140] R. H. T. Wilke, S. L. Bud'ko, P. C. Canfield, D. K. Finnemore, R. J. Suplinskas, and S. T. Hannahs, *Phys. Rev. Lett.* **92**, 217003 (2004).

[141] A. Serquis, G. Serrano, S. M. Moreno, L. Civale, B. Maiorov, F. Balakirev, and M. Jaime, *Supercond. Sci. Technol.* **20**, L12 (2007).

[142] S. X. Dou, W. K. Yeoh, O. Shcherbakova, J. Horvat, J. H. Kim, A. V. Pan, D. Wexler, Y. Li, W. X. Li, Z. M. Ren, P. Munroe, and J. Z. Cui, *Appl. Phys Lett.* **89**, 202504 (2006).

[143] P. Lezza, C. Senatore, and R. Flukiger, *Supercond. Sci. Technol.* **19**, 1030 (2006).

[144] M. Bhatia, M. D. Sumption, E. W. Collings, *IEEE Trans. Appl. Supercond.* **15**, 3204 (2005).

[145] A. Matsumoto, H. Kumakura, H. Kitaguchi, B. J. Senkowicz, M. C. Jewell, E. E. Hellstrom, Y. Zhu, P. M. Voyles, and D. C. Larbalestier, *Appl. Phys. Lett.* **89**, 132508 (2006).

[146] S. Zhou, A. V. Pan, D. Wexler, and S. X. Dou, *Adv. Mater.* **19**, 1373 (2007).

[147] O. V. Shcherbakova, A. V. Pan, J. L. Wang, A. V. Shcherbakov, S. X. Dou, D. Wexler, E. Babic, M. Jercinovic, and O. Husnjak, *Supercond. Sci. Technol.* **21**, 015005 (2008).

[148] J. H. Kim, S. Zhou, M. S. A. Hossain, A. V. Pan, and S. X. Dou, *Appl. Phys. Lett.* **89**, 142505

[149] O. V. Shcherbakova, A. V. Pan, S. X. Dou, R. Nigam, and D. Wexler, *J. Appl. Phys* **107**, 09E147 (2010).

[150] O. V. Shcherbakova, A. V. Pan, D. Wexler, and S. X. Dou, *IEEE Trans. Appl. Supercond.* **17**, 2790 (2007).

[151] H. L. Xu et al, *Supercond. Sci. Technol.* **19**, 68 (2006).

[152] M. S. A. Hossain, J. H. Kim, X. L. Wang, X. Xu, G. Peleckis, and S. X. Dou, *Supercond. Sci. Technol.* **20**, 112 (2007).

[153] D. K. Finnemore, W. E. Straszheim, S. L. Bud'ko, P. C. Canfield, N. E. Jr. Anderson, and R. J. Suplinskas, *Physica C* **385**, 278 (2003).

[154] S. Haigh, P. Kovac, T. A. Prikhna, Ya. M. Savchuk, M. R. Kilburn, C. Salter, J. Hutchison, and C. Grovenor, *Supercond. Sci. Technol.* **18**, 1190 (2005).

[155] T. A. Prikhna, W. Gawalek, Ya. M. Savchuk, V. E. Moshchil, N. V. Sergienko, T. Habisreuther, M. Wendt, R. Hergt, Ch. Schmidt, J. Dellith, V. S. Melnikov, A. Assmann, D. Litzkendorf, and P. A. Nagorny, *Physica C* **402**, 223 (2003).

[156] N. Horhager, M. Eisterer, H. W. Weber, T. Prikhna, T. Tajima, and V. F. Nesterenko, *J. Phys. Conf. Ser.* **43**, 500 (2006).

[157] T. A. Prikhna, W. Gawalek, A. B. Surzhenko, V. E. Moshchil, N. V. Sergienko, Ya. M. Savchuk, V. S. Melnikov, P. A. Nagorny, T. Habisreuther, S. N. Dub, M. Wendt, D. Litzkendorf, J. Dellith, Ch. Schmidt, G. Krabbes, and A. V. Vlasenko, *Physica C* **372-376**, 1543 (2002).

[158] T. A. Prikhna, W. Gawalek, Ya. M. Savchuk, V. E. Moshchil, N. V. Sergienko, A. B. Surzhenko, M. Wendt, S. N. Dub, V. S. Melnikov, Ch. Schmidt, and P. A. Nagorny, *Physica C* **386**, 565 (2003).

[159] Y. Zhao, Y. Feng, C. H. Cheng, L. Zhou, Y. Wu, T. Machi, Y. Fudamoto, N. Koshizuka, and M. Murakami, *Appl. Phys. Lett.* **79**, 1154 (2001).

[160] S. K. Chen, M. Wei and J. L. MacManus-Driscoll, *Appl. Phys. Lett.* **88**, 192512 (2006).

[161] Y. Feng, Y. Zhao, A. K. Pradhan, C. H. Cheng, J. K. F. Yau, L. Zhou, N. Koshizuka and M. Murakami, *J. Appl. Phys.* **92**, 2614 (2002).

[162] J. Wang, Y. Bugoslavsky, A. Berenov, L. Cowey, A. D. Caplin, L. F. Cohen, J. L. MacManus Driscoll, L. D. Cooley, X. Song, and D. C. Larbalestier, *Appl. Phys. Lett.* **81**, 2026 (2002).

[163] A. Snezhko, T. Prozorov and R. Prozorov, *Phys. Rev. B* **71**, 024527 (2005).

[164] J. D. DeFouw and D. C. Dunand, *Appl. Phys. Lett.* **83**, 120 (2003).

[165] G. Giunchi, S. Ceresara, G. Ripamonti, A. Di Zenobio, S. Rossi, S. Chiarelli, M. Spadoni, R. Wesche, P.L. Bruzzone, *Supercond. Sci. Technol.* **16**, 285 (2003).

[166] C. Chen, Z. Zhou, X. Li, J. Xu, Y. Wang, Z. Gao, and Q. Feng, *Solid State Commun.* **131**, 275 (2004).

[167] W. Goldacker, S. I. Schlachter, B. Liu, B. Obst, and E. Klimenko, *Physica C* **401**, 80 (2004).

[168] W. Habler, B. Birajdar, W. Gruner, M. Herrmann, O. Perner, C. Rodig, M. Schubert, B. Holzapfel, O. Eibl, and L. Schultz, *Supercond. Sci. Technol.* **19**, 512 (2006).

[169] R. A. Ribeiro, S. L. Bud'ko, C. Petrovic, and P. C. Canfield, *Physica C* **385**, 16 (2003).

[170] X. Xu, M. J. Qin, K. Konstantinov, D. I. dos Santos, W. K. Yeoh, J. H. Kim, and S. X. Dou, *Supercond. Sci. Technol.* **19**, 466 (2006).

[171] S. Zhou, A. V. Pan, J. Horvat, M. J. Qin, H. K. Liu, and S. X. Dou, *Supercond. Sci. Technol.* **17**, S528 (2004).

[172] C. H. Jiang, H. Hatakeyama, and H. Kumakura, *Supercond. Sci. Technol.* **18**, L17 (2005).

[173] H. Fujii, K. Togano, and H. Kumakura, *Supercond. Sci. Technol.* **15**, 1571 (2002).

[174] C. H. Jiang, T. Nakane, H. Hatakeyama, and H. Kumakura, *Physica C* **422**, 127 (2005).

[175] C. H. Jiang, H. Hatakeyama, and H. Kumakura, *Physica C* **423**, 45 (2005).

[176] R. Zeng, L. Lu, J. L. Wang, J. Horvat, W. X. Li, D. Q. Shi, S. X. Dou, M. Tomsic, and M. Rindfleisch, *Supercond Sci. Technol.* **20**, L43 (2007).

[177] Y. Takano, H. Takeya, H. Fujii, H. Kumakura, T. Hatano, K. Togano, H. Kito, and H. Ihara, *Appl. Phys. Lett.* **78**, 2914 (2001).

[178] B. A. Glowacki, M. Majoros, M. Vickers, J. E. Evetts, Y. Shi, and I. McDougall, *Supercond. Sci. Technol.* **14**, 193 (2001).

[179] C. Fischer, W. Habler, C. Rodig, O. Perner, G. Behr, M. Schubert, K. Nenkov, J. Eckert, B. Holzapfel, and L. Schultz, *Physica C* **406**, 121 (2004).

[180] H. L. Suo, P. Lezza, D. Uglietti, C. Beneduce, V. Abacherli, and R. Flukiger, *IEEE Trans. Appl. Supercond.* **13**, 3265 (2003).

[181] N. A. Frederick, S. Li, M. B. Maple, V. F. Nesterenko, and S. S. Indrakanti, *Physica C* **363**, 1 (2001).

[182] T. C. Shields, K. Kawano, D. Holdom, and J. S. Abell, *Supercond. Sci. Technol.* **15**, 202 (2002).

[183] X. Z. Liao, A. Serquis, Y. T. Zhu, L. Civale, D. L. Hammon, D. E. Peterson, F. M. Mueller, V. F. Nesterenko, and Y. Gu, *Supercond. Sci. Technol.* **16**, 799 (2003).

[184] R. Flukiger, M. S. A. Hossain and C. Senatore, *Supercond. Sci. Technol.* **22**, 085002 (2009).

[185] M. Bhatia, M. D. Sumption, M. Tomsic, and E. W. Collings, *Physica C* **407**, 153 (2004).

[186] S.I. Schlachter, A. Frank, B. Ringsdorf, H. Orschulko, B. Obst, B. Liu, and W. Goldacker, *Physica C* **445-448**, 777 (2006).

[187] S. K. Chen, K. A. Yates, M. G. Blamire, and J. L. MacManus-Driscoll, *Supercond. Sci. Technol.* **18**, 1473 (2005).

[188] D. Wang, Y. Ma, Z. Yu, Z. Gao, X. Zhang, K. Watanabe and E. Mossang, *Supercond. Sci. Technol.* **20**, 574 (2007).

[189] H. Yamada, M. Hirakawa, H. Kumakura, and H. Kitaguchi, *Supercond. Sci. Technol.* **19**, 175 (2006).

[190] P. Kovac, I. Husek, V. Skakalova, J. Meyer, E. Dobrocka, M. Hirscher, and S. Roth, *Supercond. Sci. Technol.* **20**, 105 (2007).

[191] W. Pachla, A. Morawski, P. Kovac, I. Husek, A. Mazur, T. Lada, R. Diduszko, T. Melisek, V. Strbik, and M. Kulczyk, *Supercond. Sci. Technol.* **19**, 1 (2006).

[192] P. Kovac, B. Birajdar, I. Husek, T. Holubek, and O. Eibl, *Supercond. Sci. Technol.* **21**, 045011 (2008).

[193] M. Tomsic, M. Rindfleisch, J. Yue, K. McFadden, D. Doll, J. Phillips, M. D. Sumption, M. Bhatia, S. Bohnenstiehl, and E. W. Collings, *Physica C* **456**, 203 (2007).

[194] S. Jin, H. Mavoori, C. Bower, and R. B. van Dover, *Nature* **411**, 563 (2001).

[195] G. Grasso, A. Malagoli, C. Ferdeghini, S. Roncallo, V. Braccini, and A. S. Siri, *Appl. Phys. Lett.* **79**, 230 (2001).

[196] S. Soltanian, X. L. Wang, I. Kusevic, E. Babic, A. H. Li, M. J. Qin, J. Horvat, H. K. Liu, E. W. Collings, E. Lee, M. D. Sumption, and S. X. Dou, *Physica C* **361**, 84 (2001).

[197] H. Kitaguchi, A. Matsumoto, H. Hatakeyama, and H. Kumakura, *Supercond. Sci. Technol.* **17**, S486 (2004).

[198] K. Yamamoto, K. Osamura, S. Balamurugan, T. Nakamura, T. Hoshino, and I. Muta, *Supercond. Sci. Technol.* **16**, 1052 (2003).

[199] A. Serquis, L. Civale, D. L. Hammon, J. Y. Coulter, X. Z. Liao, Y. T. Zhu, D. E. Peterson, and F. M. Mueller, *Appl. Phys. Lett.* **82**, 1754 (2003).

[200] W. Goldacker, S. I. Schlachter, B. Obst, and M. Eisterer, *Supercond. Sci. Technol.* **17**, S490 (2004).

[201] Y. Feng, G. Yan, Y. Zhao, C. F. Liu, X. H. Liu, P. X. Zhang, L. Zhou, A. Sulpice, E. Mossang, and B. Hebral, *J. Phys.: Condens. Matter* **16**, 1803 (2004).

[202] H. Yamada, M. Hirakawa, H. Kumakura, A. Matsumoto, and H. Kitaguchi, *Appl. Phys. Lett.* **84**, 1728 (2004).

[203] E. W. Collings, E. Lee, M. D. Sumption, M. Tomsic, X. L. Wang, S. Soltanian, and S. X. Dou, *Physica C* **386**, 555 (2003).

[204] R. Flukiger, H. L. Suo, N. Musolino, C. Beneduce, P. Toulemonde, and P. Lezza, *Physica C* **385**, 286 (2003).

[205] H. Fang, Y. Y. Xue, Y. X. Zhou, A. Baikalov, and K. Salama, *Supercond. Sci. Technol.* **17**, L27 (2004).

[206] M. D. Sumption, M. Bhatia, M. Rindfleisch, M. Tomsic, and E. W. Collings, *Supercond. Sci. Technol.* **19**, 155 (2006).

[207] P. Kovac, I. Husek, T. Melisek, M. Kulich, and V. Strbik, *Supercond. Sci. Technol.* **19**, 600 (2006).

[208] H. Kitaguchi and H. Kumakura, *Supercond. Sci. Technol.* **18**, S284 (2005).

[209] C. R. M. Grovenor, L. Goodsir, C. J. Salter, P. Kovac and I. Husek, *Supercond. Sci. Technol.* **17**, 479 (2004).

[210] R. G. A. Kumar, K. Vinod, N. Varghese, and U. Syamaprasad, *Supercond. Sci. Technol.* **20**, 222 (2007).

[211] H. L. Suo, C. Beneduce, M. Dhalle, N. Musolino, J. Y. Genoud, and R. Flukiger, *Appl. Phys. Lett.* **79**, 3116 (2001).

[212] K.Tanaka, H. Kitaguchi, H. Kumakura, H. Yamada, M. Hirakawa, and M. Okada, *Supercond. Sci. Technol.* **18**, 678 (2005).

[213] R. Nast, S. I. Schlachter, S. Zimmer, H. Reiner, and W. Goldacker, *Physica C* **372**, 1241 (2002).

[214] H. Kumakura, A. Matsumoto, H. Fujii, and K. Togano, *Appl. Phys. Lett.* **79**, 2435 (2001).

[215] P. Kovac, I. Husek, W. Pachla, T. Melisek, R. Diduszko, K. Frohlich, A. Morawski, A. Presz, and D. Machajdik, *Supercond. Sci. Technol.* **15**, 1127 (2002).

[216] B. A. Glowacki, M. Majoros, M. Vickers, M. Eisterer, S. Toenies, H. W. Weber, M. Fukutomi, K. Komori, and K. Togano, *Supercond. Sci. Technol.* **16**, 297 (2003).

[217] M. W. Goldaker, S. I. Schlachter, J. Reiner, S. Zimmer, A. Nyilas, and H. Kiesel, *IEEE Trans. Appl. Supercond.* **13**, 3261 (2003).

[218] A. K. Pradhan, Y. Feng, Y. Zhao, N. Koshizuka, L. Zhou, P. X. Zhang, X. H. Liu, P. Ji, S. J. Du, and C. F. Liu, *Appl. Phys. Lett.* **79**, 1649 (2001).

[219] B. Q. Fu, Y. Feng, G. Yan, Y. Zhao, A. K. Pradhan, C. H. Cheng, P. Ji, X. H. Liu, C. F. Liu, L. Zhou, and K. F. Yau, *J. Appl. Phys.* **92**, 7341 (2002).

[220] W. Goldacker, S. I. Schlachter, S. Zimmer, and H. Reiner, *Supercond. Sci. Technol.* **14**, 787 (2001).

[221] W. Goldacker and S. I. Schlachter, *Physica C* **378**, 889 (2002).

[222] M. D. Sumption, M. Bhatia, F. Buta, S. Bohnenstiehl, M. Tomsic, M. Rindfleisch, J. Yue, J. Phillips, S. Kawabata, and E. W. Collings, *Supercond. Sci. Technol.* **18**, 961 (2005).

[223] J. H. Kim, W. K. Yeoh, M. J. Qin, X. Xu, and S. X. Dou, *J. Appl. Phys.* **100**, 013908 (2006).

[224] A. V. Pan and S. X. Dou, *J. Appl. Phys.* **96**, 1146 (2004).

[225] P. E. Kirkpatrick, J. W. Ekin, and S. L. Bray, *Rev. Sci. Instrum.* **70**, 3338 (1999).

[226] J. Royet, J. Scudiere, and R. Schwall, *IEEE Trans. Magn.* **19**, 761 (1983).

[227] E. Barzi, G. Ambrosio, N. Andreev, P. Bauer, D. Chichili, M. Fratini, L. Elementi, J. Hoffman, P. J. Limon, S. Mattafirri, J.-M. Rey, R. Yamada, and A. V. Zlobin, *IEEE Trans. Appl. Supercond.* **12**, 1009 (2002).

[228] B. Seeber, L.Erbuke, R.Flukiger, I. Horvath, and J. Neuenschwander, *IEEE Trans. Appl. Supercond.* **10**, 403 (2000).

[229] D. R. Lide (ed.).,"CRC Handbook of Chemistry and Physics", 82nd edition Boca Raton, FL: CRC Press (2001-2002).

[230] F.R Fickett, *Phys. Rev. B* **3**, 1941 (1971).

[231] http://www.columbussuperconductors.com

[232] http://www.hypertechresearch.com

[233] http://www.hitachi-cable.co.jp

[234] W. K. Yeoh and S. X. Dou, *Physica C* **456**, 170 (2007).

[235] G. Grasso, "Current state of ex-situ MgB_2 superconducting wire and their applications", talk at International Workshop on Electronic Materials and Their Applications, Institute for Superconducting and Electronic Materials, Wollongong (Australia), 19-20 March 2009.

[236] L. Cooley, A. Ghosh, and R. Scanlan, *Supercond. Sci. Technol.* **18**, R51-R65 (2005).

[237] O. Tsukamoto, *Cryogenics* **45**, 3-10 (2005).

[238] M. Majoros, L. Ye, A. M. Campbell, T. A. Coombs, A. V. Velichko, D. M. Astill, P. Sargent, M. Haslett, M. D. Sumption, E. W. Collings, M. Tomsic, S. Harrison, and M. Husband, *IEEE Trans. Appl. Supercond.* **17**, 1764 (2007).

[239] Ye Lin, M. Majoros, A. M. Campbell, T. Coombs, S. Harrison, P. Sargent, M. Haslett, and M. Husband, *IEEE Trans. Appl. Supercond.* **17**, 2826 (2007).

[240] M. Majoros, L. Ye, A. M. Campbell, T. A. Coombs, M. D. Sumption, and E. W. Collings, *IEEE Trans. Appl. Supercond.* **17**, 1803 (2007).

[241] M. Tomsic, M. Rindfleisch, J. Yue, K. McFadden, and J.Phillips, *Int. J. Appl. Ceram. Technol.* **4**, 250 (2007).

[242] M. Tomsic, M. Rindfleisch, J. Yue, T. Wieber, X. Peng, J. Phillips, D. Doll, and D. Lyons, "Superconductor Fabrication & Coil Issues Rotating Equipment - Rotors and Stators", talk at International Workshop on Electronic Materials and Their Applications, Institute for Superconducting and Electronic Materials, Wollongong (Australia), 19-20 March 2009.

[243] J. M. Cowley (ed.)., "Electron diffraction techniques", International Union of Crystallography; Oxford; New York; Oxford University Press (1992-1993).

[244] D. B. Williams and C. Barry Carter (ed.)., "Transmission electron microscope: a textbook for materials science", New York: Plenum Press (1996).

[245] C. P. Bean, *Rev. Mod. Phys.* **36**, 31 (1964).

[246] D. X. Chen, and R. B. Goldfarb, *J. Appl. Phys.* **66**, 2489 (1986).

[247] M. J. Qin, S. Keshavarzi, S. Soltanian, X. L. Wang, H. K. Liu, and S. X. Dou, *Phys. Rev. B* **69**, 012507 (2004).

[248] J. Horvat, S. Soltanian, X. L. Wang, and S. X. Dou, *Appl. Phys Lett.* **84**, 3109 (2004).

[249] A. Yamamoto, J. Shimoyama, S. Ueda, Y. Katsura, S. Horii, and K. Kishio, *Supercond. Sci. Technol.* **18**, 116 (2005).

[250] E. W. Collings, "Applied Superconductivity, Metallurgy and Physics of Titanium Alloys", New York: Plenum Press (1986).

[251] S. Soltanian, X. L. Wang, J. Horvat, S. X. Dou, M. D. Sumption, M. Bhatia, E. W. Collings, P. Munrie, and M. Tomsic, *Supercond. Sci. Technol.* **18**, 658 (2005).

[252] S. X. Dou, E. W. Collings, O. Shcherbakova, and A. Shcherbakov, *Supercond. Sci. Technol.* **19**, 333 (2006).

[253] J. M. Royet, J. D. Scudiere, and E. R. Schwall, *IEEE Trans. Magn.* **19**, 761 (1983).

[254] A. Yamamoto, *IEEE Trans. Appl. Supercond.* **14**, 477 (2004).

[255] B. Blau, D. Campi, B. Cure, R. Folch, A. Herve, I. L. Horvath, F. Kircher, R. Musenich, J. Neuenschwander, P. Riboni, B. Seeber, Sequeira Tavares, S. Sgobba, and R. P. Smith, *IEEE Trans. Appl. Supercond.* **12**, 345 (2002).

[256] F. Irie, K. Yamafuji, M. Takeo and F. Sumiyoshi, *IEEE Trans. Magn.* **19**, 672 (1983).

[257] P. Turowski, L. Z. Lin and E. Seibt, *IEEE Trans. Magn.* **17**, 2047 (1981).

[258] J. Neuenschwander, B. Blau, I. L. Horvath, Th. Luthi, and H. Marti, *IEEE Trans. Appl. Supercond.* **12**, 1199 (2002).

[259] T. Tonogi, G. Iwaki, S. Inaba, H. Hosono, A. Yamamoto, and A. Takahashi, *Hitachi Cable Review* **18**, 87 (1999).

[260] M. D. Sumption, M. Bhatia, X. Wu, M. Rindfleisch, M. Tomsic, and E. W. Collings, *Supercond. Sci. Technol.* **18**, 730 (2005).

[261] A. Serquis, Y. T. Zhu, E. J. Peterson, J. Y. Coulter, D. E. Peterson, and F. M. Mueller, *Appl. Phys. Lett.* **79**, 4399 (2001).

[262] S. X. Dou, S. Soltanian, Y. Zhao, E. Getin, Z. Chen, O. Shcherbakova, and J. Horvat, *Supercond. Sci. Technol.* **18**, 710 (2005).

[263] W. B. Sampson, M. Garber, and A. K. Ghosh, *IEEE Trans. Magn.* **25**, 2097 (1989).

[264] S. X. Dou, S. Soltanian, W. K. Yeoh, and Y. Zhang, *IEEE Trans. Appl. Supercond.* **15**, 3219 (2005).

[265] B. V. Reddy and S. C. Deevi, *Intermetallics* **8**, 1369 (2000).

[266] H. Suo, C. Beneduce, M. Dhalle, N. Musolino, J.-Y. Genoud, and R. Flukiger, *Appl. Phys. Lett.* **79**, 3116 (2001).

[267] S. Zhou, A. V. Pan, M. Ionescu, H. K. Liu and S. X. Dou, *Supercond. Sci. Technol.* **15**, 236 (2002).

[268] K. Tanaka, M. Okada, H. Kumakura, H. Kitaguchi, K. Togano, *Physica C* **382**, 203 (2002).

[269] S. X. Dou, J. Horvat, S. Soltanian, X. L. Wang, M. J. Qin, S. H. Zhou, H. K. Liu, and P. G. Munroe, *IEEE Trans. Appl. Supercond.* **13**, 3199 (2003).

[270] K. Tanaka, H. Kitaguchi, H. Kumakura, H. Yamada, M. Hirakawa and M. Okada, *Supercond. Sci. Technol.* **18**, 678 (2005).

[271] S. Soltanian, J. Horvat, X. L. Wang, M. Tomsic and S. X. Dou, *Supercond. Sci. Technol.* **16**, L4 (2003).

[272] Y. Takahashi, T. Ando, T. Hiyama, H. Tsuji, E. Tada, M. Nishi, K. Yoshida, K. Okuno, K. Koizumi, H. Nakajima, T. Kato, K. Kawano, M. Oshikiri, Y. Hattori, R. Takahahi, S. Kamiya, Y. Ohgane, and S. Shimamoto, *IEEE Trans. Magn.* **21**, 157 (1985).

[273] B. Lorenz, R. L. Meng, Y. Y. Xue, and C. W. Chu, *Phys. Rev. B* **64**, 052513 (2001).

[274] T. Nakane, H. Kitaguchi and H. Kumakura, *Supercond. Sci. Technol.* **19**, 528 (2006).

[275] G. A. Moller, US Patent no. 2315725 (1948).

[276] J. Horvat, S. Soltanian, X. L. Wang, and S. X. Dou, *IEEE Trans. Appl. Supercond.* **13**, 3324 (2003).

[277] J. H. Kim, personal communication.

[278] I. F. Lyuksyutova and V. L. Pokrovskya, *Adv. Phys.* **54**, 67-136 (2005).

[279] Yu. A. Genenko, A. Usoskin, and H. C. Freyhardt, *Phys. Rev. Lett.* **83**, 3045 (1999).

[280] C. Cheng and Y. Zhao, *Physica C* **463-465**, 220 (2007).

[281] B. Qu, X. D. Sun, J.-G. Li, Z. M. Xiu, S. H. Liu, and C. P. Xue, *Supercond. Sci. Technol.* **22**, 015027 (2009).

[282] V. P. S. Awana, M. Isobe, K. P. Singh, E. Takayama-Muromachi, and H. Kishan, *Supercond. Sci. Technol.* **19**, 551 (2006).

[283] T. Kuroda, T. Nakane, H. Uematsu, and K. Kumakura, *Supercond. Sci. Technol.* **19**, 1152 (2006).

[284] M. Mustapic, D. Pajic, N. Novosel, E. Babic, K. Zadro, J. Horvat, M. Cindric, Z. Skoko, A. Shcherbakov, and M. Bijelic, accepted for publication to Croatica Chemica Acta 2009

[285] D. Pajic, K. Zadro, R. E. Vanderberghe, and I. Nedkov, *J. Magn. Magn. Mater.* **281**, 353 (2004).

[286] A.T. Raghavender, D. Pajic, K. Zadro, T. Milekovic, P. Venkateshwar Rao, K. M. Jadhav, D. Ravinder, *J. Magn. Magn. Mater.* **316**, 1 (2007).

[287] E. Dorolti, P. Vlaic, E. Burzo, and C. Djega-Mariadassou, *AIP Conf. Proc.* **899**, 777 (2007).

[288] G. F. Korznikova, A. V. Korznikov, L. A. Syutina, and Kh. Ya. Mulyukov, *J. Magn. Magn. Mater.* **196-197**, 207 (1999).

[289] C. S. Lue, T. H. Su, B. X. Xie, S. K. Chen, J. L. MacManus-Driscoll, Y. K. Kuo, and H. D. Yang, *Phys. Rev. B* **73**, 214505 (2006).

[290] N. Novosel, D. Pajic, M. Mustapic, E. Babic, A. Shcherbakov, J. Horvat, Z. Skoko, and K. Zadro, *J. Phys.: Conf. Ser.* **234**, 022027 (2010).

[291] S. Xu, Y. Moritomo, K. Kato, and A. Nakimura, *J. Phys. Soc. Jpn.* **70**, 1889 (2001).

[292] P. P. Singh and P. Jili Thomas Joseph, *J. Phys.: Condens. Matter.* **14**, 12441 (2002).

[293] P. J. T. Joseph and P. P. Singh, *Solid State Commun.* **141**, 390 (2007).

[294] B. Gahtori, R. Lal, and S. K. Agarwal, Y. K. Kuo, K. M. Sivakumar, and J. K. Hsu, J. Y. Lin, Ashok Rao, S. K. Chen, and J. L. MacManus-Driscoll, *Phys. Rev. B* **75**, 184513 (2007).

[295] W. X. Li, R. Zeng, C. K. Poh, Y. Li, and S. X. Dou, *J. Phys.: Condens. Matter.* **22**, 135701 (2010).

[296] T. Maui, N. Suemitsu, Y. Mikasa, S. Lee, and S. Tajima, *J. Phys. Soc. Japan* **77**, 074720 (2008).

[297] A. A. Abrikosov and L. P. Gorkov, *Sov. Phys.- JETP* **12**, 1234 (1961).

[298] A. Yamamoto, J. I. Shimoyama, S. Ueda, Y. Katsura, S. Horii, and K. Kishio, *IEEE Trans. Appl. Supercond.* **15**, 3292 (2005).

[299] X. Xu, J. H. Kim, W. K. Yeoh, Y. Zhang, and S. X. Dou, *Supercond. Sci. Technol.* **19**, L47 (2006).

[300] M. S. A. Hossain, J. H. Kim, X. Xu, X. L. Wang, M. Rindfleisch, M. Tomic, M. D. Sumption, E. W. Collings, and S. X. Dou, *Supercond. Sci. Technol.* **20**, L51-L54 (2007).

[301] C. H. Jiang, S. X. Dou, Z. X. Cheng, and X. L. Wang, *Supercond. Sci. Technol.* **21**, 065017 (2008).

[302] O. V. Shcherbakova, A. V. Pan, E. Babic, and S. X. Dou, *J. Phys.* **234**, 012038 (2010).

[303] S. Lee, T. Masui, A. Yamamoto, H. Uchiyama, and S. Tajima, *Physica C* **412-414**, 31 (2004).

[304] O. Shcherbakova, S. X. Dou, S. Soltanian, D. Wexler, M. Bhatia, M. Sumption, and E. W. Collings, *J. Appl. Phys.* **99**, 08M510 (2006).

[305] O. V. Shcherbakova, A. V. Pan, J. L. Wang, A. V. Shcherbakov, S. X. Dou, and D. Wexler, *J. Phys.*: **97**, 012314 (2008).

[306] R. F. Klie, J. C. Idrobo, N. D. Browning, K. A. Regan, N. S. Rogado, and R. J. Cava, *Appl. Phys. Lett.* **79**, 1837 (2001).

[307] B. J. Senkowicz, A. Polyanskii, R. J. Mungall, Y. Zhu, J. E. Giencke, P. M. Voyles, C. B. Eom, E. E. Hellstrom and D. C. Larbalestier, *Supercond. Sci. Technol.* **20**, 650 (2007).

[308] A. Gurevich, *Phys. Rev. B* **67**, 184515 (2003).

[309] S. B. Samanta, H. Narayan, A. Gupta, A. V. Narlikar, T. Muranaka, and J. Akimitsu, *Phys. Rev. B* **65**, 092510 (2002).

[310] A. Yamamoto, J. Shimoyama, S. Ueda, Y. Katsura, I. Iwayama, S. Horii, and K. Kishio, *Physica C* **445**, 806 (2006).

[311] S. Keshavarzi, M. J. Qin, S. Soltanian, H. K. Liu, and S. X. Dou, *Physica C* **408-410**, 601 (2004).

[312] E. Martinez, P. Mikheenko, M. Martinez-Lopez, A. Millan, A. Bevan, and J. S. Abell, *Phys. Rev. B* **75**, 134515 (2007).

[313] A. V. Pan and S. X. Dou, *Phys. Rev. B* **73**, 052506 (2006).

Publications

1. S. X. Dou, E. W. Collings, O. Shcherbakova, and **A. Shcherbakov**, "Aluminium-stabilized magnesium diboride - a new light-weight superconductor", *Supercond. Sci. Technol.* **19**, 333 (2006).

2. S. X. Dou, E. W. Collings, O. Shcherbakova, **A. Shcherbakov**, M. Bhatia, M. Sumption and M. Tomsic, "Aluminum-Stabilized Magnesium Diboride Superconductors", *AIP Conf. Proc.* **824**, 639 (2006).

3. **A. Shcherbakov**, S. X. Dou, O. Shcherbakova and J. Horvat, "Development of MgB_2 wires with an aluminum as a stabilizer", published on the Australian Institute of Physics Website (http://www.aip.org.au/conferences.php) (2006).

4. **A. V. Shcherbakov**, A. V. Pan, and S. X. Dou, "Superconducting properties of Al-stabilized MgB_2 wires", *Physica C* **460** - **462**, 1420 (2007).

5. **A. V. Shcherbakov**, A. V. Pan, S. X. Dou, and E. W. Collings, "New Method for the Fabrication of Al-Stabilized Fe/MgB_2 Wires", *IEEE Trans. on Appl. Supercond.* **17**, 2806 (2007).

6. O. V. Shcherbakova, A. V. Pan, J. L. Wang, **A. V. Shcherbakov**, S. X. Dou, D. Wexler, E. Babić, M. Jerčinović, and O. Husnjak, "Sugar as an optimal carbon source for the enhanced performance of MgB_2 superconductor at high magnetic fields", *Supercond. Sci. Technol.* **21**, 015005 (2008).

7. O. V. Shcherbakova, A. V. Pan, J. L. Wang, **A. V. Shcherbakov**, S. X. Dou, and D. Wexler, "Identification of factors limiting the critical current density in $MgB_{2-x}C_x$ superconductors at low magnetic fields", *J. Phys.* **97**, 012314 (2008).

8. M. Mustapić, D. Pajić, N. Novosel, E. Babić, K. Zadro, J. Horvat, M. Cindrić, Z. Skoko, **A. Shcherbakov**, and M. Bijelić, "Synthesis, structural characterization and magnetic properties of iron boride nanoparticles with or without silicon dioxide coating", accepted for publication in *Croatica Chemica Acta* (2009).

9. N. Novosel, D. Pajić, M. Mustapić, E. Babić, **A. Shcherbakov**, J. Horvat, Z. Skoko, and K. Zadro, "Flux pinning and inhomogeneity in magnetic nanoparticle doped MgB_2/Fe wires", *J. Phys.* **234**, 022027 (2010).

10. **A. V. Shcherbakov**, J. Horvat, O. V. Shcherbakova, N. Novosel, E. Babić, and S. X. Dou, "Temperature effect on microstructure and electromagnetic performance of polycrystalline and sugar-doped MgB_2 wires", *J. Phys.* **234**, 022033 (2010).